UNIVERSIDADE FEDERAL DE MINAS GERAIS
Programa de Pós-Graduação em Engenharia Química

Tese de Doutorado

# "The Influence of Microstructure on the Hydrogen Embrittlement in Martensitic-Ferritic Stainless Steel"

Autor: Daniela Cristina de Sousa Garcia
Orientador: Vanessa de Freitas Cunha Lins
Co-Orientador: Dilson Silva dos Santos

Outubro 2015

UNIVERSIDADE FEDERAL DE MINAS GERAIS
Programa de Pós-Graduação em Engenharia Química

Daniela Cristina de Sousa Garcia

# THE INFLUENCE OF MICROSTRUCTURE ON THE HYDROGEN EMBRITTLEMENT IN MARTENSITIC-FERRITIC STAINLESS STEEL

Tese apresentada ao Programa de Pós-Graduação em Engenharia Química da Universidade Federal de Minas Gerais, como requisito parcial à obtenção do título de Doutor em Engenharia Química.

Área de Concentração: Corrosão
Orientador: Profª. Drª.Vanessa de Freitas Cunha Lins
Co-Orientador: Profº. Drº: Dilson Silva dos Santos

Belo Horizonte
Escola de Engenharia da UFMG
2015

Dedico esta tese à minha mãe querida, Irene de Sousa Garcia.

*“Não quero ter a terrível limitação de quem vive apenas do que é passível de fazer sentido. Eu não: quero uma verdade inventada, pois enquanto eu tiver perguntas e não houver resposta continuarei a escrever.”*

***Clarice Lispector***

# Acknowledgments

Gostaria de agradecer a Deus por ter me dado força, paciência, amparo e entusiasmo principalmente nesta reta final da realização deste trabalho.

Aos meus irmãos que sempre acreditaram em mim e confiaram que ia dar certo. Principalmente à Graziela que agora no final me deixou "quieta" para conseguir terminar de escrever.

A Vallourec Tubos do Brasil pelo incentivo e apoio financeiro para a realização desta pesquisa.

Ao Marcelo Ferreira da Vallourec Tubos do Brasil pela "compra da ideia" do trabalho, confiança, mesmo antes de eu ser funcionária da empresa e por todos os conselhos e ensinamentos.

Ao Ricardo Nolasco por ter me oferecido este projeto e por toda a paciência em sanar as minhas dúvidas.

Ao professor Dilson por toda a transferência de conhecimento no assunto, e pela visão crítica para a realização de um trabalho de qualidade e a professora Vanessa por todo seu apoio e confiança.

A Marília Lima por sua disponibilidade em sempre tirar minhas dúvidas em relação à metalurgia e também por sempre me ouvir nos momentos de angústias e inseguranças.

A Vania e Luciana R. por sempre me apoiarem e acreditarem na minha capacidade.

A Luciana Lima que mesmo de longe, sempre me ouviu e me apoiou quando necessário.

Aos meus queridos estagiários Hannah Lauar e Pedro Nogueira por serem em momentos diferentes meu braço direito na PD.

Aos meninos da PROPMEC Camila, Leandro, Gabriel e Monique por me ajudarem sempre que precisei na realização de ensaios e também nas dúvidas técnicas.

A Tatiane Santos por sempre me ajudar com os seus conhecimentos em metalurgia e ter me ajudado na definição das amostras com os resultados do seu trabalho de mestrado.

A todos os meus amigos que sempre me apoiaram e ficaram na torcida, em especial: Ana Paula, Raquel, Edisângela, Maraíza, Juliana Quintino, Renata, Kelly, Ívina, Sabrina, Marcela, Samuel e Mariana.

A Capes pelo apoio financeiro.

E a todos que direta ou indiretamente contribuíram para a realização deste trabalho tão sofrido, mas gratificante.

# Summary

# Abstract

This work investigates the interaction of hydrogen with the microstructure in the martensitic-ferritic stainless steel (MFSS). The samples were extracted from hot rolled seamless stainless steel tube after a solution treatment at 1000°C for 30 min and water quenched. In order to obtain retained austenite ($\gamma_{ret}$) the samples were heat treated (HT) at 600, 625, 675 and 675°C for 1h and water quenched, then the samples were heat treated at 625 and 675°C and were tempered at 600°C for 1h and water cooled. For the production of a chi sample ($\chi$-phase), the heat treatment was held at 670°C for 18h and water quenched. The samples were identified as follows: as-quenched (1000°C for 30min); Chi (HT at 670°C for 18h), LRA (low retained austenite heat treated at 600°C), RA (medium retained austenite heat treated at 625°C) and HRA (high retained austenite heat treated at 675°C). The microstructural characterization by scanning electron microscopy (SEM), X ray diffraction (XRD), Mossbauer and XRD Syncrothron showed 2, 7, 7 and 22% of $\gamma_{ret}$ in the samples LRA, RA, Chi and HRA, respectively. The amount of $\chi$-phase plus precipitates rich in Cr and Mo analyzed by image analyzer in the chi sample was 6%. The hydrogen permeation tests presented diffusivity for the as-quenched > Chi > LRA > RA > HRA and a solubility for the RA > Chi > HRA > as-quenched > LRA. All the samples presented the diffusible hydrogen and reveal the irreversible characteristics of retained austenite to trap hydrogen, and feature of $\chi$-phase to absorb hydrogen. Tensile tests in the cathodically hydrogen charged samples showed a high loss ductility when compared with samples tested without hydrogen charge. The results performed at 0.01mm/s rate, showed higher loss ductility for Chi, LRA and RA samples than the same samples tested at 1.0mm/s rate. It was possible to observe a trend to increase the hydrogen embrittlement with the increase in the amount of retained austenite. The **retained austenite** in the samples chi, LRA and HRA showed a trend of **transformation-induced plasticity (TRIP) effect**, with a reduction in the levels of austenite and a increase in the quantities of martensite in the area close to the **necking** after the tensile tests performed in the cathodically charged samples. The retained austenite showed a deleterious effect in this material, promoting a high hydrogen embrittlement.

# Resumo

Neste trabalho foi investigada a interação do hidrogênio com a microestrutura do aço inoxidável martensítico-ferrítico. O estudo foi realizado em tubo de aço sem costura que foi laminado a quente, austenitizado a 1000°C por 30 min e temperado em água. Para a obtenção de austenita retida, este material foi revenido nas temperaturas de 600, 625, e 675°C por 1h e resfriados em água. As amostras tratadas termicamente a 625 e 675°C passaram por um segundo revenimento à temperatura de 600°C por 1h e foram resfriadas em água. Já para a obtenção de fase chi as amostras foram tratadas termicamente à temperatura de 600°C por 18h. Para falicitar a compreensão, as amostras foram chamadas de as-quenched (austenitizada a 1000°C e temperada em água), Chi (TT a 670°C por 18h) AB (austenita retida baixa TT a 600°C), AM (austenita retida média TT a 625°C) e AA (austenita retida alta TT a 675°C). A caracterização da microestrutura após os tratamentos térmicos foi realizada por microscopia eletrônica de Varredura (MEV), difração de raios X (DRX), Mossbauer e DRX Syncronthron mostrou um teor de 2, 7, 7 e 22% de $\gamma_{ret}$ para as amostras tratadas AB, AM, Chi e AA, respectivamente, e a amostra chi analisada também por um analisador de imagens apresentou um teor de 6% de fase $\chi$ e/ou precipitados ricos em Cr e Mo. Os ensaios de permeação de hidrogênio mostraram valores de difusividade para as amostras na seguinte ordem : as-quenched > Chi > AB > RA > AA e a seguinte ordem de solubilidade : amostra RA > Chi > AA > as-quenched > AB. Todas as microestruturas estudadas apresentaram a presença de hidrogênio difusível e revelaram o caráter irreversível do aprisionamento do hidrogênio pela austenita retida e a característica de alta absorção de hidrogênio da fase chi. Os resultados de tração com as amostras hidrogenadas apresentaram uma alta perda de ductilidade quando comparados com as amostras testadas sem hidrogenação. O ensaio de tração realizado à taxa de 0.01mm/s apresentou uma maior perda de ductilidade para as amostras Chi, AB e AM quando comparados com os ensaios realizados à taxa de 1.0mm/s. A austenita retida nas amostras chi, AB e AA mostraram uma tendência de transformação induzida por deformação plástica, apresentando uma redução na quantidade de austenita retida e um aumento na quantidade de martensita na região próxima à estricção após o ensaio de tração realizado com as amostras hidrogenadas. A austenita retida e a fase chi

apresentaram um efeito deletério neste aço, promovendo uma alta fragilização pelo hidrogênio.

# Organization of the work

*This document is organized in:*

**Resumo Expandido;**

**Chapter 1 - Introduction;**

**Chapter 2 - Objectives;**

**Chapter 3 – Heat treatment in the martensitic-ferritic stainless steel (MFSS) to obtain chi-phase and different amount of retained austenite: Preliminaries Results.** This chapter presents the main characteristics of the phase transformation with the preliminary analysis to obtain the samples studied in this study. The chapter is divided in *Introduction, Experimental Details, Preliminaries Results and Discussion, Conclusions and References.* The goal of this chapter is to give an overview of the phase transformation of reversed/retained austenite and chi-phase, and shows the preliminary results of the heat treatment performed on the samples.

**Chapter 4 - Materials and Methods, Results and Discussion.** This chapter presents the methodology and results in the scientific paper format. This study produced 4 papers and they will be presented in this chapter.

**Chapter 6 – Conclusions and next steps**

## Resumo Expandido

Problemas comuns na indústria do petróleo são trocas de materiais que atuam neste segmento devido a danos sofridos pelo processo corrosivo. Além da preocupação ambiental, prejuízos econômicos é sempre um fator a ser considerado na escolha do material a ser utilizado neste segmento. Materiais metálicos que operam em meio de petróleo devem ser inspecionados e monitorados de modo a evitar ou minimizar problemas causados pela corrosão. A presença de $H_2S$ que é um contaminante do petróleo e também proteções catódicas que são realizadas neste ambiente pode causar um fenômeno conhecido como Fragilização pelo Hidrogênio (HE), no qual o hidrogênio gerado pode ser absorvido pelo material, penetrar na estrutura metálica e provocar fraturas frágeis em materiais que são por essência dúctil.

No contexto atual deste segmento, os aços inoxidáveis supermartensíticos e inoxidáveis duplex seriam uma boa opção para serem utilizados neste ambiente, pois além de apresentarem propriedades mecânicas satisfatórias, possuem maior resistência à corrosão do que os aços carbonos de alta liga. Devido às novas descobertas de ambientes cada vez mais severos, i.e. baixo pH, alta concentração de cloretos e $H_2S$, estas opções de materiais não são satisfatórias o suficiente. Por um lado, os aços duplex possuem maior resistência à corrosão, mas com um custo elevado. Por outro lado, os SMSS apresentam menor custo, mas limitada resistência à corrosão.

Com o objetivo de oferecer ao mercado uma opção com maior custo/benefício, os aços inoxidáveis martensíticos-ferríticos estão sendo desenvolvidos com uma maior resistência à corrosão do que os supermartensíticos e menor custo do que os duplex. Como se trata de um material totalmente novo é importante antes de oferecê-lo ao mercado, avaliar problemas relacionados à corrosão e consequentemente à fragilização pelo hidrogênio. Desta forma, neste trabalho buscou-se estudar a susceptibilidade à HE neste novo material. Neste trabalho, foi realizado um estudo da interação do hidrogênio com a microestrutura do material, assim como a influência deste elemento nas propriedades mecânicas do material. O aço estudado foi um aço inoxidável martensítico-ferrítico com 14% de Cr, alto teor de Ni e Mo, que está sendo desenvolvido para resistir a ambiente com altas concentrações de hidrogênio e pH’s ácidos.

O objetivo do trabalho foi avaliar a interação do H com a microestrutura do aço inoxidável martensítico-ferrítico (AIMF) com diferentes tratamentos térmicos e o efeito deste elemento na propriedade mecânica deste material. Para isso, teve-se como objetivos específicos:

- Realização de tratamentos térmicos específicos para obtenção de fase-chi e diferentes quantidades de austenita revertida retida;
- Caracterização da microestrutura por meio de análise de Mossbauer, MEV e DRX;
- Determinação da difusividade e solubilidade do hidrogênio nestas diferentes microestruturas;
- Avaliação da susceptibilidade à fragilização pelo hidrogênio por meio de ensaios de tração em diferentes taxas de deformação em amostras previamente carregadas catodicamente com hidrogênio e em amostras não carregadas.

Para a obtenção das diferentes quantidades de austenita revertida retida e fase-chi as amostras somente temperadas foram tratadas termicamente de acordo com o esquema da figura 1. Para a amostra chi o tratamento térmico escolhido para seguir adiante com os ensaios com hidrogênio foi o de 670°C por 18h, devido a maior quantidade desta fase identificada pelo analisador de imagens e também pela técnica de Mossbauer (~ 6%). Já para a amostra com austenita revertida retida os tratamentos térmicos foram realizados para obtenção de baixa (~ 3%), média (~7%) e alta (~22%) quantidade de austenita retida, conforme descrito na figura e todas as amostras foram testadas com hidrogênio. Além das amostras com fase-chi e austenita revertida retida, uma amostra temperada também foi escolhida para se ter como referência.

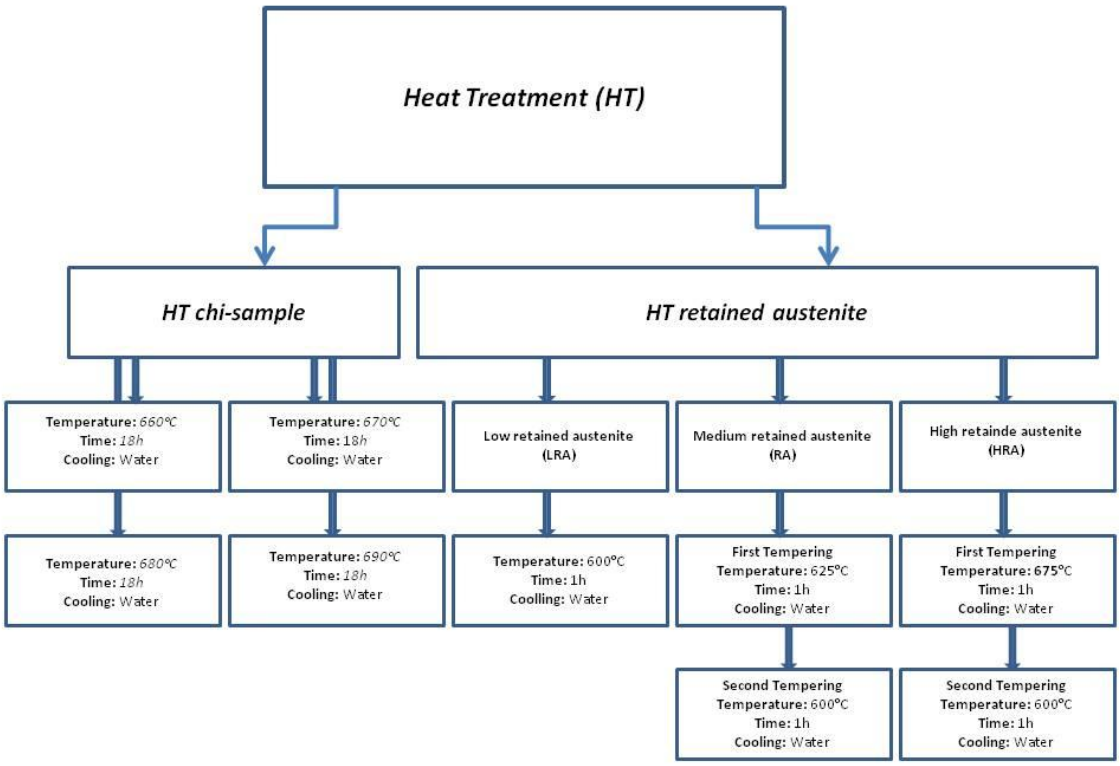


As amostras após tratamento térmico, foram submetidas a ensaios de permeação eletroquímica de hidrogênio pela técnica desenvolvida por Devanthan-Starchusck, no qual a morfologia da austenita revertida retida mostrou uma influência na permeação do hidrogênio, sendo o menor coeficiente de difusão obtido para a amostra com maior quantidade de austenita revertida retida (22%) e a maior solubilidade para a amostra com média quantidade desta fase (7%).

A fragiliação pelo hidrogênio foi investigada nestas amostras por ensaio de tração nas amostras carregadas catodicamente com hidrogênio e comparadas com o resultado da amostra sem o carregamento com hidrogênio. As amostras carregadas catodicamente com H mostraram em sua maioria fratura frágil com pouca redução de area e baixo alongamento. As amostras com alta quantidade de austenita revertida retida mostraram uma maior fragilização pelo hidrogênio, que as amostras com menor quantidade desta fase, o que demonstra esta fase exercer uma influência no aumento da FH neste material estudado. Este efeito deletério desta fase, parece estar relacionado com o efeito de transformação induzido por deformação, no qual a austenite revertida retida devido à deformação sofrida pelo hidrogênio pode se ter transformado em maternsita, aumentando assim a susceptiblidade à FH. A amostra com fase-chi mostrou uma alta

FH com uma perda de ductilidade de 80% , mostrando também o efeito deletério desta fase neste tipo de aço.

Para finalizar foi realizado os ensaios de dessorção à temperatura programada (TPD) em que as amostras foram ensaiadas em 3 diferentes taxas de aquecimento (6, 9 e 12°C.min$^{-1}$). A amostra com maior quantidade de austenite revertida retida (22%) apresentou a maior energia de ativação para o primeiro pico, comprovando assim o efeito irreversível do aprisionamento do hidrogênio nesta fase.

Com os resultados obtidos, foi possível concluir que a morfologia da austenita revertida retida desempenha um papel importante na difusão e solubilidade do hidrogênio, no qual a amostra com 22% desta fase que apresentou a austenita em forma de placas apresentou o menor coeficiente de difusão enquanto que a amostra com esta fase na forma de agulhas apresentou a maior solubilidade de hidrogênio. Foi possível observar também que houve uma significante redução de ductilidade do material na presença de hidrogênio, tanto para as amostras com austenita revertida retida, quanto para a amostra com fase-chi. E por fim, todas as amostras apresentaram a presença de hidrogênio difusível e também a presença de aprisionadores irreversíveis com a dessorção de hidrogênio em temperaturas mais elevadas.

# *CHAPTER 1 - Introduction*

## Introduction

The replacement of materials in the oil and gas industry due to damage promoted by corrosive process is a common problem faced by companies operating in this segment. In addition to environmental concerns, economic loss is always a factor to be considered in the choice of the material to be used. Metallic materials that operate in transport and oil rigging should be monitored in order to minimize the problems caused by corrosion. The $H_2S$ that is a contaminant of the oil and the cathodic protection used in the subsea applications could promote a phenomenon called hydrogen embrittlement (HE), in which hydrogen can be absorbed and penetrate in the metallic structure and promote brittle failures in ductile materials.

In the actual context of this segment, the supermartensitic stainless steel (SMSS) and duplex stainless steel (DSS) is a good option to be used, because besides having satisfactory mechanical properties they also have a higher corrosion resistance than high alloy carbon steels. Due the new discoveries of sour service environment, i.e.: low pH, high $H_2S$ and chloride concentrations, these options (DSS and SMSS) are not sufficient enough. In one hand, the DSS has a high corrosion resistance, but also showed high costs. On the other hand, the SMSS has low costs, but a limited corrosion resistance.

In order to produce an alternative material with lower costs than DSS, and a higher corrosion resistance than SMSS, the martensitic-ferritic stainless steel (MFSS) is under development.

Since this is a completely new material, it is important to evaluate the corrosion resistance and, hence, the HE before making the material available. This research aims to study the interaction of hydrogen with the microstructure of the material and the impact of this element in the material's mechanical properties. The chosen steel to be studied is a MFSS with 14Cr-5Ni-3Mo-5wt%.

# *CHAPTER 2 - Objectives*

## Objectives

This study aimed at evaluating the interaction of hydrogen on the microstructure in the martensitic-ferritic stainless steel (MFSS) with different heat treatments and the effect of this element in the mechanical properties of this material.

Specific objectives:

- Heat treat the samples in order to obtain chi-phase and different amounts of retained austenite;
- Characterize these microstructures;
- Determine the diffusivity and solubility of hydrogen in different samples;
- Characterize the nature of existing hydrogen traps;
- Evaluate the hydrogen embrittlement susceptibility in the microstructure, performing tensile tests in different strain rates in samples uncharged and cathodically charged with hydrogen.

# *CHAPTER 3 - Preliminaries results:*

***Heat treatment in martensitic-ferritic stainless steel to transform different amounts of retained austenite and chi-phase***

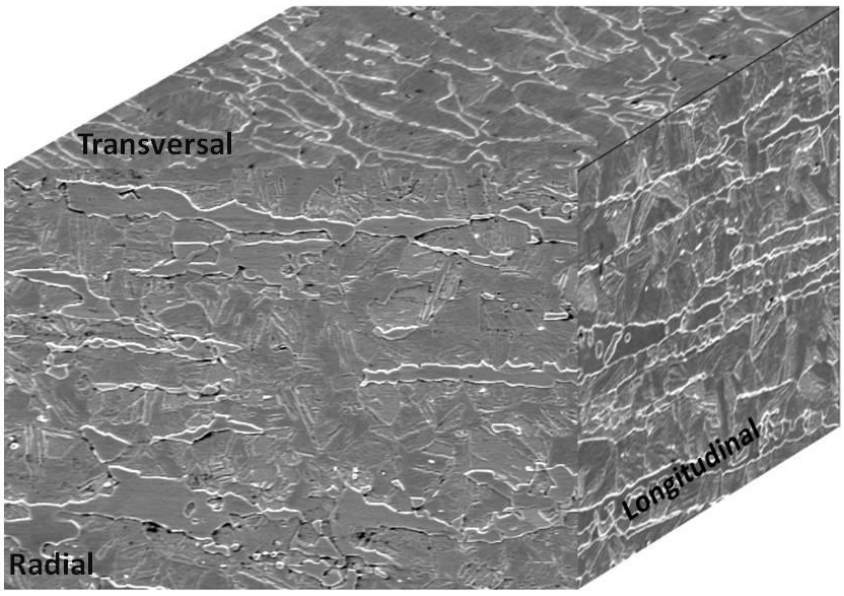

## Abstract

In order to obtain different amounts of retained austenite and chi-phase in martensitic-ferritic stainless steel, different timings and tempering temperatures were used. Different amounts of the reversed austenite were obtained by controlling the tempered temperature. High amounts of reversed and retained austenite were obtained in a sample heat treated at 675°C for 1h. The high amount of chi-phase precipitated was obtained in a sample heat treated at 670°C for 18h. The cooling at sub-zero temperature to destabilize retained austenite was not enough to transform this phase. The samples chosen to be tested in hydrogen condition in the following chapters were as-quenched, Chi, LRA, RA and HRA.


## Introduction

The stainless steel is a class of steel that presents in the chemical composition Cr above 11 wt%, good toughness, a high corrosion resistance and good weldability. On one hand, the improvement on the corrosion resistance is conferred because of the high amount of Cr, and also for Mo and Ni content. On the other hand, good toughness is attributed due the presence of retained austenite on the microstructure. Martensitic-ferritic stainless steel (MFSS) is a new class of steel that is being developed in order to substitute the traditional super martensitic stainless steel in the sour environment, i.e. a medium of high chloride concentration, high $H_2S$ content and a low pH. This kind of material contains mainly 14%Cr-5%Ni-3%Mo and depending on the heat treatment conditions, the final microstructure can present different amounts of retained austenite and chi-phase. It is known that $\chi$-phase promote a deleterious effect in the material, e.g. decrease toughness, and depending on the amount of retained austenite in the microstructure this phase can provide the improvement or the depletion in the steel. Due this, the study of the austenite reversion and chi-phase transformation is necessary.

***Reversed and retained austenite***

In general, the thermal cycle is projected to have an austenitization above 900°C and quenching in a temperature slightly above of $Ac_{1,}$ hence, even small amounts of austenite can be reversed and consequently retained in the microstructure.

The martensitic-ferritic stainless steel studied in this work was produced with a balance of alloy elements generating a microstructure with martensite (~78%) plus ferrite (~22%) at room temperature. The amount of Cr, Mo, Ni and C is ~14 , ~3, ~5 and ~0.01 wt. % respectively, and these elements have a major influence in stabilization of ferrite and prior austenite at room temperature.

The ternary diagram Fe-Cr-C in figure 1a shows the combination of Cr content versus temperature for an alloy with 0.01C wt% [1]. It is possible to observe that between the austenitic field and fully ferritic region, there is a specific range of Cr (12-14%) that corresponds to the ferrite derived from solidification and martensite formed from the rapid cooling of austenite. On one hand, the role of Mo is stabilizing the ferrite, as showing in the figure 1b, i.e. the addition of this element decreases the austenitic region and is necessary to add gammagenic element to maintain the fully martensitic region after cooling. On the other hand, Ni is an austenite stabilizer and the addition of this element is necessary to control the formation of martensite and retained austenite (figure 1c) [1].

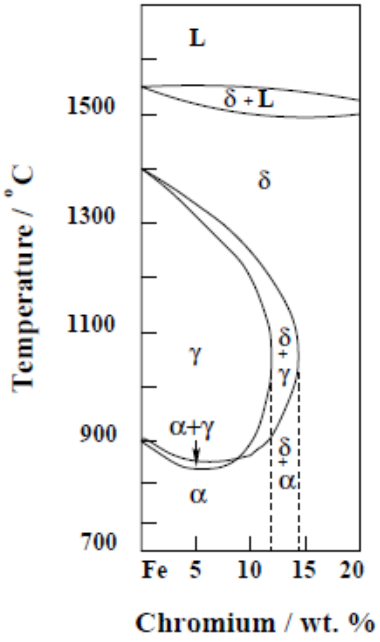


**(a)**

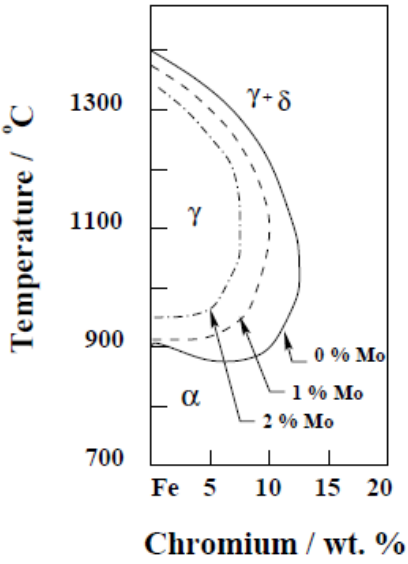


**(b)**

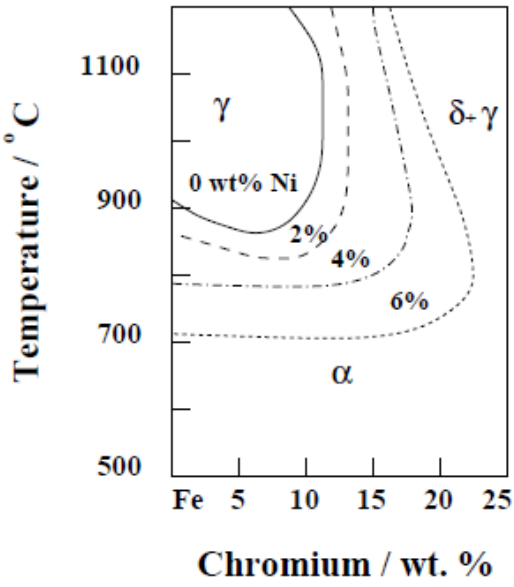


**(c)**

**Figura 1: a)** Ternary diagram Fe-Cr-C; **b)** Effect of molybdenum on the austenite phase stability field in the Fe-Cr phase diagram; **c)** Influence of nickel on the range of the austenite phase field in the Fe-Cr system. Adapted from Carrouge 2002 [1].

The amount of Ni determining the stability of the austenite, so that retained austenite remain in the microstructure due to lower the final temperature of the martensite transformation (Mf) below room temperature.

Thus, in this kind of material the relation between $Cr_{eq}$ and $Ni_{eq}$ control the formation of martensite and retained austenite. The volume fraction of retained austenite is a combination between thermodynamic and kinetic parameter. The amount of gammagenic elements in the matrix, temperature and time are key parameters to remain austenite retained at room temperature.

Zou et. al. [2] studied the influence of tempering processes in supermartensitic stainless steel (MFSS) performing a heating treatment of the material from 520 to 720°C for 3h and cooling in air. It can be observed in the figure 2 adapted from these authors that as the tempering temperature increase from 520 to 600°C the amount of retained austenite increase, achieving the maximum content at 600°C. Above 600°C, the amount of this phase decrease considerable and achieve almost the same quantity of retained austenite in the sample tempered at 520°C. This fact is attributed to the content of reversed austenite and its stability during the tempering process. It is known that the increase in the tempering temperature increase the amount of reversed austenite. Thus, at low temperature the reversed austenite nucleation starts at preferential locals with a high Ni concentration giving rise to an austenite rich in solute and with a low $M_s$ temperature, hence promoting high stability of this phase at room temperature. At high temperature, the nucleation of this phase does not occur necessarily in these locals of high Ni concentration, promoting an austenite less stable that transform to tempered martensite after cooling [3]. Song [4] studied the influence on tempering temperature in martensitic stainless steel and also found the same trend of Zou et al. [2], and attributed this fact for the local concentration of Ni, that decrease with the increase in temperature.

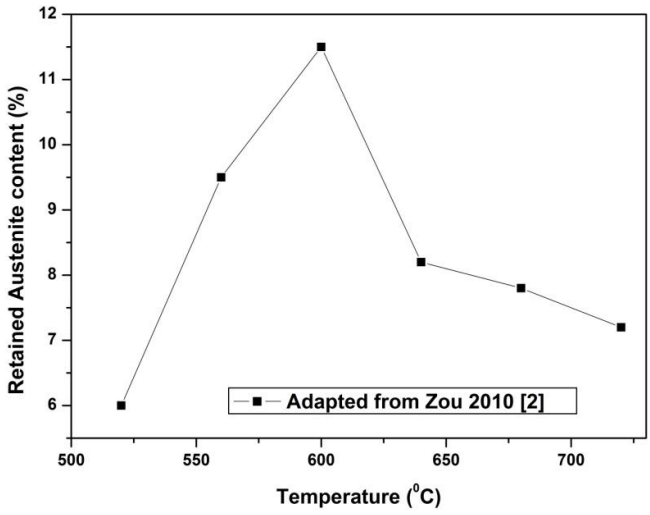


**Figura 2:** Tempering at different temperatures for 3 h; Adapted from Zou 2010 [2].

***χ-phase transformation***

The parameters chosen to transform χ-phase in the MFSS in this work were based on thermocalc of this alloy and in the available literature of DSS.

In general, the χ-phase in DSS coexists with σ-phase, and depending on the combination of time and temperature the first one can be replaced by the second one [5].

Escriba et. al. [5] studied χ-phase transformation in a duplex stainless steel with different tempering temperature and soaking time. They have found that as higher the temperature and holding time, as higher the tendency of chi-phase to be replaced by sigma-phase. They concluded that χ-phase precipitates preferentially at ferrite/ferrite grain boundaries prior to the σ-phase precipitation. In figure 3, the SEM observations of these authors exhibiting χ-phase and σ-phase precipitated at grain boundaries are shown. Michalska and Sozánska [6] and Yang et. al. [7] also showed the coexistence of chi and sigma phases in DSS in different tempering temperature and soaking time.

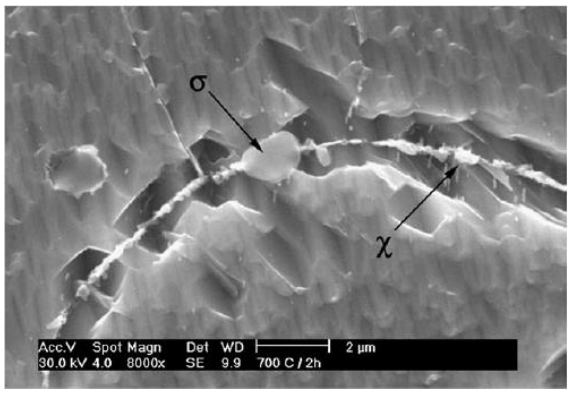


**Figura 3:** Scanning electron microscopy micrographs of chi and sigma phases in the DSS in the aged condition: 700°C for 2h followed by quenching water. Adapted from Escriba et. al. 2009 [6].

## Experimental Details

The reference sample (as-quenched) was a pipe rolled and quenched at 1000°C for 30 min and water quenched. The microstructure of this sample in the transversal, radial and longitudinal directions is shown in Figure 4. For this sample, the configuration of heat treatment to obtain the retained austenite and chi-phase are summarized in the figure 5. The conditions of the heat treatment to obtain retained austenite were based on the

results from the study of Santos et. al. [8]. In their work, the authors evaluated the austenite reversion and found that at 675°C there is a high amount of reversed and retained austenite (figure 6).

The chosen temperature in the present work was performed in order to obtain low, medium and high amounts of retained austenite (~3; ~10 and ~23% respectively). In the retained austenite (RA) and in the high retained austenite HRA samples, the second tempering was chosen to temper the untransformed martensite.

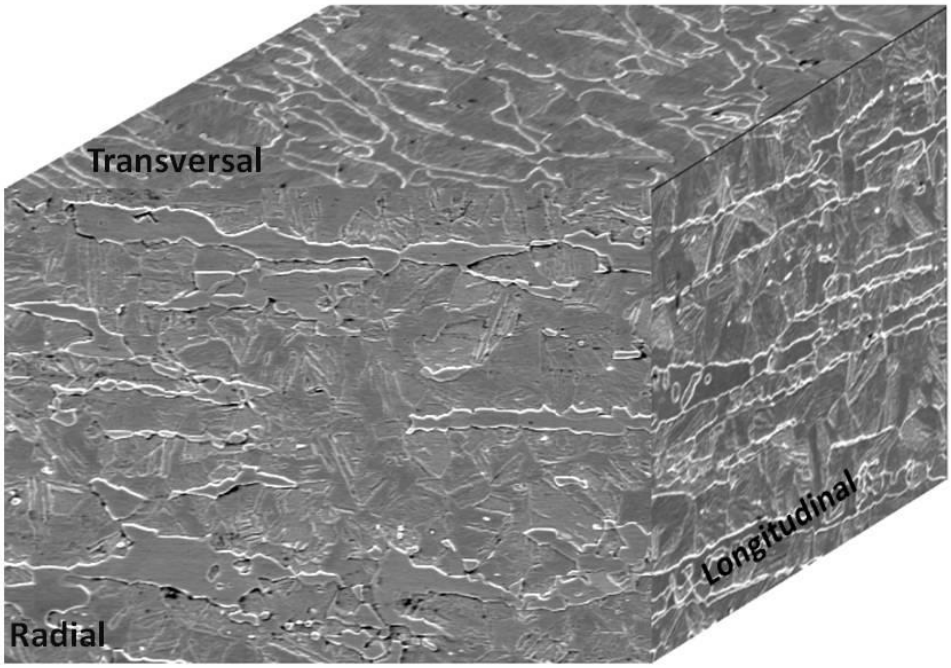


**Figura 4:** as-quenched sample in three directions.

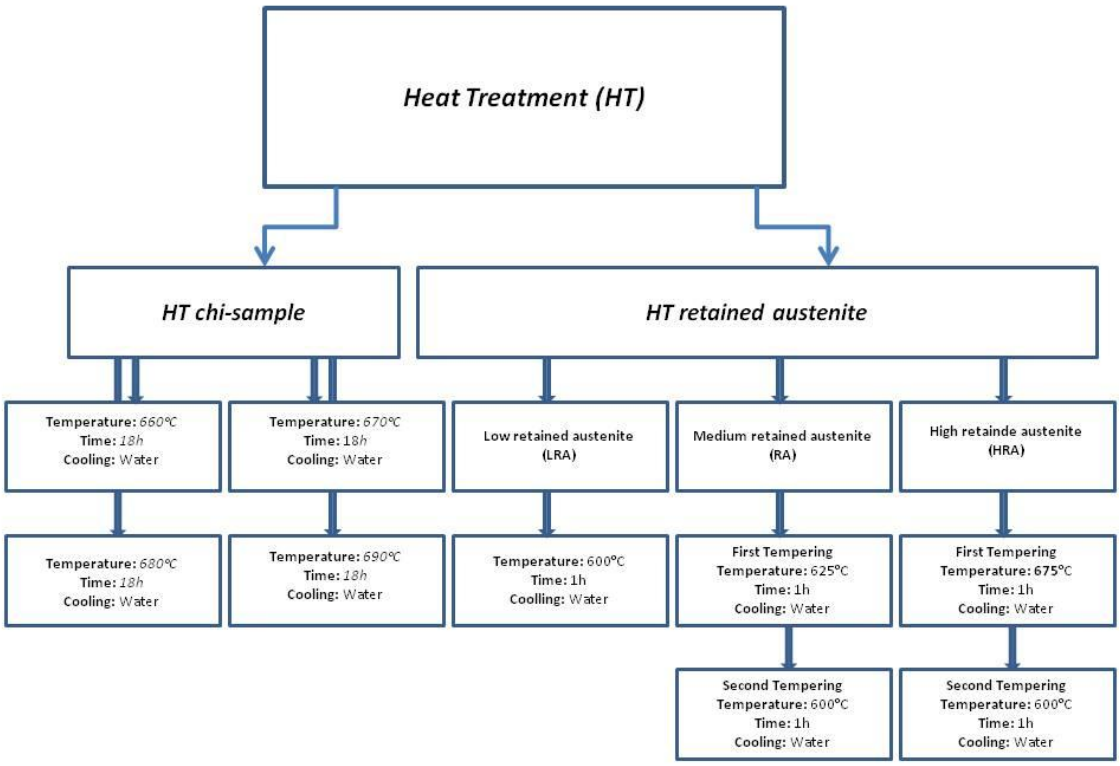


**Figura 5:** Heat treatment of samples.

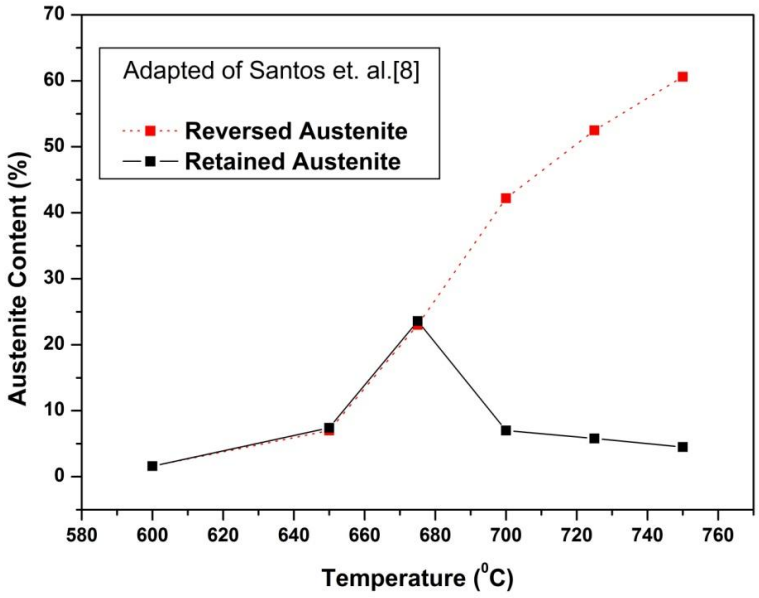


**Figura 6:** Austenite transformation. Adapted of Santos et. al. [8].

To obtain chi sample, the temperature of the heating treatment was based on the thermocalc of this alloy (figure 7). In the temperature below 950°C, the phase transformation initiates, and in the range below from 700 to 550°C, the maximum volume of fraction transformation is obtained. In the range temperature showed by thermocalc was not possible to observe the sigma-phase transformation, and it was believed that these phases do not coexist in these temperatures. The heat treatment of this sample was carried out in the range of 660 to 690°C, as described in the figure 5. In order to favor the precipitation kinetics, the soaking time was of 18h followed by water quenching for each sample.

Since the temperature for the formation of χ-phase is very close to the maximum content of retained austenite, i.e. 670 versus 675°C, 1 sample was heat treated at 675°C and then cooled at sub-zero temperatures with nitrogen for 1h, and then quenched in 600°C for 1h. This procedure was adopted in order to disestablish and transform austenite into martensite, and obtain just chi-phase in the sample. The heat treatment for this sample was the same used in the HRA HT, with cooling in nitrogen before the second tempering. The sample with nitrogen cooling was called $HRA_1$. The volume fraction of the retained austenite was determined by X-Ray-diffraction (XRD) pattern recorded using a D8 ADVANCE X-ray machine (Cu Ka radiation with 1% 1.5406Å) and scanning electron microscope (SEM), JEOL JSM 6460. Chi-phase was estimated by SEM and the quantification was made using image analysis and optical microscopy after polishing.

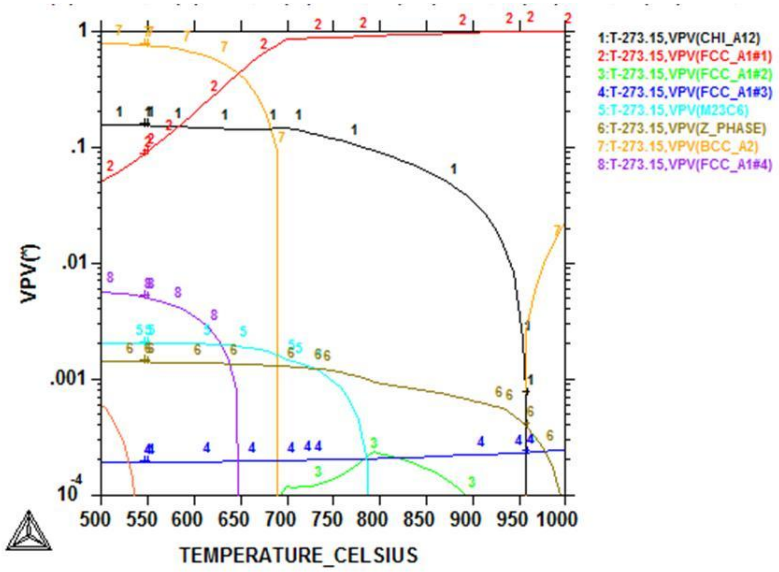


**Figura 7:** Thermocalc of Martensitic-Ferritic Stainless Steel.

## Results and Discussion

### *Retained austenite content*

The XRD results are shown in the figure 8. It can be observed that as higher the temperature as higher the amount of retained austenite. The quantification of this phase was made by using Rietveld method using TOPAS software of Bruker and the results are summarized in table 1. The amount of retained austenite in the $HRA_1$ was very close to HRA, the austenite in this material is stable enough to transform to martensite. Song et. al. [9] studied a martensitic stainless steel with different tempering temperatures and also cooled the material after heat treatment in sub-zero temperature, and instead destabilize this phase, they found a higher amount of retained austenite than before cooling. The reason of this is not establish yet, in fact, there are many hypotheses concerning the thermal stability of the reversed austenite, and this phenomenon is not yet well understood, and more studied on it need to be performed.

Due to the low transformation of austenite to martensite, this sample was discarded and the research was done in as-quenched, Chi, LRA, RA and HRA samples.

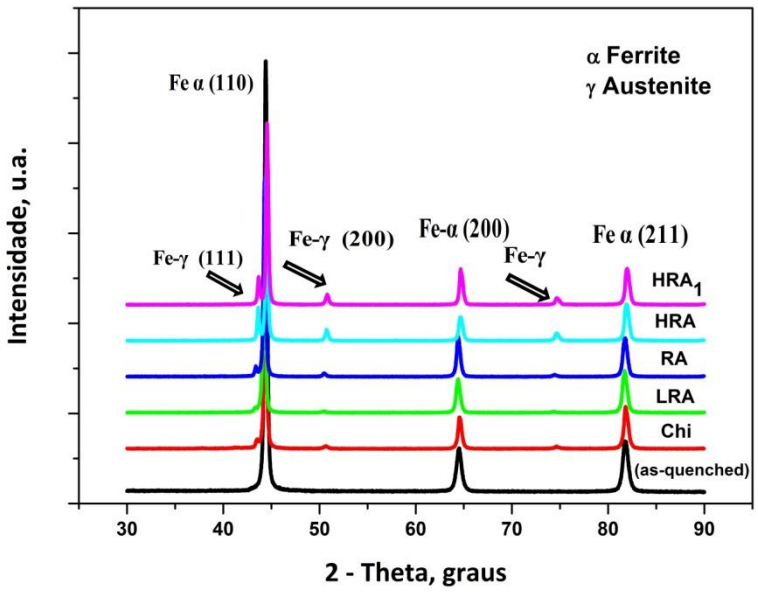


**Figura 8:** XRD results of all heat treated samples.

**Table 1:** Amount of austenite and ferrite in the samples.

| Sample Identification | Austenite (%) | Ferrite (%) |
|---|---|---|
| **As-quenched** | 0 | 100 |
| **Chi** | 7.0 | 97.0 |
| **LRA** | 2.7 | 97.3 |
| **RA** | 7.1 | 92.9 |
| **HRA** | 22.2 | 77.8 |
| **$HRA_1$** | 20.0 | 80.0 |

***χ-phase identification and quantification***

The SEM results of identification of χ-phase are shown in figure 9. A thin phase is observed in the grain boundaries and precipitates inside the ferrite, identified using EDX analysis and showed a high amount of Cr and Mo. This phase can be the χ-phase.

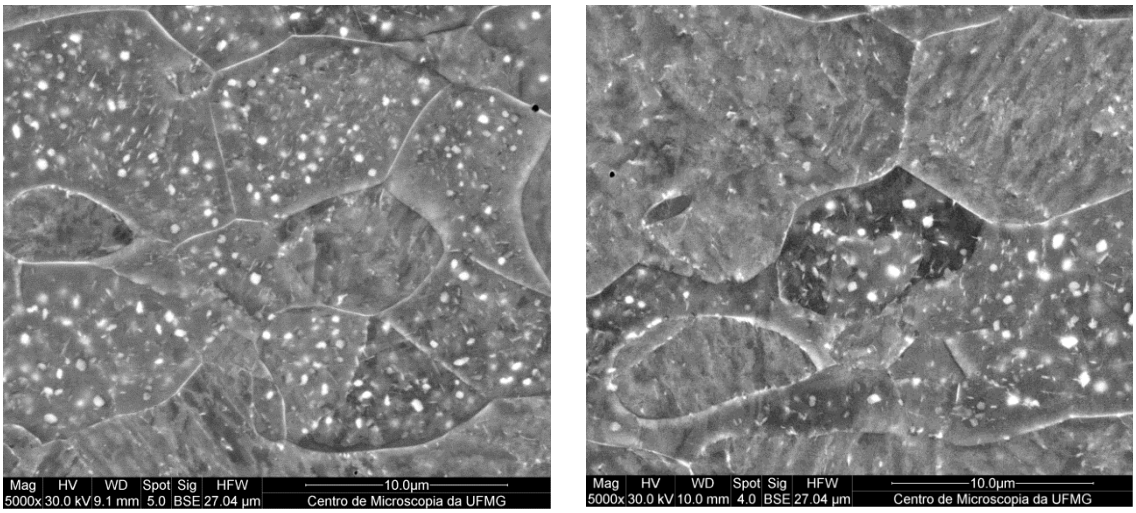


**(a)** **(b)**

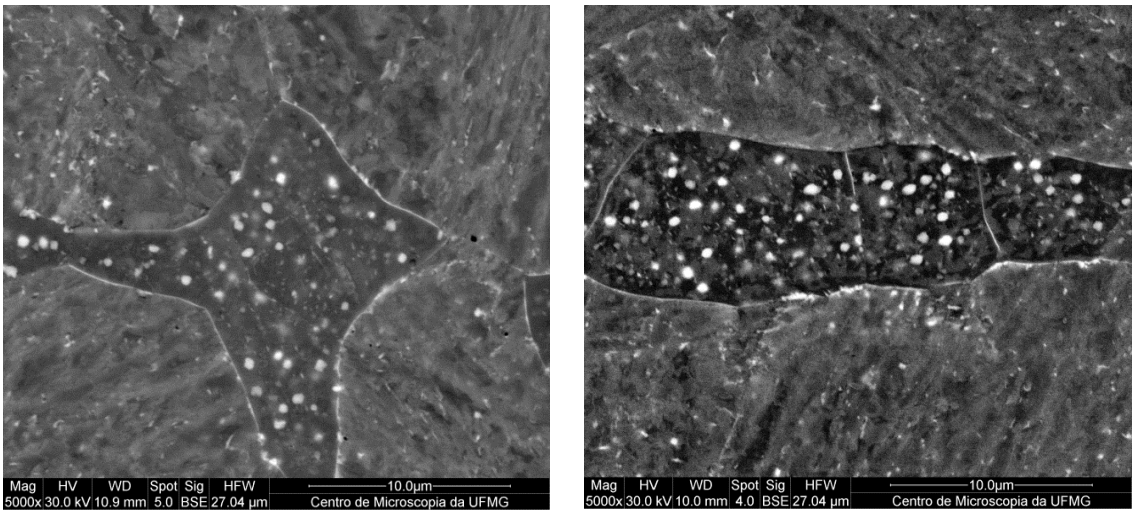


**(c)** (d)

**Figura 9:** SEM observation in sample heat treated for 18h to obtain χ-phase. **a)** sample heat treated at 660°C; **b)** sample heat treated at 670°C; **c)** sample heat treated at 680°C; **d)** sample heat treated at 690°C.

In order to quantify the χ-phase, the SEM images of heat treated samples at 660 and 670°C were analyzed taking into account different shades of gray and the results are shown in figure 10. The results are the average of 5 different regions of the samples and two magnifications (2000x and 5000x). The chi-phase was considered as being the blue points (figure 10b and 10d). These samples were selected since the SEM showed visually high amount of this phase in these two temperatures.

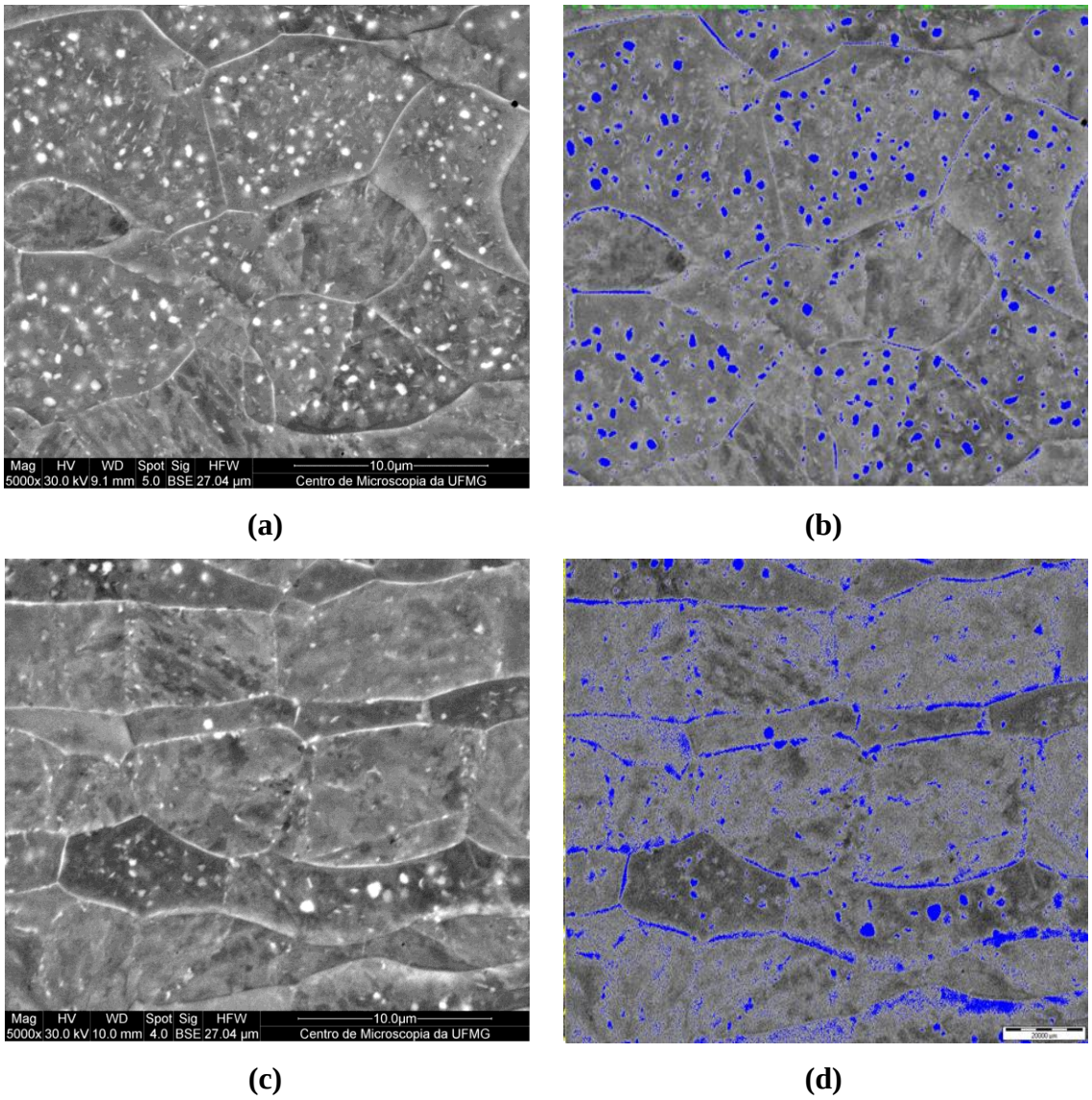


**Figura 10:** Sample heat treated for 18h. **a)** SEM observations of chi-sample heat treated at 660°C for 18h**, b)** Image analyzer of image a; **c)** SEM observations of chi-sample heat treated at 670°C for 18h; **d)** Image analyzer of image c.

The quantification of this phase is presented in table 2. The heat treated sample at 670°C presented a higher amount of this phase, and it was chosen to be tested under hydrogen conditions in the following chapters.

**Table 2:** χ-phase quantification.

| Heat Treatment | X-phase (%) |
|---|---|
| **660°C** | **4.7** |
| **670°C** | **6.0** |

In order to characteze the χ-phase, an EDS map of elements on the sample surface was obtained and the results are shown in figure 11. The Cr and Mo showed a high concentration on the ferrite phase, which was already expected as these elements are alphagenic and promote the formation of the bcc phase. However, the Ni content is higher in the martensitic phase; furthermore, this element is gammagenic and favor the austenite formation.

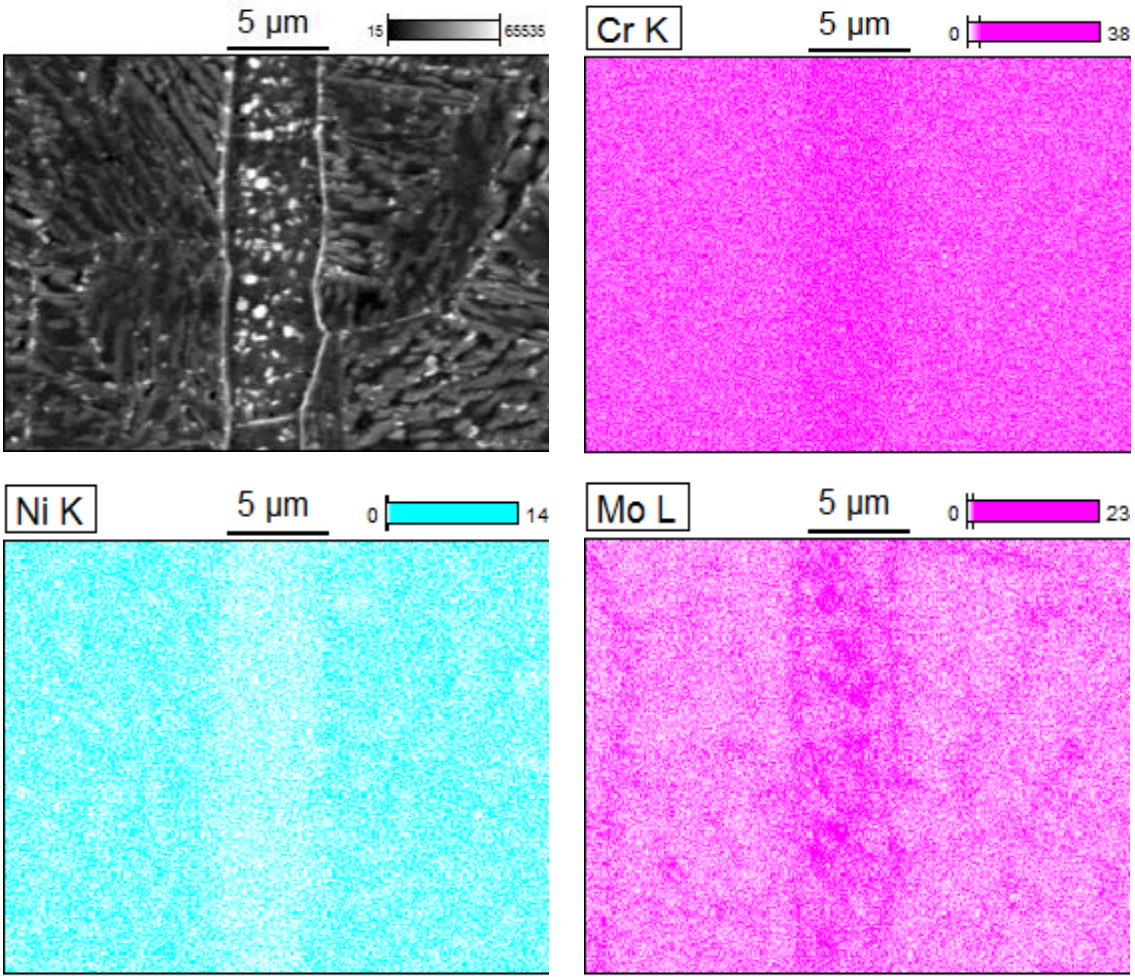


**Figura 11:** Structure mapping by SEM.

The EDS linescan was performed to identify the concentration of the Cr and Mo along the area that was considered to have a higher amount of χ-phase, i.e. grain boundary and ferrite (figure 12). It is possible to observe a high amount of Mo in the precipitate inside the ferrite and in the grain boundary. The chi-phase is considered as a phase with α-Mn-type with lattice parameter of 8.895Å and was indexed by Kasper [10] on the basis of a bcc cell. Kasper et al. [10] discussed the ordering of the atoms in the unit cell, and concluded that this phase can be a combination of Fe-Cr-Mo with geometrical

arrangements of neighbors and occurs around Mo, but different proportions of Cr with other elements can occur. Further discussions on the identification and quantification of this χ-phase in the chi-sample will be done in the chapter 4, paper 1 and 2.

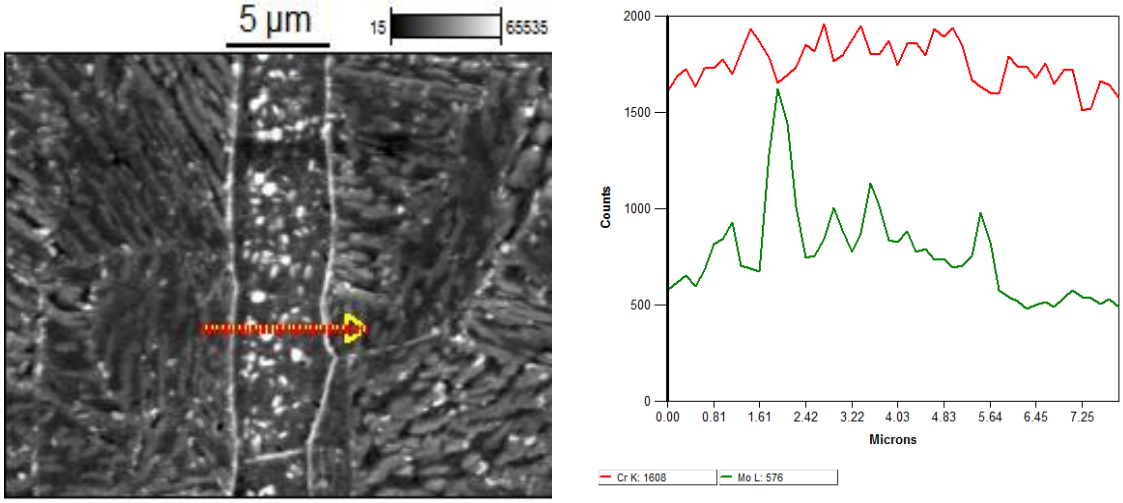


**Figura 12:** Linescan chi-sample heat treated at 670°C for 18h.

## Conclusions

The heat treatment proposed for the samples in order to obtain reverse and remain the austenite retained in the microstructure was successfully. The sub-zero treatment did not destabilize the retained austenite. The χ-phase, or at least a phase rich in Cr and Mo was precipitated in the ferrite grain boundaries and inside the ferrite. The samples chosen for testing in the hydrogen conditions were as-quenched, Chi, LRA, RA and HRA.

## References

[1] Carrouge D. “Transformations in Supermartensitic Stainless Steels.” Tese (PHD), Department of Materials Science and Metallurgy, University of Cambridge, 2002.

[2] Zou D.N., Han Y., Zhang W., Fang X.D. Influence of Tempering Process on Mechanical Properties of 00Cr13Ni4Mo Supermartensitic Stainless Steel. Journal of Iron and Steel Research International 201017(8): 50-54.

[3] Leem D.S, Lee Y.D, Jun J.H. Amount of retained austenite at room temperature after reverse transformation of martensite to austenite in an Fe13%Cr7%Ni-3%Si martensitic stainless steel. Scripta Materialia 2001, 45 (7): 767-772.

[4] Song Y.Y., Li X.Y., Rong L.J., Ping D.H. Yin F.X., Li Y.Y. Formation of the reversed austenite during intercritical tempering in a Fe–13%Cr–4%Ni–Mo martensitic stainless steel Materials Letters 2010, 64: 1411-14.

[5] Escriba D.M., Materna-M. E., Plauta R.L., Padilha A.F. Chi-phase precipitation in a duplex stainless steel. Material Characterization 60 (2009) 1214-1219.

[6] MICHALSKA J., SOZANSKA M. Qualitative and quantitative analysis of σ and χ phases in 2205 duplex stainless steel. Materials Characterization 2006, 56: 355–62.

[7] YANG Y.H., YAN B., WANG J., YIN J.L. The influence of solution treatment temperature on microstructure and corrosion behavior of high temperature ageing in 25% Cr duplex stainless steel. Journal of Alloys and Compounds 2011, 509: 8870– 79.

[8] Santos T.A.A., Carvalho R. N., Rocha A. C., Ferreira M.A.C., Buono V.T.L. Estudo da Reversão da Austenita em um aço inoxidável martensítico-ferrítico. 69º Congresso Anual da ABM – Internacional, 14º ENEMET - Encontro Nacional de Estudantes de Engenharia Metalúrgica, de Materiais e de Minas, 21 a 25 de julho de 2014, São Paulo, SP, Brasil.

[9] Song Y., Li X, Rong L., Li Y. Anomalous Phase Transformation from Martensite to Austenite in Fe-13%Cr-4%Ni-Mo Martensitic Stainless Steel. Materials Science and Engineering A 2011, 528: 4075–79.

[10] Kasper J. S. The ordering of atoms in the chi-phase of the iron chromium molybdenum system. Acta Metallurgica 1954, 2: 456-61.

# *CHAPTER 4 – Methodology, Results and Discussion.*

# *CHAPTER 4*

## *PAPER 1: Influence of microstructure in the hydrogen permeation in martensitic-ferritic stainless steel*

ARTICLE IN PRESS

INTERNATIONAL JOURNAL OF HYDROGEN ENERGY XXX (2015) 1–8

Available online at www.sciencedirect.com

ScienceDirect

journal homepage: www.elsevier.com/locate/he

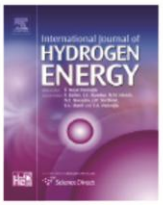


# Influence of microstructure in the hydrogen permeation in martensitic-ferritic stainless steel

D.C.S. Garcia [a,b,*], R.N. Carvalho [a], V.F.C. Lins [b], D.M. Rezende [c], D.S. Dos Santos [c]

[a] Vallourec Tubos do Brasil S.A., Olinto Meireles Avenue 65, Zip Code: 30640-010, Belo Horizonte, Brazil
[b] Chemical Engineering Department, Federal University of Minas Gerais, Antonio Carlos Avenue 6627, Zip Code: 31270901, Belo Horizonte, Brazil
[c] Federal University of Rio de Janeiro, PEMM/COPPE/UFRJ, PO-BOX 68505, 21941-972, RJ, Brazil

ARTICLE INFO

*Article history:*
Received 28 February 2015
Received in revised form
18 June 2015
Accepted 20 June 2015
Available online xxx

*Keywords:*
Hydrogen permeation
Thermal desorption spectroscopy
Stainless steel
Dual-phase
Retained austenite
Chi-phase

ABSTRACT

Martensitic-ferritic stainless steels (MFSS) have been proposed to fulfill an existing gap in material selection, caused by the limited corrosion performance of supermartensitic stainless steels and high costs of duplex stainless steels. This kind of steel basically presents a martensitic-ferritic matrix and, depending on heat treatment schedule, small amounts of retained austenite ($\gamma_{ret}$), chi-phase ($\chi$), carbides and other deleterious phases can form. Since these microstructure features may affect corrosion behavior in different ways, the influence on hydrogen diffusion in a MFSS with different content of retained austenite ($\gamma_{ret}$) and chi-phase ($\chi$) was investigated. Samples were submitted to electrochemical hydrogen permeation and thermal desorption spectroscopy (TDS) techniques. As a result, microstructures have shown different behaviors on hydrogen diffusion. The lower hydrogen apparent diffusion coefficient ($D_{app}$) was obtained for the sample called retained austenite (RA) with 7% of retained austenite, 20% of ferrite and 73% of martensite. The results of TDS showed that retained austenite plays a role as irreversible hydrogen trapping site.

## Abstract

Martensitic-ferritic stainless steels (MFSS) have been proposed to fulfill an existing gap in material selection, caused by the limited corrosion performance of supermartensitic stainless steels and high costs of duplex stainless steels. This kind of steel basically presents a martensitic-ferritic matrix and, depending on heat treatment schedule, small amounts of retained austenite ($\gamma_{ret}$), chi-phase ($\chi$), carbides and other deleterious phases can form. Since these microstructure features may affect corrosion behavior in different ways, the influence on hydrogen diffusion in a MFSS with different content of retained austenite ($\gamma_{ret}$) and chi-phase ($\chi$) was investigated. Samples were submitted to electrochemical hydrogen permeation and thermal desorption spectroscopy (TDS) techniques. As a result, microstructures have shown different behaviors on hydrogen diffusion. The lower hydrogen apparent diffusion coefficient ($D_{app}$) was obtained for the sample called retained austenite (RA) with 7% of retained austenite, 20% of ferrite and 73% of martensite. The results of TDS showed that retained austenite plays a role as irreversible hydrogen trapping site.


**Keywords:** Hydrogen permeation; thermal desorption spectroscopy; stainless steel; dual-phase; retained austenite; chi-phase;

## Nomenclature

MFSS – Martensitic ferritic stainless steel

$\gamma_{ret}$ – Retained austenite

$\gamma$ - austenite

$\chi$ – Chi-phase

$\delta$ – ferrite

$\sigma$ – standard deviation

M – Martensite

$D_{app}$ - hydrogen apparent diffusion coefficient

$D_{appth}$ – theoretical apparent hydrogen diffusion coefficient

$D_{appexp}$ – experimental apparent hydrogen diffusion coefficient

$S_{app}$ – apparent hydrogen solubility

RA – retained austenite sample

Ea – activation energy

$J_\infty$ - the maximum flux

## Introduction

Metallic alloys which are used in oil and gas industry should be inspected and monitored, due the presence of $H_2S$ which may cause premature failure of the equipment, because hydrogen entry in the steel. The steel exposure in the low pH and high $H_2S$ concentration environments can absorb the atomic hydrogen produced by the cathodic reaction from $H_2S$ and penetrate the metallic structure, promoting the Hydrogen Embrittlement (HE) phenomenon [1]. It is important to study the susceptibility of the material to the HE, thus, the materials for most oil and gas applications should be designed to be resistant to HE. For environments containing $CO_2$, stainless steels are an option widely used because besides having satisfactory mechanical properties they have higher general corrosion resistance. Among them, supermartensitic stainless steels have been selected when slight amounts of sulfides are present and, consequently, resistance to HE is required.

Prior to understanding the problem of HE in stainless steels, it is important to assess how the transport of hydrogen takes place, how the diffusion is affected by the different microstructures typically found in this class of material and how hydrogen can travel using different paths inside the material according to the existing phases.

Defects in the steel lattice are traps for hydrogen atoms, being usually distinguished between reversible and irreversible trap sites which are determined by its activation energy (Ea). According to Pressouyre [2,3] if trapping energy exceeds 77 $kJ.mol^{-1}$ (0.79 eV), the trap is considered irreversible, which means the trap can absorb hydrogen until it becomes saturated and release it at a higher temperature. However, if the trapping energy is lower than 60 $kJ.mol^{-1}$ (0.62 eV), the trap is reversible, being able to release hydrogen at lower temperatures. Previous studies have shown that hydrogen may be trapped on dislocations, microvoids, interfaces between inclusions, particles, grain boundaries (e.g. segregation) and precipitates (e.g. particles of TiC) [2-5]. Szost et al [6] report several types of reversible and irreversible traps, such as retained austenite which is irreversible in dual phase steel, and reversible in the high carbon steel.

The retained austenite which has a face-centered cubic crystal structure (fcc) may influence the hydrogen cracking resistance of the steel because of its ability to act as a hydrogen trap due to its low diffusivity. In general, the steel which presents this phase shows a lower diffusion coefficient and higher solubility based on its close packed lattice. In contrast, the ferritic phase which has a body-centered cubic crystal structure (bcc) enables a high diffusion rate and low solubility due to its open lattice structure. Martensite which has a body-centered tetragonal crystal structure (bct) is closer packed than bcc, and the hydrogen diffusion coefficient value is between ferrite and austenite [7]. The χ-phase is body centered cubic (bcc) and it is related to the detrimental effect on ductility, toughness and corrosion resistance. This phase can precipitate in the interface δ/δ, inside the ferrite grains and the interface δ/γ[8]. It is also important to note that austenite found in martensitic or martensitic-ferritic stainless steels is inside the martensite structure as retained austenite. This austenite is quite different configuration of the austenite found in the duplex stainless steels.

The aim of this study is to investigate the influence of steel microstructure on the hydrogen diffusion in a MFSS. In this system, hydrogen permeation occurs in martensitic-ferritic matrix containing an amount of χ and γret. Electrochemical hydrogen permeation and TDS tests were performed to evaluate the phenomenon of hydrogen diffusion in MFSS and correlate it with the microstructure, obtained by an especially designed heat treatment.

## Experimental Details

The composition of the steel used in this research is shown in table 1. The specimens were extracted from seamless stainless steel tube water quenched after a solution treatment at 1000°C for 30 min. In order to produce different microstructures, the specimens were tempered at different temperatures and times followed by water quenching, generating the samples listed in table 2.

**Table 1:** The Chemical Composition of investigated MFSS (wt%)

| C | Cr | Ni | Mo | Mn | Si | S | P |
|---|---|---|---|---|---|---|---|
| 0.012 | 14.00 | 5.00 | 3.00 | 0.32 | 0.2 | 0.002 | 0.014 |

**Table 2:** Sample Identification and heat treatments conditions.

| Sample | Heat Treatment | Microstructure |
|---|---|---|
| As-Quenched | 1000°C 1h, quenching water | 22% Ferrite; 78% Martensite; σ = ± 0.95% |
| Chi | 670°C 18h, quenching water | 21% Ferrite; 66% Martensite; 7% Retained Austenite; 6% Chi σ = ± 2.23% |
| RA | 625°C 1h, quenching water; 600°C 1h, quenching water | 20% Ferrite; 73% Martensite; 7% Retained Austenite σ = ± 1.23% |

The microstructure of each specimen was characterized using different techniques. The relative amount of martensite and ferrite was determined by image analysis using optical microscopy after etching with Lichtenegger-Blöch (LB) solution (20 g ammonium bisulfide, 0.5 g potassium bisulfate, 100 mL water) immersed for 15s [9]. Volume fraction of the retained austenite was determined by X-Ray diffraction (XRD) pattern recorded using a D8 ADVANCE X-ray machine (Cu Kα radiation with λ = 1.5406 Å). Phase transformation was investigated by using a scanning electron microscope (SEM), JEOL JSM 6460 with EDX Thermo/Noran System SIX Model 200 and Chi-phase was estimated by image analysis in optical microscopy after polishing.

In order to calculate the apparent hydrogen diffusion coefficient, electrochemical permeation tests were performed using a Devanathan-Starchusck method [10]. An oxidation cell (detection side) was filled with NaOH 0.1 M and the potential used was obtained from open potentiometric circuit. A reduction cell (charging side) was filled with 3.5% NaCl solution with pH 4.0 (adjusted by $CH_3COOH$). A cathodic current (- 20 mA) was applied on the charging side, and an anodic current was detected on the cell oxidation side [11]. Both currents were generated or detected by AUTOLAB PGSTAT100N potentiostat.

The apparent hydrogen diffusion coefficient ($D_{app}$) was calculated according to equation 1 [12].

$$D_{\text{app}} = 0.5\frac{L^2}{\pi^2 t_b} \quad (1)$$

Where $D_{app}$ is the apparent diffusion coefficient, $L$ is the thickness of the sample and $\boldsymbol{t_b}$ is the breakthrough time.

The apparent hydrogen solubility ($S_{app}$) was calculated according to equation 2 [13].

$$S_{app} = \frac{2}{L}\int_0^t J_c\, dt \qquad (2)$$

Where $S_{app}$ is the hydrogen diffusible in the lattice plus the hydrogen trapped reversibly; and $\int_0^t J_c\, dt$ is the area under the hydrogen permeation curve.

To validate the model used in the calculation of apparent hydrogen diffusion coefficient (equation 1), the theoretical apparent hydrogen diffusion coefficient was calculated by using equation 3 [12].

$$\mathrm{J} = J_\infty \left[1 + 2\sum_1^\infty (-1)^n \; Exp\left(\frac{-n^2\pi^2 Dt}{L^2}\right)\right] \qquad (3)$$

Where $J_\infty$ is the maximum flux.

Thermal desorption spectroscopy (TDS) has been used to study the hydrogen trapping [6]. The technique consists of heating the sample up to 800 °C at a heating rate of 6°C $min^{-1}$ in vacuum environments desorbing the hydrogen detected by a mass spectrometer (QMA200-PFEIFFER). The study was performed on the steel samples in the same solution conditions described for electrochemical hydrogen permeation. To determine the time to hydrogenate the samples, the apparent diffusion coefficient was considered, and the details are in the table 3. The way the samples were hydrogenated is similar to the method used by Hurley et. al. [14] who studied two types of hydrogenation; homogeneous charging using the value of $D_{app}$ versus non-homogeneous charging using the concentration gradient; and concluded that the type using the diffusion coefficient is more efficient in the interpretation of the data, and in the peak definition. The hydrogenation without considering the $D_{app}$ can promote false peak and a wrong de-trapping time.

**Table 3:** Hydrogenation condition of TDS tests.

| Sample | Current Density ($mA.cm^{-2}$) | Thickness (cm) | **Samples size (mm)** | **Hydrogenation** time (h) |
|---|---|---|---|---|
| As-quenched | 43.0 | 0.043 | 3.67 x 20.5 | 3 |
| Chi | | 0.047 | 3.55 x 18.2 | 18 |
| RA | | 0.081 | 2.72 x 15.5 | 24 |

## Results and Discussion

### *Microstructural Characterization*

The results of SEM are shown in figure 1.

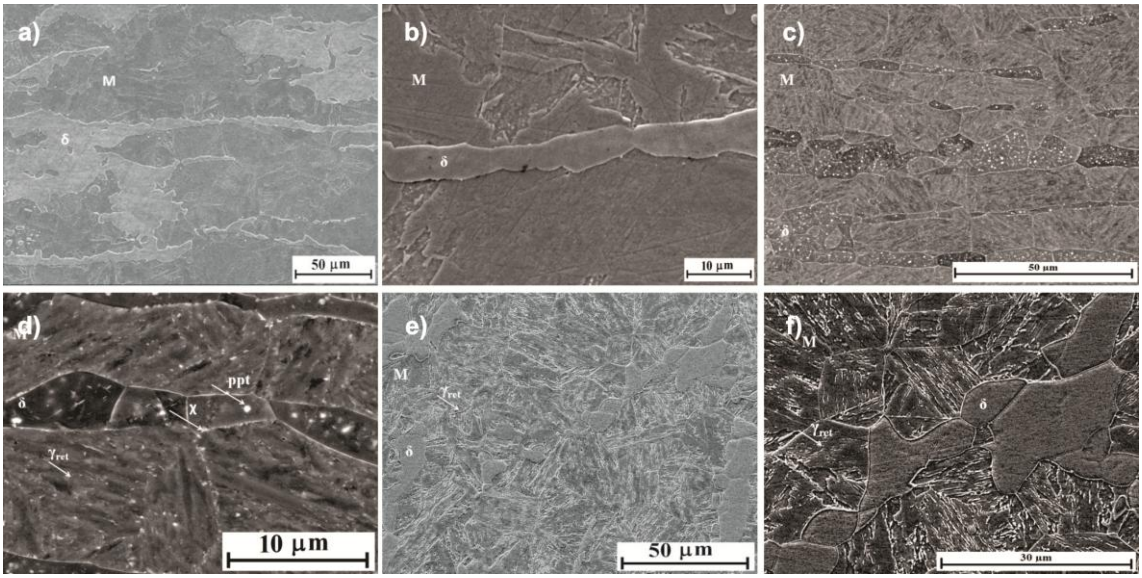


**Figure 1:** SEM (BSE-back scatered electrons) micrography results, a) as-quenched 500x b) as-quenched 2000x, c): Chi 1300x d) Chi 5000x; 1e) RA 2000x f) 5000x

The as-quenched sample (figure 1a and 1b) shows the two predominant phases: ferrite (δ) with higher contents of Mo and Cr and martensite (M) with a higher content of Ni, with prior austenite grain size ASTM 8.7 ± 0.2 corresponding to 15.9 ± 1.4 µm. Due to rolling, both martensitic and ferritic grains become more elongated and, due to the low carbon content, the martensite is formed by laths arranged in the packet form [15,16]. In that sample, it was not possible to observe retained austenite, using XRD pattern.

The chi sample (figure 1c and 1d) was heat treated at a higher temperature (670°C) and long soaking time (18h) in order to maximize the formation of chi-phase, with prior austenite grain size ASTM of 8.9 ± 0.2 corresponding to 14.8 ± 1.9 µm. As a consequence, there was the formation of $\gamma_{ret}$ (see white arrows) and precipitates rich in Mo and Cr inside the ferrite, at the ferrite grain boundaries and at martensite-ferrite interphase boundaries, which were characterized by SEM as χ (see white arrows). Escriba et. al [8] studied a duplex stainless steel and also identified thin precipitated phases at grain boundaries, rich in Cr and Mo, characterized as chi-phase. The chemical

composition of this phase showed a high concentration of Mo and Cr in the precipitate inside the ferrite, and at the grain boundaries. The results found here are in agreement with the results of Escriba **et. al.** [8], which found **χ-phase** in the same region (ferrite/interface) for different times of annealing. Other authors [17,18] reported that chi phase can be rich in Mo and Cr with stoichiometry $Fe_{36}Cr_{12}Mo_{10}$ and/or $(Fe,Ni)_{36}Cr_{18}Mo_4$.

The RA sample (figure 1e and 1f) shows ferritic and martensitic phases with fine white lines indicated with white arrows, spread over the martensite laths, characterizing the retained austenite. The prior austenite grain size is ASTM 9.1 ± 0.2 corresponding to 13.6 ± 0.93 μm.

***XRD Results***

Figure 2 shows the XRD results, for all different microstructures studied.

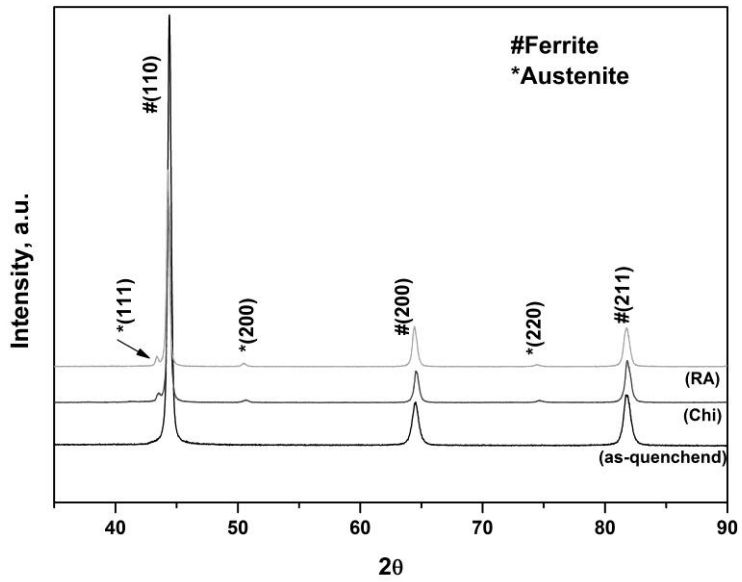


**Figure 2:** XRD results: as-quenched, Chi and RA.

It is possible to observe that the matrix of all samples have martensite and delta-ferrite structure (δ), and the peak of each phase has the same reflection in the interval of 30 to 90° for the plans (110), (200) and (211), and it may not be differentiated. The lattice parameter of ferrite (bcc) is close to the lattice parameter of martensite after water

quenching (bct) causing the peaks to overlap. The difference between these phases appears just from the plan (310) as they would decompose in ferrite and cementite [19]. Furthermore it is important to highlight the fact that this material has low carbon content and, consequently, the tetragonality of martensite is lower. In the as-quenched sample, the amount of ferrite was 100%, but using an image analyzer it was possible to quantify 78% of martensite and 22% of ferrite.

The austenite phase appears in the (111), (200) and (220) plans for chi and RA samples. This occurred because the tempering temperature used reverted the martensite transformation and stabilized this phase after cooling. Observing the X-ray pattern for the chi sample, it was not possible to identify the chi-phase. There are two considerations that are to be made: the technique was not suitable for phase identification and quantification; the amount of the transformed phase was too low; so that the technique was not sensitive enough to identify and quantify it. To quantify these phases (RA, δ and M), the Rietveld method was used. The technique was developed by Hugo M. Rietveld in 1969 and consists of adjusting the theoretical diffraction standard with the experimental data using the least-square method [20].

To quantify the χ-phase in the chi sample, the image analyzer technique was used. This phase has been considered to be the precipitated phase inside the ferrite grains, at the grain boundaries, and at the ferrite/martensite interphase. It is indicated in white color in figure 3. To obtain the content of this phase, five images obtained using SEM were analyzed and the content of 6 ± 1.3% was identified.

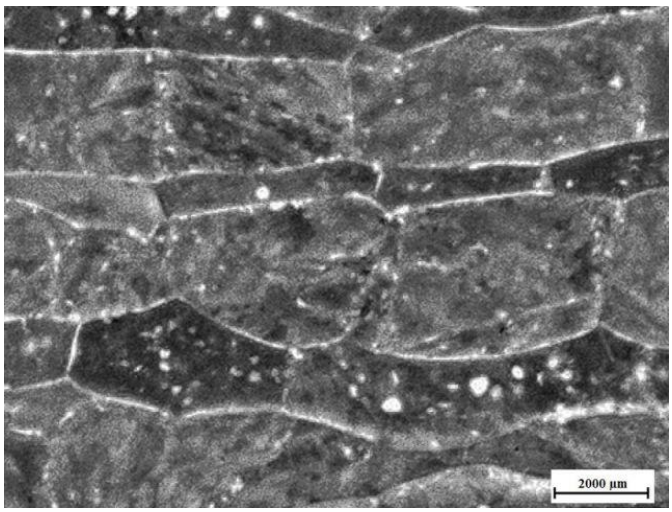


**Figure 3:** Chi-phase identification using image analyzer.

The **RA** results show ferrite and austenite, and the amount of austenite obtained using the Rietveld method [20] was 7% of retained austenite and 93% of martensite/ferrite. Considering the results of image analyzer, the phase contents were 20% of ferrite, 7% of retained austenite and 73% of martensite. For identification and quantification of the phases found in the material under study, different techniques were used such as XRD diffraction and image analysis. A complex microstructure requires the use of more than one technique for phase identification, because there are phases with different morphologies and difficult to identify. In this case, one technique complements another.

***Hydrogen permeation***

The experimental hydrogen permeation and theoretical model (continuous line) calculated by equation 3 are compared in figure 4, and the $D_{app}$ and $S_{app}$ theoretical versus experimental are shown in table 4.

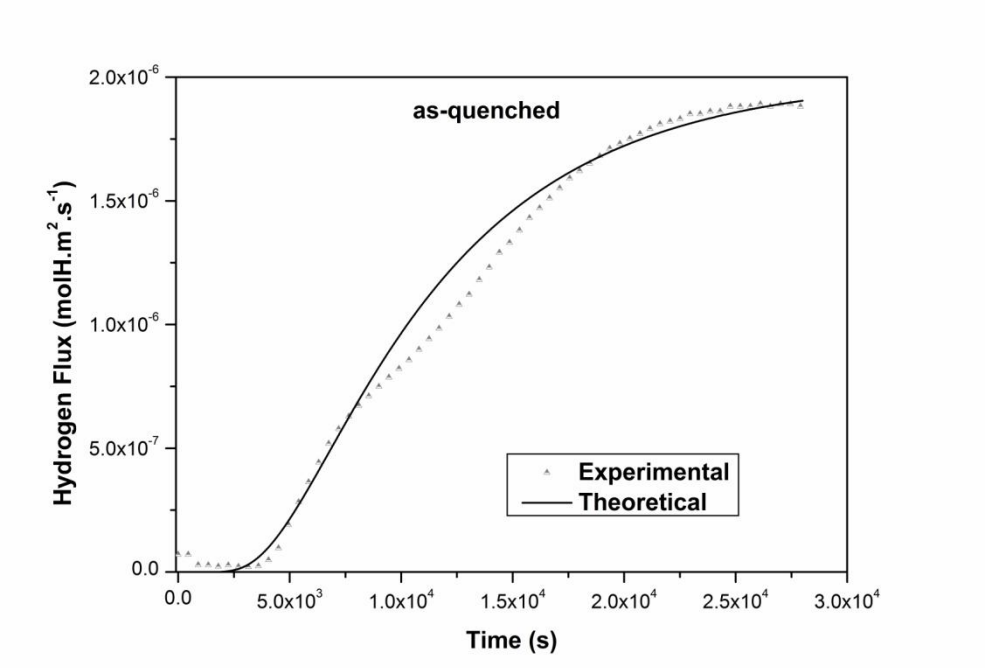


**(a)**

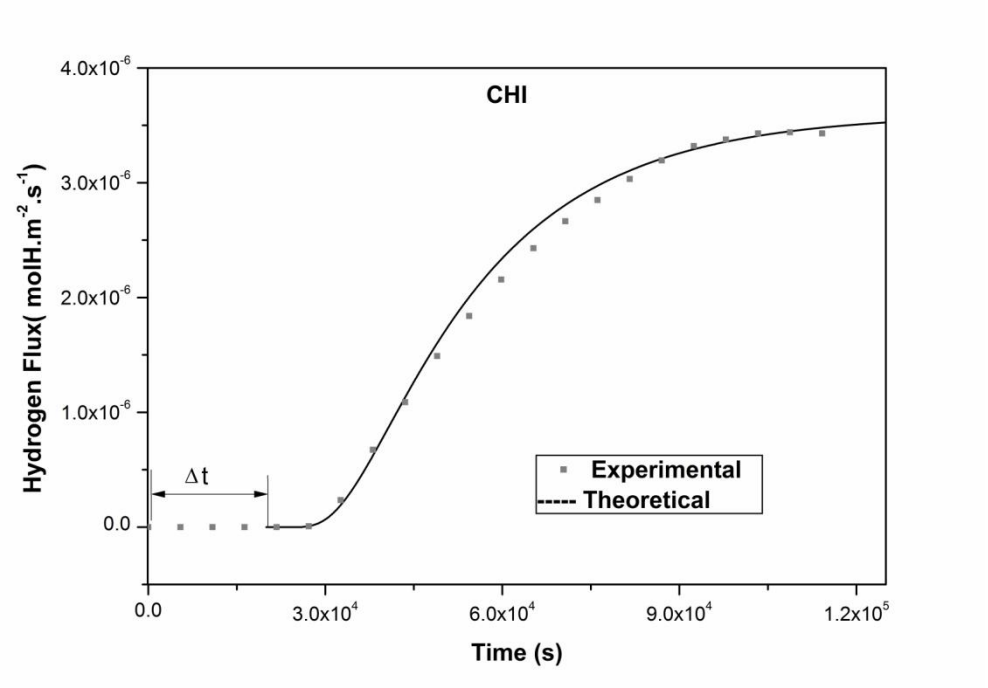


**(b)**

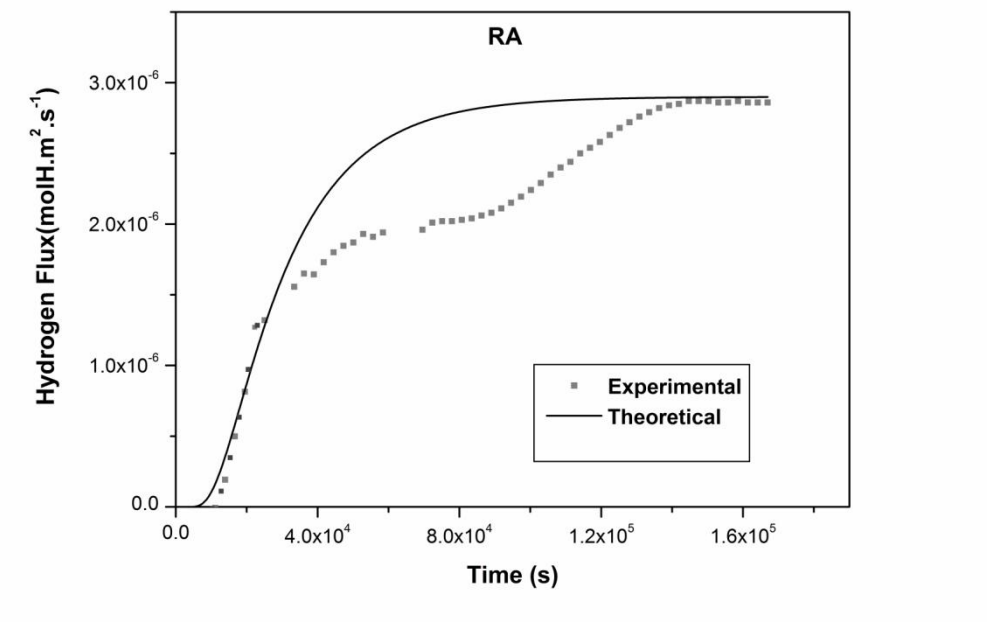


**(c)**

**Figure 4** Electrochemical hydrogen permeation curves for: a) as-quenched; b) Chi; c) RA.

**Table 4:** Data of experimental versus theoretical for area (A), diffusion coefficient (D), solubility (S) and sample thickness (L) in martensitic/ferritic stainless steel.

| Sample | $A_{exp}$ ($m^2$) | $A_{th}$ ($m^2$) | $S_{app}$ ($mol.H.m^{-3}$) | $S_{th}$ ($mol.H.m^{-3}$) | $D_{th}$ ($m^2.s^{-1}$) | $D_{exp}$ ($m^2.s^{-1}$) | L (m) |
|---|---|---|---|---|---|---|---|
| as-quenched | 0.02914 | 0.3211 | 105 | 116 | $4.1x10^{-12}$ | $3.9x10^{-12}$ | $5.5x10^{-4}$ |
| chi | 0.2761 | 0.2761 | 904 | 904 | $2.1x10^{-12}$ | $2.1x10^{-12}$ | $6.9x10^{-4}$ |
| RA | 0.3312 | 0.3840 | 1577 | 1828 | $9.0x10^{-13}$ | $7.8x10^{-13}$ | $4.2x10^{-4}$ |

Theoretical curves fitted experimental data well, but due to the presence of traps in the microstructure there is a slightly difference between theoretical and experimental results for all samples, theoretical results presented a higher value than experimental ones, which can be explained as the model does not consider the hydrogen trapping effect. The microstructure studied in this work presented different phases (M, δ, $\gamma_{ret}$ and χ-phase) and precipitates rich in Mo and Cr affecting hydrogen diffusion on metallic structures. Fallahmohammadi et al. [21,22] also found difference between the theoretical versus experimental permeation curve using solution of Fick's second law, due to the fact that the permeation curve is the result of the diffusion process controlled and the physic-chemical reactions of hydrogen with traps of different types: reversible, irreversible, saturable, and non-saturable traps. The definition of a complete permeation curve using a single constant parameter is difficult.

The curve in figure 4a shows the results of electrochemical hydrogen permeation experimental versus theoretical for as-quenched specimen. The curve presents a deviation of a sigmoid shape; however, the adjustment from equation 4 presented just 9% of difference between the area under the curve of theoretical versus experimental; thus the values of diffusibility, solubility and permeability obtained from the experimental curve are in good agreement with the theoretical results. Deviation in the permeation curves in biphasic samples is expected mainly due to the difference between diffusibility of ferritic phase ($10^{-9}$ $m^2/s$) and martensitic phase ($10^{-13}$ $m^2/s$). This anomalous behavior (non sigmoid shape) is originated from the permeation in the interfaces of δ/M. The experimental apparent diffusion coefficient was $D_{appexp} = 3.9x10^{-12}$ $m^2.s^{-1}$ in M/δ microstructure. As reported by Olden [16], the hydrogen diffusion coefficient is $10^{-9}$ $m^2.s^{-1}$ for ferrite and $10^{-12}$ to $10^{-13}$ $m^2.s^{-1}$ for martensite at 25°C. In this microstructure, hydrogen permeates consecutively between martensitic and ferritic grain, accelerating or decelerating, and results in a significant change in the value of the

coefficient, i.e. higher than that reported for ferrite and lower for martensite. The predominance of the value characteristic of martensite could be due to the lack of connectivity between the grains of ferrite δ (no short - circuit) in that material. The solubility ($S_{app}$) is proportional to the area under the experimental versus theoretical curves (table 3). The high value of solubility is characteristic of the martensite structure that dissolves a large amount of hydrogen and displays low diffusibility.

Figure 4b shows the results of hydrogen permeation in the sample containing χ- phase precipitated. The chi-phase samples presented an apparent hydrogen diffusion coefficient $D_{appexp}$ = 2.1 x$10^{-13}$ $m^2.s^{-1}$. It is important to highlight that the chi samples, after heat treatment for 18 h in 670 °C, presented a microstructure with ferrite, martensite, 7% of $\gamma_{ret}$ and 6% of χ-phase.

At the beginning of permeation (Δt), the experimental curve presented a delay which can be attributed to the completion of the deep traps sites. During this time, no hydrogen permeates through the sample. After this filling, hydrogen permeation occurred across the samples and the curve presented a good adjustment of a theoretical curve. Calculating the value of the hydrogen concentration required to initially fill the deep traps, considering the fact that the efficiency of cathodic current is limited to the J∞, the value obtained from Faraday's law gives a $S_{app}$ = 104 molH.$m^{-3}$, to which must be added to the solubility found from the theoretical adjustment. The simple calculation, using the Fick's second law, provides $S_{app}$ value higher than that obtained from theoretical adjustment, which reinforces the necessity to analyze the curve from the theoretical adjustment. Literature [23, 24, 25] reported modifications in Fick's law to incorporate the trapping effects in the permeation curve, however the presence of martensite, ferrite, $\gamma_{ret}$, χ-phase, and precipitates in these samples produces a complex analysis.

Fig. 4c shows the experimental and theoretical results of RA samples. In this sample, experimental apparent diffusion coefficient was $D_{appexp}$ = 7.8x$10^{-13}$$m^2.s^{-1}$. This sample has no precipitates in ferrite thus making the diffusion more clearly defined. Chan et. al [26] evaluated the effect of quenched and quenched + subzero temperature treatments on the Fe-Mn-C steel with different carbon contents. The steel quenched with high carbon content presented a higher amount of retained austenite than the same material quenched + subzero temperature. As a consequence, the greater the retained austenite the slower the hydrogen diffusion coefficient, which can be explained due to the interfaces between austenite and matrix offer additional trapping sites for hydrogen. As reported by Olden et. al. [16], the greater the diffusion path and the higher the

tortuosity, the greater the amount of retained austenite, the lower the hydrogen diffusion coefficient of the sample, since this phase acts as trap for hydrogen. Olden et al. [16] have also found that in supermartensitic stainless steel, the higher the volume fraction of retained austenite in the sample the greater the delay in the diffusion coefficient. The results of Olden et al. [16] are in good agreement with the results found in this work, which showed a slow $D_{app}$ for the samples with retained austenite (chi and RA samples). In terms of solubility ($S_{app}$), a strong deviation in the sigmoid shape of the experimental versus theoretical curves is observed, representing a difference of 14% in value. The solubility values (table 3) for RA sample were even higher (10 times) than those obtained for the as-quenched samples. This result can be explained by the presence of the new phase ($\gamma_{ret}$) that contributes with more trap interfaces (deep traps).

Diffusion in martensite is low, but higher than in chi and RA samples. The precipitation of retained austenite indicates an increase of trapping and a decrease in the diffusion, since the precipitation of $\chi$-phase captures solute elements and tempers the microstructure favoring the diffusion in this sample with $\gamma_{ret}$, although the $D_{app}$ is similar to both samples.

In order to compare solubility results for all samples, the as-quenched sample ($S_{app}$ = 116 molH.m$^{-3}$) can be regarded as a reference for having only $\delta$+M, and may present residual retained austenite. The quenching and tempering treatments to obtain $\gamma_{ret}$ promote a reduction in the martensite due to the tempering which could lead to a decrease in the apparent solubility. However, the new M-$\gamma_{ret}$ interface contributes heavily to the increase in apparent solubility in the RA sample ($S_{app}$ = 1828 molH.m$^{-3}$). For the chi sample, even though the presence of $\chi$-phase and $\gamma_{ret}$, which absorb a large amount of hydrogen, the effects of a prolonged heat treatment (18 hours) in 670°C contribute to a greater diffusion of substitutional elements and consequently precipitations. Furthermore, there is a greater reduction in the microstructure defects and a reduction in the total solubility ($S_{app}$ = 904 molH.m$^{-3}$).

In figure 5, there is a schematic model to show the hydrogen paths across the different microstructures studied in this work. The presence of ferrite in martensitic matrix promotes a short circuit due to the high diffusivity in this stage. On the other hand, the interfaces between ferrite/martensite and/or martensite/retained austenite contribute to trap hydrogen in the matrix, causing a delay in the permeation and a new permeation in other stage.

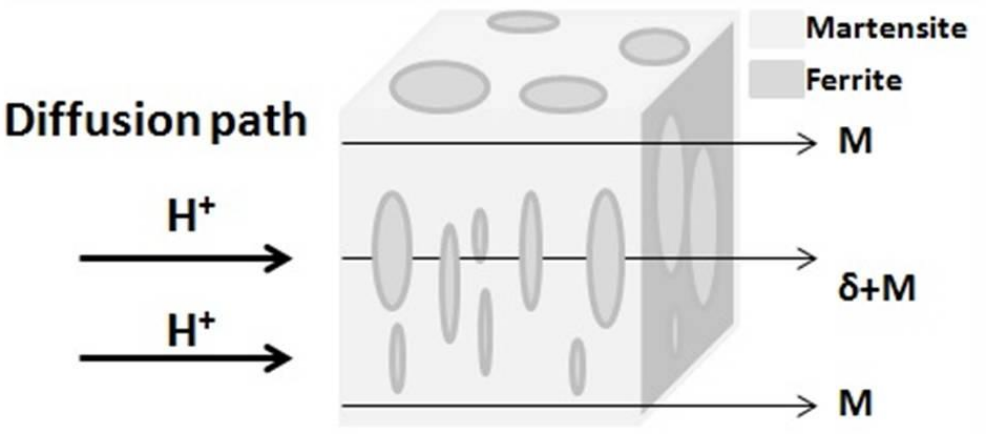


**Figure 5** Diffusion model schematic in martensitic/ferritic stainless

***Thermal Desorption Spectroscopy Results***

The results of TDS are shown in figure 6.

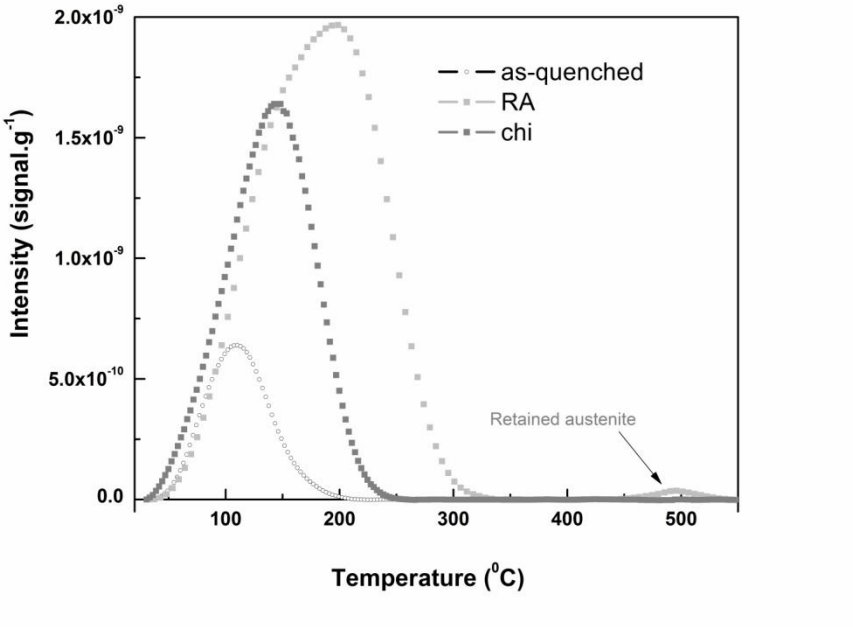


**Figure 13** Thermal Desorption Spectroscopy as-quenched, Chi and RA

A peak in low temperatures is observed for all samples tested: 109, 143 and 195°C for as-quenched, chi and RA, respectively. Desorption temperature is a characteristic of sites with defects, dislocations, clusters, grain boundaries and elastic stress responsible to trap hydrogen reversibly or de-trap the diffusive hydrogen from the lattice sites [27].

The as-quenched sample presented a more shifted peak to the lowest temperature (109°C) which means that hydrogen was weakly trapped and thus released at a lower temperature. It is important to highlight that the martensite in this specimen was not tempered, and the fast water quenching introduced a high degree of lattice strain in the martensite which acts as efficient reversible traps for hydrogen [28].

The chi sample presented the first desorption peak which shifted to a slightly higher temperature (143°C) for as-quenched, but a lower temperature than the RA sample. Wei et al. [29] report that the hydrogen storage capacity is directly related to the nature and quantity of those interfaces in the material as well as the size and the amount of precipitates, beyond the capacity of each phase. This peak which shifted to a higher temperature is consistent with the data reported by Wei et al. [29].

In the RA sample, the first peak shifted to a higher temperature (195°C). This phenomenon can be associated to a higher quantity of interface, γ/M and γ/δ, due to the volumetric fraction of $\gamma_{ret}$ precipitated after tempering. Literature [6,30] reports that the retained austenite can act as irreversible site with high activation energy and high temperature in the spectrum, or reversible site with low activation energy and low temperature peaks appearing in the spectrum [6,30]. As reported by Szost et al. [6], the peak at 215°C was due to γret, the coherent interface α/γret was reversibly trapped in nanobainitic steel, but literature also reports the trapping for hydrogen in M/γ interfaces or inside the γ, that could occur in the case of RA samples; the trap was carried out into the γ, and shifted the peak to a higher temperatures.

The RA specimen presented a second peak at 492°C that can be explained by the retained austenite phase. Escobar et al [31] studying a TRIP steel with different retained austenite content, identified a de-trapping peak at 500°C, attributed to the retained austenite presented in this material. Escobar et al [31] mentioned that the interaction of the hydrogen with this phase can be strong enough to be necessary a higher energy and temperature for hydrogen release. It is important to highlight the influence of amount and morphology of the retained austenite in the capacity of hydrogen trapping. Thinner precipitates can result in coherent interface with more reversible characteristics, and thicker precipitates will present incoherent interface resulting in irreversible sites. This fact can be confirmed by other studies such as Szost et al [6] and Park et al [30].

## Conclusions

The influence of microstructure in the hydrogen permeation in martensitic/ferritic stainless steel has been studied using the electrochemical hydrogen permeation and thermal desorption spectroscopy techniques. The RA samples presented the lowest diffusion coefficient and the highest solubility. Despite the solution of Fick's second law which does not predict the trapping effect, the used adjustment showed a good agreement with experimental curves and the deviation occurs due to the deep traps created by heat treatment.

The permeation experiments indicate that $D_{app}$ decreases as the amount of $\gamma_{ret}$ and chi-phase increases. This study establishes that $\gamma_{ret}$ can trap hydrogen irreversibly.

**Acknowledgments**

The authors would like to sincerely thank Vallourec Tubos do Brasil, CNPq and CAPES for their financial support.

## References

[1] Beidokhti B; Dolati A; Koukabi AH. Effects of alloying elements and microstructure on the susceptibility of the welded HSLA steel to hydrogen-induced cracking and sulfide stress cracking. Materials Science and Engineering A 2009; 507: 167-73.

[2] Pressouyre GM. Trap theory of hydrogen embrittlement. Acta Metallurgica 1979; 28:895-11.

[3] Pressouyre GM, Bernstein IM. An Example of the Effect of Hydrogen Trapping on Hydrogen Embrittlement. Metallurgical Transactions 1981; 12A: 835-44.

[4] Pressouyre GM. Hydrogen traps, repellers, and obstacles in steel; consequences on hydrogen diffusion, solubility, and embrittlement. Metallurgical Transactions A 1983; 14A: 2189-93.

[5] Pressouyre G. A classification of hydrogen traps in steel. Metallurgical Transaction 1979; 10A:1571-73.

[6] Szost BA, Vegter RH, Rivera-Díaz-del-Castillo PEJ. Hydrogen trapping mechanisms in nanostructured steel. Metallurgical and Materials Transactions 2013; 44A: 4542-50.

[7] Solheim KG, Solberg JK, Walmsley J, Rosenqvist F, Bjørnå TH. Hydrogen Induced stress cracking in supermartensitic stainless steels – Stress threshold for coarse grained HAZ. Engineering Failure Analysis 2013; 34:140.

[8] Escriba DM, Materna-Morris E, Plaut RL, Padilha AF. Chi-phase precipitation in a duplex stainless steel. Materials Characterization 2009; 60:1214-19.

[9] Bramfitt BL, Benscoter AO. Metalographer's guide Practices and Procedures for Irons and Steels. ASM International 2002; 237.

[10] ISO 17081:2004(E), Method of Measurement of Hydrogen permeation and Determination of Hydrogen Uptake and Transport in Metals by an Electrochemical Technique, ISO, Switzerland, 2004.

[11] Santos DS, Miranda PEV. Hydrogen solubility in amorphous and crystalline materials. International journal of hydrogen energy 1998; 23: 1011-17.

[12] Boes N, Zuchner H. Eletrochemical methods for studying diffusion permeation and solubility of hydrogen in metals. Journal of the Less-Common Metals 1976; 49: 223-40.

[13] Kircheim R. Hydrogen solubility and diffusivity in defective and amorphous metals. Progress in Materials Science1988; 32: 261-25.

[14] Hurley C, Martin F, Marchetti L, Chêne J, Blanc C, Andrieu E. Numerical modeling of thermal desorption mass spectroscopy (TDS) for the study of hydrogen diffusion and trapping interactions in metals. International journal of hydrogen energy 2015; 40:3402-14.

[15] Bilmes PD, Solari M, Llorente CL. Characteristics and effects of austenite resulting from tempering of 13Cr–NiMo martensitic steel weld metals. Materials Characterization 2001; 46:285-96.

[16] Olden V, Thaulow C, Johnsen R. Modelling of hydrogen diffusion and hydrogen induced cracking in supermartensitic and duplex stainless steels. Materials & Design 2008; 29:1934–48.

[17] Wernick JH. Topologically close-packed structures. In: Westbrook JH, Fleischer RL. Intermetallic Compounds. New York 1967.

[18] Tottem GE. Steel Heat Treatment: metallurgy and technologies 2006. 2nd editionTaylor & Francis Group, LLC

[19] Cullity BD, Stock SR. Elements of X-Ray Diffraction 2001; 3rd edition Prentice Hall Inc., New Jersey.

[20] Rietveld HM. A profile refinement method for nuclear and magnetic structures. J. Appl. Crystallogr. 1969; 2:65-71.

[21] Fallahmohammadi E, Bolzoni F, Lazzari L. Measurement of lattice and apparent diffusion coefficient of hydrogen in X65 and F22 pipeline steels. International journal of hydrogen energy 2013; 38:2531-43.

[22] Fallahmohammadi E, Bolzoni F, Fumagalli G, Re G, Benassi G. Hydrogen diffusion into trhee metallurgical microstructure of a C-Mn X65 and low alloy F22 sour service steel pipelines. International journal of hydrogen energy 2014; 39:13300-13.

[23] McNabb A, Foster PK. A new analysis of the diffusion of hydrogen in iron. Journal Transactions of the Metallurgical Society of AIME 1963;119:691-4.

[24] Oriani RA. The physical and metallurgical aspects of hydrogen in metals. Fourth international conference on cold fusion. 1993. p. 1-42.

[25] Pressouyre GM, Bernstein IM. Quantitative analysis of H trapping. Metallurgical Transactions A 1978;9A:1571.

[26] Chan SLI, Lee HL, Yang JR. Effect of retained austenite on the hydrogen content and effective diffusivity of martensitic structure. Metallurgical Transactions A 1991; 22A:2579-86.

[27] Escobar DP, Duprez L, Verbeken K. Identification of the hydrogen trap sites in a high strenght TRIP steels by means of Thermal Desorption Spectroscopy. In: Effects of hydrogen on materials: Proceedings of the 2008 International Hydrogen Conference 2008; Wyoming, EUA 485-92.

[28] Parvarthavarthini N; Saroja S. Studies on hydrogen permeability of 2.25% Cr-1% Mo ferritic steel: correlation with microstructure. Journal of Nuclear Materials 2001; 288: 187-96.

[29] Wei FG, Hara T, Tsuzaki K. Nano Precipitates design with hydrogen trapping character in high strenght steels. In: Effects of hydrogen on materials: Proceedings of the 2008 International Hydrogen Conference 2008; Wyoming, EUA 448-55.

[30] Park BYD, Maroef IS, Landau A. Retained Austenite as a hydrogen trap in steel welds. Welding Research 2002; 27-35.

[31] Escobar DP, Depover T, Duprez L, Verbeken K, Verhaege M. Combined thermal desorption spectroscopy, differential scanning calorimetry, scanning electron

microscopy and X-ray diffraction study of hydrogen trapping in cold deformed TRIP steel. Acta Materialia 2012; 60: 2593-05.

# *CHAPTER 4*

## *PAPER 2: Influence of Retained Austenite in the Hydrogen Diffusion in Martensitic-Ferritic Stainless Steel*

*(Paper submitted to International Journal of Hydrogen Energy in 2015/October)*

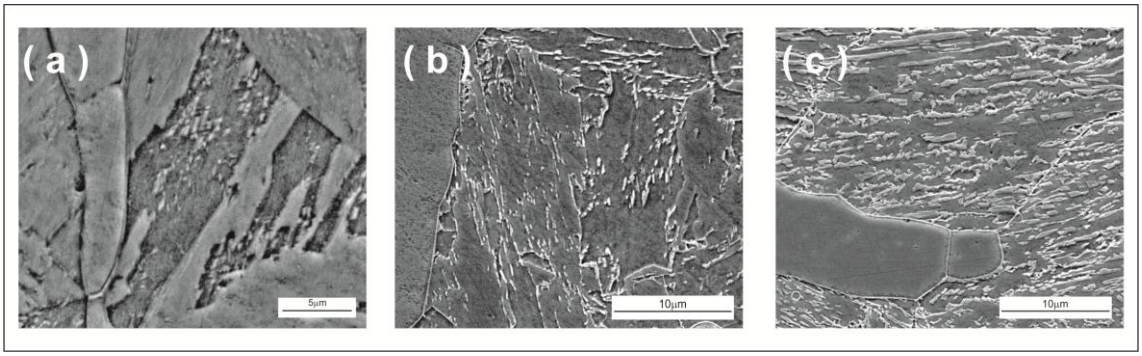

## Abstract

The effect of retained austenite on hydrogen permeation behavior was investigated by electrochemical hydrogen permeation technique developed by Devanathan-Starchusck. The samples were extracted from seamless stainless steel tube water quenched after a solution treatment at 1000°C for 30min and heat treated in different tempering temperatures in order to achieve different contents of retained austenite. As a result, the concentration of retained austenite ($\gamma_{ret}$) in martensitic-ferritic stainless steel affected the hydrogen diffusion and the retained austenite morphology has shown a significant effect on hydrogen permeation. The lower hydrogen apparent diffusion coefficient ($D_{app}$) was obtained for the sample called high retained austenite (HRA) with 22% of $\gamma_{ret}$. and the high solubility was obtained for the sample called medium retained austenite (RA).


## Introduction

Due to the improvement on the corrosion performance compared with supermartensitic stainless steel (SMSS) and the low cost compared to duplex stainless steel (DSS), martensitic-ferritic stainless steels (MFSS) have been proposed to substitute the SMSS and DSS in sour environments of oil industry. The mainly microstructure of this material is constituent of martensite plus ferrite phase, but some retained austenite can be formed during the heat treatment. Depending on the heat treatment temperature, this complex microstructure can be modified and the performance of the material could be also affected.

This new class of steel (MFSS) contains a significant percentage of Ni to reduce the Ac1 transformation temperature (Ac1 temperature corresponds to austenite transformation start) and to decrease the temperature transformation of martensite (Mf) to below the room temperature. As a result, transformed reverse austenite precipitates during tempering close to Ac1. After tempering and during cooling, reverse austenite sometimes remains as retained austenite ($\gamma_{ret}$) [1].

Thus, retained austenite is formed during the tempering process and its volume is influenced by the tempering temperature and process [2]. The content of retained austenite, which is untransformed to martensite during cooling stage, may affect the mechanical and fatigue properties, ductility and hydrogen embrittlement [3,4].

It is known that the finely dispersed austenite phase increases the solubility and decreases the diffusion rate of hydrogen when compared to ferrite and martensite phase. Thus, the retained austenite in steels forms traps, which are able to bind hydrogen strongly and the austenitic constituent effectively acts as a hydrogen trap in martensitic or ferritic steel [4, 5]. According to Szost et. al. [6], the retained austenite acts as irreversible trap in dual phase steel, and as reversible trap in high carbon steel.

In order to study the hydrogen interaction with the steel microstructure, different methods can be used. The electrochemical hydrogen permeation technique developed by Devanathan and Starchurscki [6] is widely used to measure the diffusivity, solubility and permeability of hydrogen in the material, and gives information on the density of trap sites and the binding energy of the dominant reversible trap site.

The aim of this study is to investigate the influence of retained austenite on the hydrogen diffusion in MFSS. In this system, the hydrogen permeation occurs in martensitic-ferritic matrix containing 2 and 22% of $\gamma_{ret}$. Electrochemical hydrogen permeation was performed to evaluate the phenomenon of hydrogen diffusion in MFSS and correlate it with the steel microstructure, obtained by an especially designed heat treatment. The results obtained in this study will be compared with a previous work [7] developed in the same material with different heat treatment containing 7% of $\gamma_{ret}$ and chi-phase ($\chi$).

## Experimental Details

The experimental details were performed at the same way cited in the previous work [7], and the specimens were extracted from seamless stainless steel tube water quenched after a solution treatment at 1000°C for 30min and heat treated as shown in table 1. The chemical composition of the steel studied in this research is shown in table 2.

**Table 1:** Sample identification, heat treatments conditions and steel microstructure.

| Sample | Heat Treatment | Microstructure | Reference |
|---|---|---|---|
| As-Quenched | 1000°C 1h, quenching water | 22% Ferrite; 78% Martensite; σ = ± 0.95% | [7] |
| Chi | 670°C 18h, quenching water | 21% Ferrite; 66% Martensite; 7% Retained Austenite; 6% Chi σ = ± 2.23% | [7] |
| Low Retained Austenite (LRA) | 600°C 1h, quenching water | 20% Ferrite; 78% Martensite; 2% Retained Austenite σ = ± 4.6% | Present Work |
| RA | 625°C 1h, quenching water; 600°C 1h, quenching water | 20% Ferrite; 73% Martensite; 7% Retained Austenite σ = ± 1.23% | [7] |
| High Retained Austenite (HRA) | 675°C 1h, quenching water; 600°C 1h, quenching water | 20% Ferrite; 58% Martensite; 22% Retained Austenite; σ = ± 1.0% | Present Work |

**Table 2:** The Chemical Composition of investigated MFSS (wt%)

| C | Cr | Ni | Mo | Mn | Si | S | P |
|---|---|---|---|---|---|---|---|
| 0.012 | 14.00 | 5.00 | 3.00 | 0.32 | 0.2 | 0.002 | 0.014 |

The steel microstructure was investigated by using a scanning electron microscope (SEM), JEOL JSM 64060. In order to distinguish the morphology of retained austenite, the relative area of austenite grain was evaluated using an image analyzer with ImageJ program. The relative amount of martensite and ferrite and XRD pattern was obtained according to the previous work [7].

Conversion electron Mössbauer spectrometry (CEMS) analyses were now used to identify and quantify the retained austenite and chi phases, in an effort to improve further the reportedly microstructural characterization of the same material of our previous work [7]. These analyses were made with a constant acceleration in the CEMS setup mode, using a ~80 mCi $^{57}$Co source in Rh matrix, at room temperature. The gamma ray-detector was a proportional counter with a flowing gas composed of a work mixture of 95% He and 5% $CH_4$. The collected data were numerically fitted with the NORMOS 90® computer program [8].

These results were analyzed basing mainly on the isomer shift (δ) values, which is a spectrometric parameter that reflects the s-electron density at the $^{57}$Fe nucleus, providing clues about the: (i) oxidation state of iron composing the sample; (ii) electronegativity of the ligands and (iii) electronic configuration. These isomer shift

values are relative to the natural Fe (αFe) [9]: The isomer shift is spectrometrically taken as the distance between the centroid of the spectrum for the sample and the zero velocity of the scale set from the αFe spectrum at the same experimental conditions; the positive velocity corresponds to the source moving toward the absorber [10]. The obtained 298 K-Mössbauer spectra are plotted as the relative transmission of gamma rays versus the Doppler velocity of the radioactive source.

The hydrogen permeation also used the same method cited in the previous work [7] using Devanathan-Starchusck method [11], with a 3.5% NaCl aqueous solution with pH 4.0 adjusted by $CH_3COOH$ on the charging side, and with a NaOH 0.1M solution on the detection side. The cathodic current used was -20mA on the detection side, and the potential obtained from open potentiometric circuit was used on the cathodic side [12].

The apparent hydrogen diffusion coefficient ($D_{app}$) was calculated according to equation 1 [13].

$$D_{\text{app}} = 0.5\frac{L^2}{\pi^2 t_b} \qquad (1)$$

Where $D_{app}$ is the apparent diffusion coefficient, $L$ is the thickness of the sample and $\boldsymbol{t_b}$ is the breakthrough time.

The apparent hydrogen solubility ($S_{app}$) was calculated according to equation 2 [14].

$$S_{app} = \frac{2}{L}\int_0^t J_c\, dt \qquad (2)$$

Where $S_{app}$ is the hydrogen diffusible in the lattice plus the hydrogen trapped reversibly; and $\boldsymbol{\int_0^t J_c\, dt}$ is the area under the hydrogen permeation curve. The theoretical diffusion coefficient diffusion was calculated in order to validate the model used in the calculation of apparent hydrogen diffusion coefficient.

## Results and Discussion

The discussion will be done in the samples studied at the present work (LRA and HRA samples) comparing with the results obtained in the previous work from these authors (as-quenched, chi and RA samples).

### *Microstructure characterization*

#### *XRD results*

The volume fraction of austenitic phase examined by XRD measurement (fig. 1) is 2% for LRA and 22% for HRA. Using this technique the detection of any other phase

besides ferrite and austenite was not possible. The analysis performed by XRD Synchrotron identified besides the austenite and ferrite phase, traces of precipitates such as $Cr_{23}C_6$ in the HRA sample, but the quantification of these precipitates was not viable.

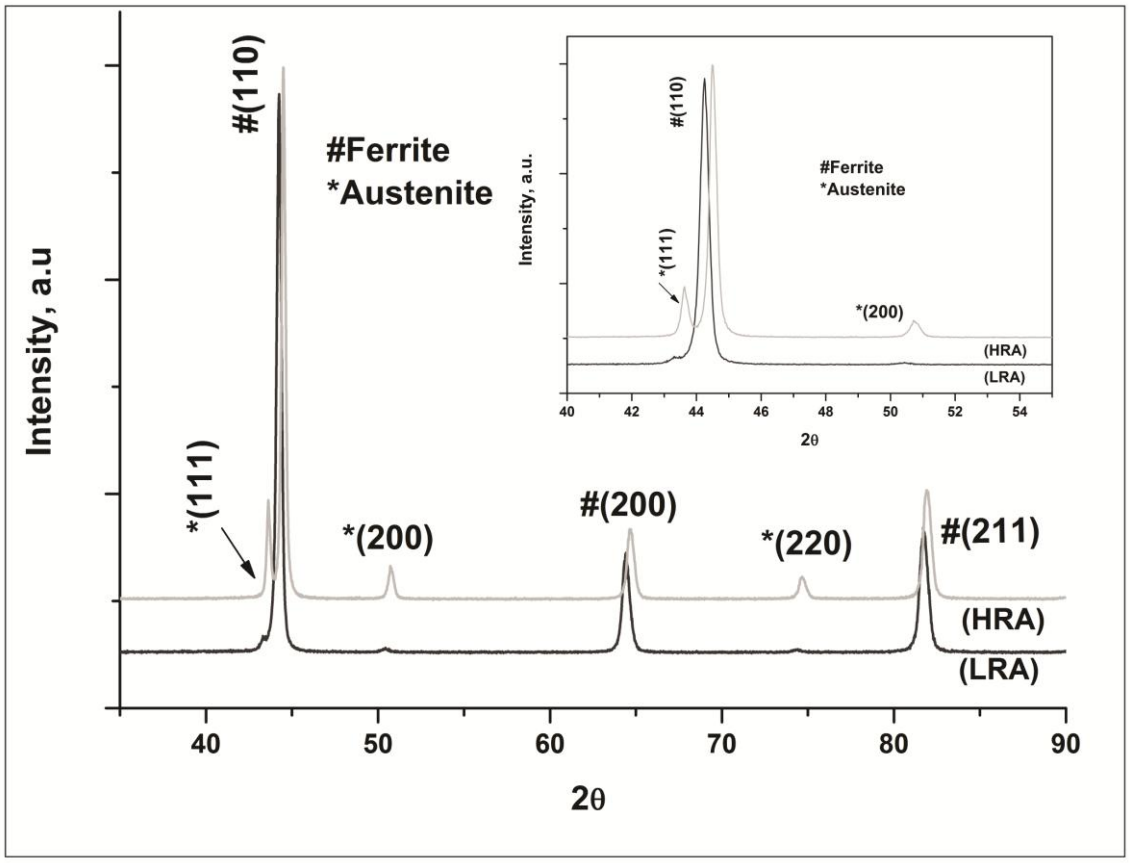


**Figure 1:** XRD results: LRA and HRA samples. Detailed of the austenite peak for both samples.

***Mössbauer Spectrometry (MS)***

According to Solomon and Levinson [10] a Mössbauer spectrum results from the resonant absorption of 14.4 keV γ-rays by the $^{57}$Fe iron nuclei. In the present case, the Mössbauer spectra for the LRA and HRA samples and for the as-quenched Chi and RA samples [7] are shown in Table 3 and Figure 2. When these nuclei are in a ferromagnetic arrangement, as in the case of the αFe below the Curie point, a six-line absorption pattern is observed. In Figure 2, it is shown such a typical six-lines pattern for the ferromagnetic αFe.

Still according Solomon and Levinson [10], if the $^{57}$Fe nucleus in the αFe is in a paramagnetic state, then a single paramagnetic resonant line will be observed. For any sample, if a paramagnetic $^{57}$Fe occurs in the sample along with the magnetically ordered

αFe phase, the corresponding spectrum will be the superposition of six-peak ferromagnetic spectrum (black lines, Figure 2) with the single-line paramagnetic spectrum (gray and dark gray lines, Figure 2).

The Mössbauer spectra for the as-quenched LRA, RA and HRA samples presented the six-line ferromagnetic (black lines) and the single-line paramagnetic patterns (dark gray lines). The ferromagnetic subspectrum represents the ferrite phase and the paramagnetic peak represents the austenite phase.

Spectrum for the Chi sample showed the six-line ferromagnetic (black lines) along with two different single-line paramagnetic patterns (gray and green lines), which can be assigned to the austenite (dark gray line), and a single-line (gray line) paramagnetic Mo-rich phase.

The δ parameter for the paramagnetic subspectrum (gray line) in the Chi-phase sample (Figure 2a) is shifted towards the negative values, i.e. $\delta = -0.30 \pm 0.04 mm.s^{-1}$. As this parameter is associated to the electronegativity of the ligands, as more it is shifted to negative values, the higher is the electronegativity of the element bound to the iron atom. This is thus an indicative that this phase is rich in Mo. Cieslak et. al. [15] tested a phase contained Fe-Mo (namely, μ-phase) and observed the more negative the δ parameter the higher the concentration of Mo, the isomeric shift in the sample tested in that work showed a IS parameter near to $-0.30 mm.s^{-1}$.

**Table 3:** Mössbauer Spectrometry results for as-quenched, chi, LRA, RA and HRA samples

| **Samples** | **Phase Identification** | **Isomeric shift δ (±0,04) mm/s** | **Phase (%)** |
|---|---|---|---|
| As-quenched | **α** | -0.01 | 99 |
| | **γ** | -0.10 | 1 |
| Chi | **α** | -0.01 | 95 |
| | **χ** | -0.30 | 3 |
| | **γ** | 0.08 | 2 |
| LRA | **α** | -0.02 | 98 |
| | **γ** | -0.10 | 2 |
| RA | **α** | -0.01 | 88 |
| | **γ** | -0.10 | 12 |
| HRA | **α** | -0.02 | 88 |

| | | | |
|---|---|---|---|
| | γ | -0.10 | 12 |

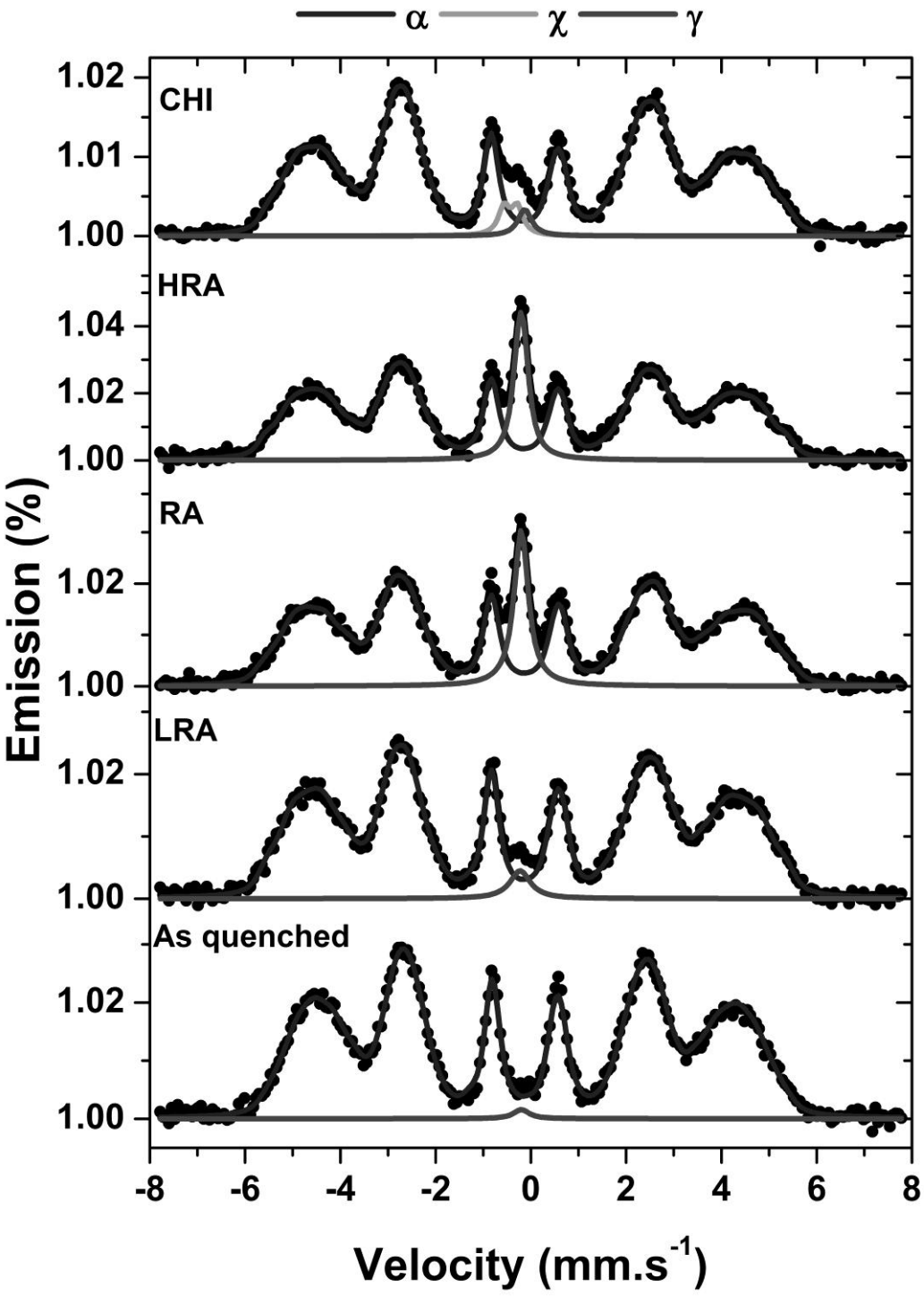


**Figure 2: a)** Mössbauer Spectrometry results of as-quenched, Chi, RA, LRA and HRA samples. **b)** Magnification of Chi sample results.

***Discussion of χ-phase identification using different techniques in the chi sample***

In order to identify and quantify the χ-phase presented in the chi-sample different techniques were used: XRD, XRD Syncronthron, Mössbauer Spectrometry, SEM and image analyzer. Since these techniques have different approaches discrepancies in the results is expected.

The XRD results did not detected the presence of χ-phase in the Chi sample, as explained in the previous work [7] this technique did not show enough sensibility to indentify this phase.

The Syncrothron results did not show the presence of χ-phase in the chi-sample, but presented traces of $Cr_{23}C_6$ in the Chi sample. As reported by Hurtado-Noreňa [16] $M_{23}C_6$ may be observed as the $Cr_{23}C_6$ compound, but for long tempering or service times changes in the composition of this phase were observed, in which several Cr positions are replaced by Fe or Mo. The Chi sample was tempering for 18h, and this change could be occurred. In addition, the Thermocalc of this alloy shows thermodynamically conditions favorable to occur carbide precipitation at temperatures below 800°C, with the maximum precipitation occurring below 680°C. However, the carbon content in this material is very low (0.01%) hindering the carbon to diffuse for the preferential areas for the formation of these precipitates.

The results of SEM showed a high amount of precipitates inside the ferrite phase and a fine phase at the grain boundaries which is rich in Cr and Mo, hence it is unlikely that all this is carbide phase. The image analyzer was used in the SEM images and the amount of χ-phase was considered 6 wt%.

The results of Mössbauer Spectrometry showed a paramagnetic phase rich in Mo and quantified this phase as 3wt% (table 3). As reported in the previous work [7], the chi-phase is rich in Mo and Cr. According to Kasper [17] the chi-phase is considered a phase with α-Mn-type with lattice parameter of 8.895Å and was indexed in the basis of a bcc cell. Kasper et al. [17] discussed the ordering of the atoms in the unit cell, and showed that this phase can be a combination of Fe-Cr-Mo with a geometrical arrangement of neighbor atoms around Mo.

The literature about characterization and quantification of chi-phase is scarce, so in the present work the phase identified by using the MS technique will be considered as the χ-phase or at least a phase rich in Mo, and the amount of this phase will be considered has been 6wt% found in the image analyzer characterized in the previous work [7].

***Discussion of retained austenite identification using different techniques***

For the identification of $\gamma_{ret}$ in the studied samples XRD and Mössbauer Spectrometry were used.

The XRD results showed that the amount of retained austenite in the Chi sample has been 7wt% [7]. The results of Mössbauer Spectrometry presented in the present work showed only 2wt% of this phase (table 3). The XRD analysis was made in two different labs and the results were 7wt% of retained austenite for both labs. Therefore, for this sample, the concentration was considered as 7wt%.

The results of XRD and Mössbauer Spectrometry techniques for the LRA sample showed the same amount (2wt%) of this phase (table 1 and 3, respectively).

The results of XRD for the RA sample showed 7wt% of $\gamma_{ret}$ [7] and the results of the Mössbauer Spectrometry showed 12wt% of this phase (table 3). The XRD analysis was performed in two different labs and the results gave 7wt% of retained austenite for both labs. Therefore, for this sample, the content of retained austenite was considered as 7wt% for the RA sample.

The results of XRD for the HRA sample identified 22wt% of retained austenite (table 1) and the results of Mössbauer Spectrometry detected 12wt% of this phase (table 3).

It is important to highlight that the heat treatment was performed to obtain 10% of retained austenite in the RA and 20% for the HRA sample. In addition, the SEM images showed a higher amount of retained austenite in the HRA sample than in the RA sample. As the results of SEM and XRD are considerable consistent, the discussion in the present work will be taking account the high amount of $\gamma_{ret}$ in the HRA sample (22%) and a medium amount of this phase in the RA sample (7%).

***SEM results***

Figure 3 presents the microstructure of the LRA and the HRA samples. The LRA (fig. 3a and 3b) and HRA samples (fig. 3c and 3d ) were heat treated above Ac1, and ferrite plus martensite with fine white lines spread over the martensite laths were observed, characterizing the retained austenite. This result is in agreement with the results reported by Gesnouin et. al. [18] which explained that austenite phase appears as precipitated platelets between the martensite laths. In the HRA sample, besides a precipitation into the ferrite, a fine phase at the grain boundary was precipitated and was

rich in Cr and Mo (black arrows fig. 3d). According to the Thermocalc calculation of this steel, in the temperature below 950°C until 500°C, the chi-phase transformation is thermodynamically favorable. It is important to highlight that although the formation of chi-phase is thermodynamically favorable, the heat treatment was performed for 1h that could not be kinetically likely to produce high amount of this phase. Tavares et. al. [19] studied a MFSS with 16.4Cr 3.62Ni2.42Mo wt.% double tempered at 670°C plus heated at 600°C for 2h and also observed a fine white phase precipitated at the grain boundaries, which was rich in Cr and Mo, but the authors could not identified the phase accurately.

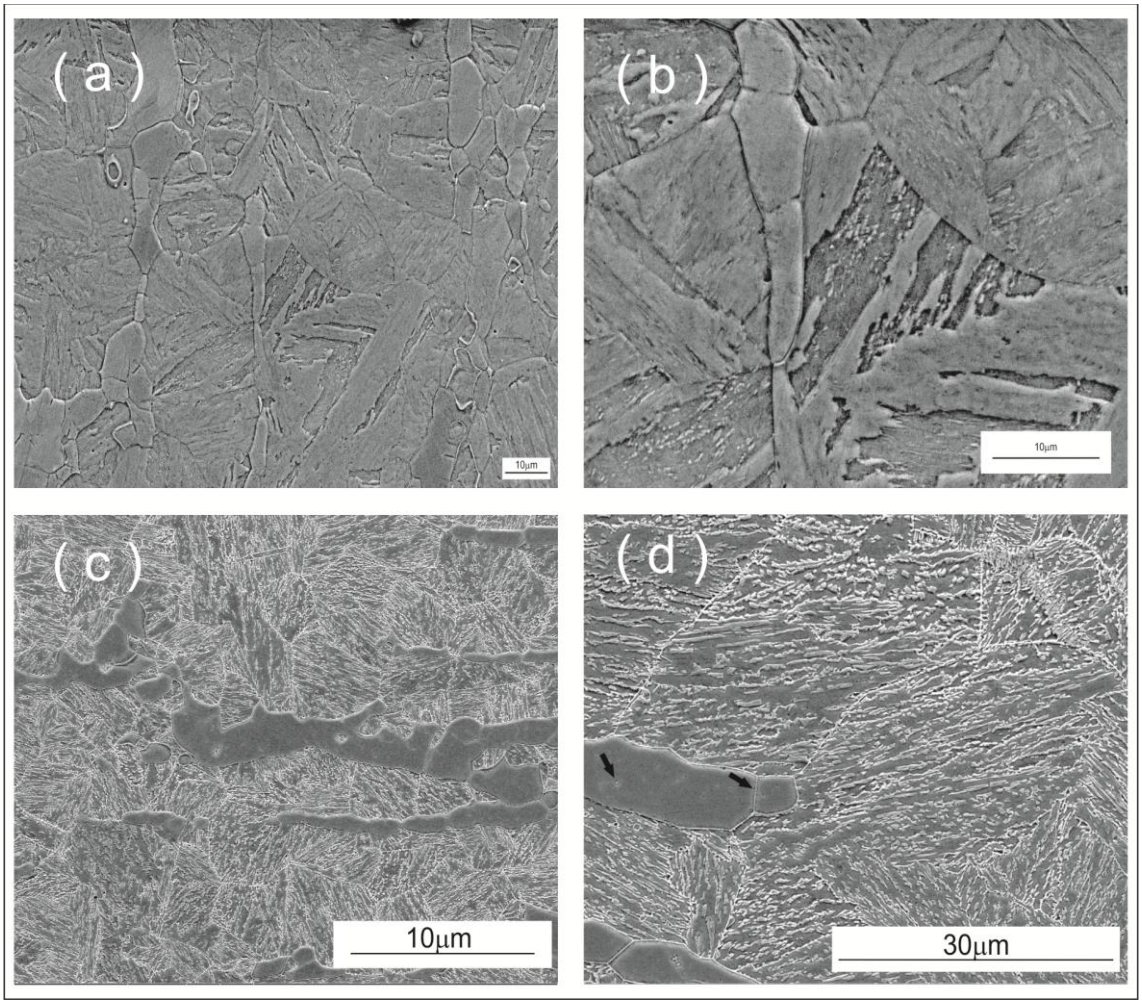


**Figura 3:** SEM (BSE-back scatered electrons) micrography results, **a)** LRA sample **b)** Magnification of a **c)** HRA sample **d)** Magnification of c.

***Retained austenite morfology***

The relative area of retained austenite was measured based on the microstructure showed in the figure 4, and the results found using the image analyzer (ImageJ) are

0.11mm$^2$ for LRA, 0.133mm$^2$ for RA and 0.288mm$^2$ for HRA. These results show that increasing the temperature of heat treatment provide an increase in the relative area of retained austenite occurs, promoting a coarse aspect of retained austenite in the sample treated at higher temperatures (HRA – 675°C) than the samples heat treated at medium and low temperatures (RA – 625°C ; LRA – 600°C). Figure 4 shows the SEM image used to measure the area of retained austenite.

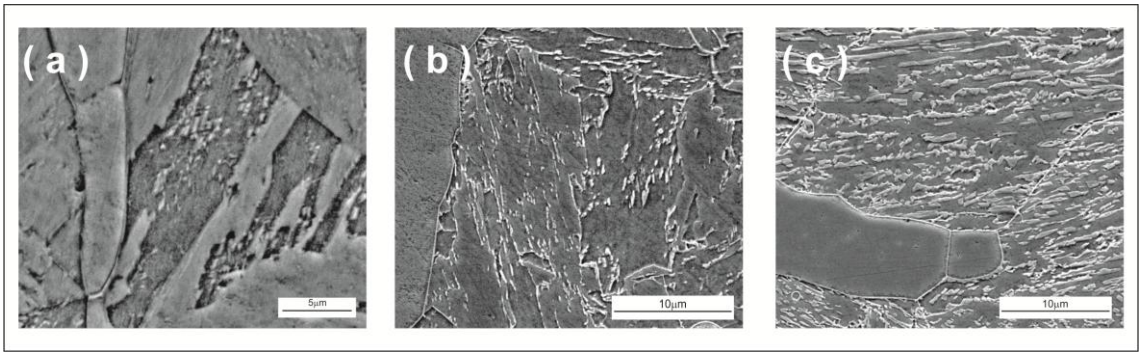


**Figure 4:** Austenite morfology **a)** LRA sample; **b)** RA sample; **c)** HRA sample.

It is important to highlight that the heterogeneous nucleation and consequently the growth of austenite from the martensite occurred from plate interfaces. Therefore, the increase in temperature will promote an increase in the phase growth. Analyzing the morphology of austenite in the three samples (fig. 4), it is possible to observe that in the LRA sample the austenite presented in a spherical form, indicating that the nucleation was favorable, but not the growth. In the RA sample, the austenite appears as needles, showing an increase in the amount of nuclei and in the phase growth. In the HRA sample, the austenite is coarser presenting a plate form, indicating an increase in the nucleation and in the phase growth.

Santos et. al. [20] studied the kinetics of the austenite transformation in the same as-quenched material studied in the present work and showed that the maximum temperature which the reversed austenite is maintained as a retained austenite in the microstructure is at 675°C (see fig. 5). The results of those work showed that above the 675°C tempering temperature, the reverse austenite transformation was increased, but the amount of austenite that remained as retained austenite in the microstructure decreased considerably, showing the instability of this transformation at high temperatures. It means that the HRA sample used in the present work has the maximum amount of retained austenite that is possible in this alloy.

In order to show the efficiency of the heat treatment performed in the LRA, RA [7] and HRA samples, the data of evolution of amount of retained austenite versus tempering temperature from Santos et. al. [20] were plotted together the same data obtained in the present work (fig.5). It is possible to observe that the results obtained in this work are in agreement with the results obtained by Santos et. al. [20].

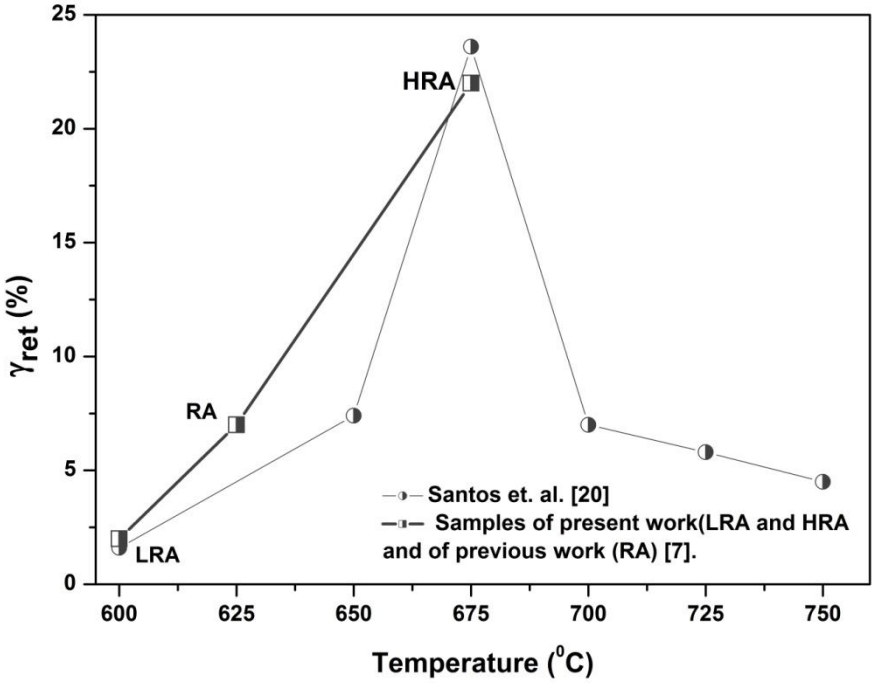


**Figure 5:** Transformed austenite fraction versus tempering temperature. Adapted from Santos et. al. [20] versus the data from present work.

***Hydrogen permeation***

The experimental versus theoretical data of hydrogen permeation results of the LRA and HRA samples are shown in table 4 and figure 6. Theoretical curves fitted the experimental data quite well, with a slightly difference due to the presence of traps in the microstructure, which the model does not consider.

For the LRA and HRA samples the $D_{app}$ for the experimental and theoretical model was considered the same, due to the time to start the detection of hydrogen was well fitted. A delay in the hydrogen detection for experimental data was observed, promoting a time interval, $\Delta t$, between the theoretical versus experimental data. The reason for this phenomenon was explained in the previous work [7] and can be used in this work, i.e.

the experimental curve presented a delay which can be attributed to the completion of the deep trap sites before the detection of hydrogen in the anodic side. During this time, no hydrogen permeates through the sample. After this filling, hydrogen permeation occurred across the samples and the curve presented a good adjustment with the theoretical curve [7].

Both samples tested in the present work have retained austenite, which acts as deep trap for hydrogen generating a delayed detection of hydrogen, which is not considered in the theoretical model. Due to the good fitting for both samples, the discussion will be done considering the theoretical data.

The diffusivity of LRA sample was higher than that found for the HRA sample [7] ($1.2x10^{-12}$ versus $3.4x10^{-13}$ $m^2.s^{-1}$ respectively). It is already expected since the HRA sample presents martensite, austenite, retained austenite, fine precipitates and a phase richest in Cr and Mo at grain boundaries , which promote many interfaces for hydrogen permeate (M/δ; M/γ) and additional trapping sites for hydrogen thereby reducing hydrogen permeability and diffusivity in this complex microstructure. Furthermore, the austenite phase trapped the H-atoms and it takes extremely long time to diffuse out of the γ-interface, due to the high activation energy of this phase ($55KJ.mol^{-1}$) [21]. Gesnouin et. al. [18] studied a 13CrNiMo steel with different amounts of retained austenite and also observed a decrease in the hydrogen diffusivity with an increase in the amount of retained austenite. Kim et. al [22], in their study of a TRIP steel with 13% of retained austenite, also observed this decrease in the hydrogen diffusivity for the sample with a high content of retained austenite.

**Table 4:** Data of hydrogen permeation of LRA and HRA samples. Area (A), diffusion coefficient ($D_{app}$) and solubility (S) in martensitic/ferritic stainless steel.

| Sample | A($m^2$) | $S_{app}$ ($mol.H.m^{-3}$) | $D_{app}$($m^2.s^{-1}$) | Reference |
|---|---|---|---|---|
| **as-quenched** | 0.0291 | 105 | $3.0x10^{-12}$ | [7] |
| **Chi** | 0.2761 | 904 | $2.1x10^{-12}$ | [7] |
| **LRA** | 0.0137 | 64 | $1.2x10^{-12}$ | Present work |
| **RA** | 0.3312 | 1577 | $7.8x10^{-13}$ | [7] |
| **HRA** | 0.0797 | 331 | $3.4x10^{-13}$ | Present Work |

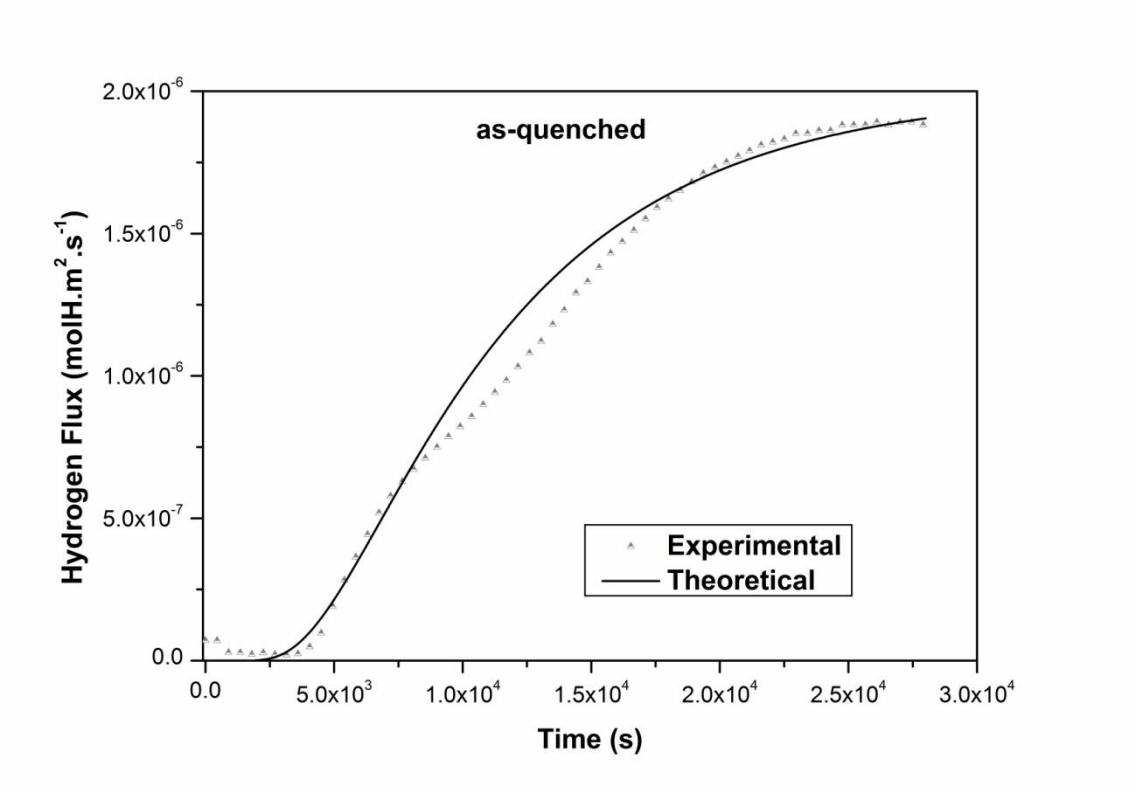
as-quenched
Hydrogen Flux (molH.m$^{-2}$.s$^{-1}$)
Time (s)
Experimental
Theoretical
2.0x10$^{-6}$
1.5x10$^{-6}$
1.0x10$^{-6}$
5.0x10$^{-7}$
0.0
0.0
5.0x10$^{3}$
1.0x10$^{4}$
1.5x10$^{4}$
2.0x10$^{4}$
2.5x10$^{4}$
3.0x10$^{4}$

**(a)**

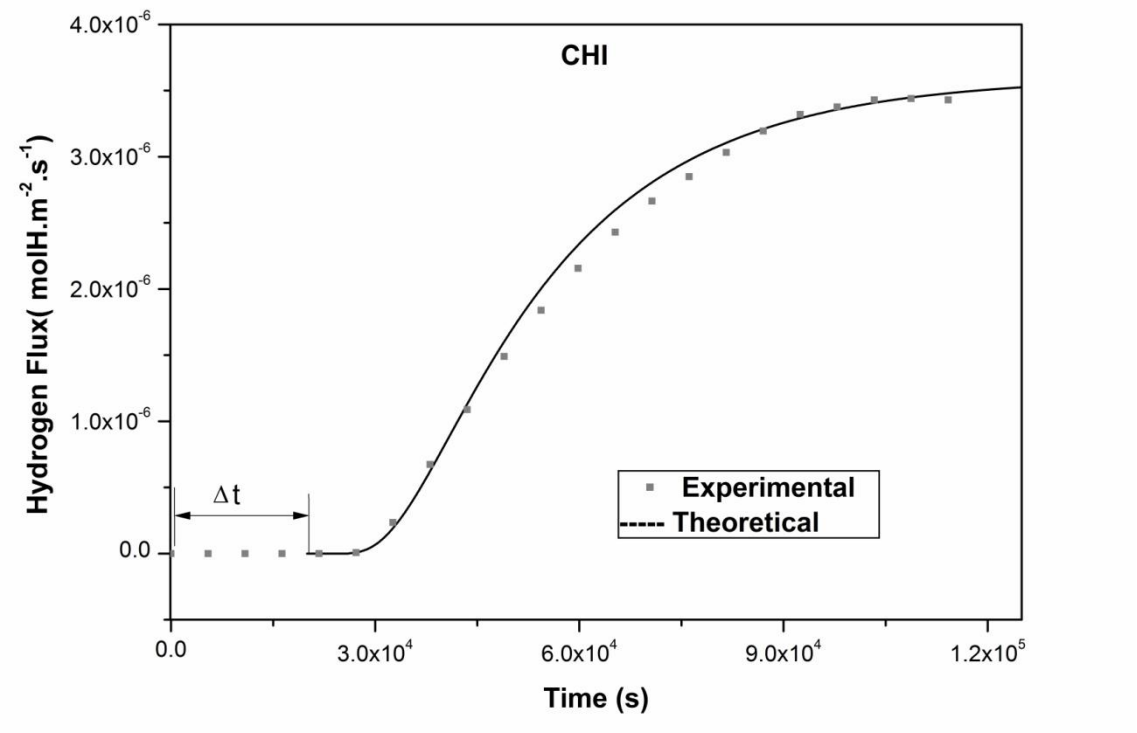
CHI
Hydrogen Flux( molH.m$^{-2}$.s$^{-1}$)
Time (s)
Δt
Experimental
Theoretical
4.0x10$^{-6}$
3.0x10$^{-6}$
2.0x10$^{-6}$
1.0x10$^{-6}$
0.0
0.0
3.0x10$^{4}$
6.0x10$^{4}$
9.0x10$^{4}$
1.2x10$^{5}$

**(b)**

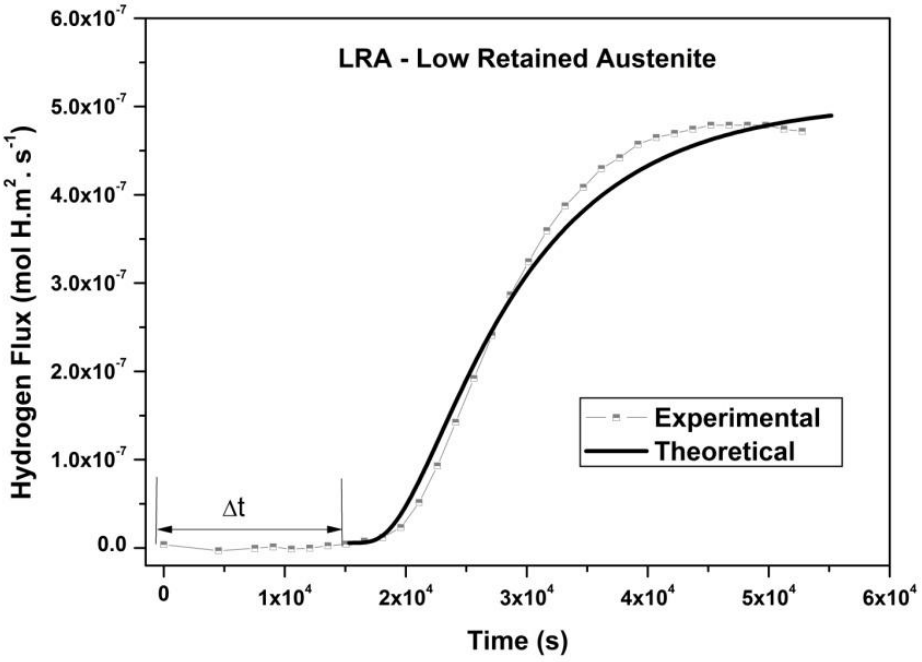
LRA - Low Retained Austenite
Hydrogen Flux (mol H.m$^2$ . s$^{-1}$)
Time (s)
Experimental
Theoretical
Δt
6.0x10$^{-7}$
5.0x10$^{-7}$
4.0x10$^{-7}$
3.0x10$^{-7}$
2.0x10$^{-7}$
1.0x10$^{-7}$
0.0
0
1x10$^4$
2x10$^4$
3x10$^4$
4x10$^4$
5x10$^4$
6x10$^4$

**(c)**

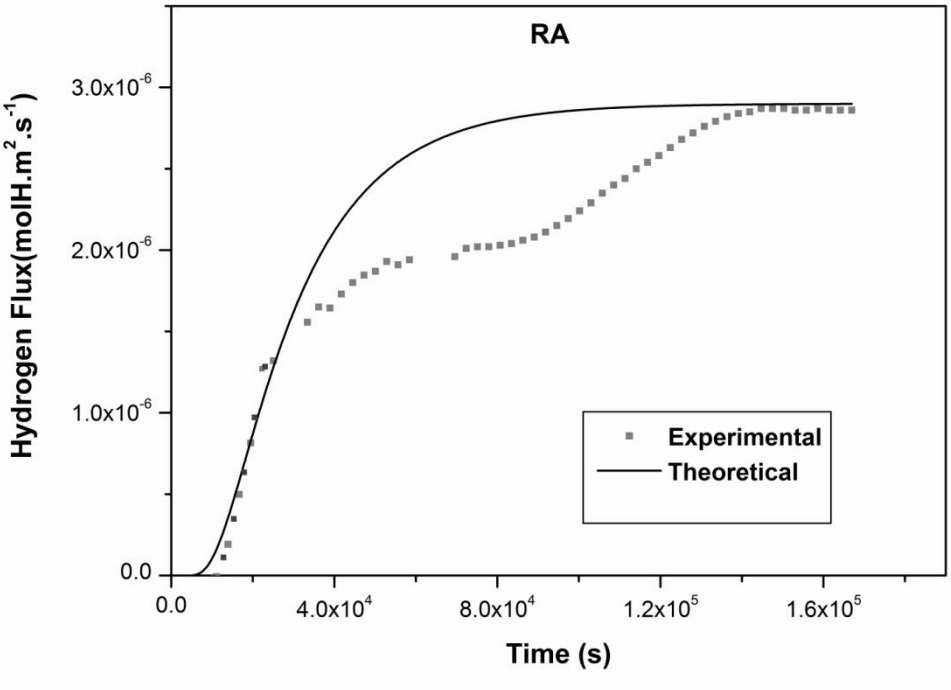
RA
Hydrogen Flux(molH.m$^2$.s$^{-1}$)
Time (s)
Experimental
Theoretical
3.0x10$^{-6}$
2.0x10$^{-6}$
1.0x10$^{-6}$
0.0
0.0
4.0x10$^4$
8.0x10$^4$
1.2x10$^5$
1.6x10$^5$

**(d)**

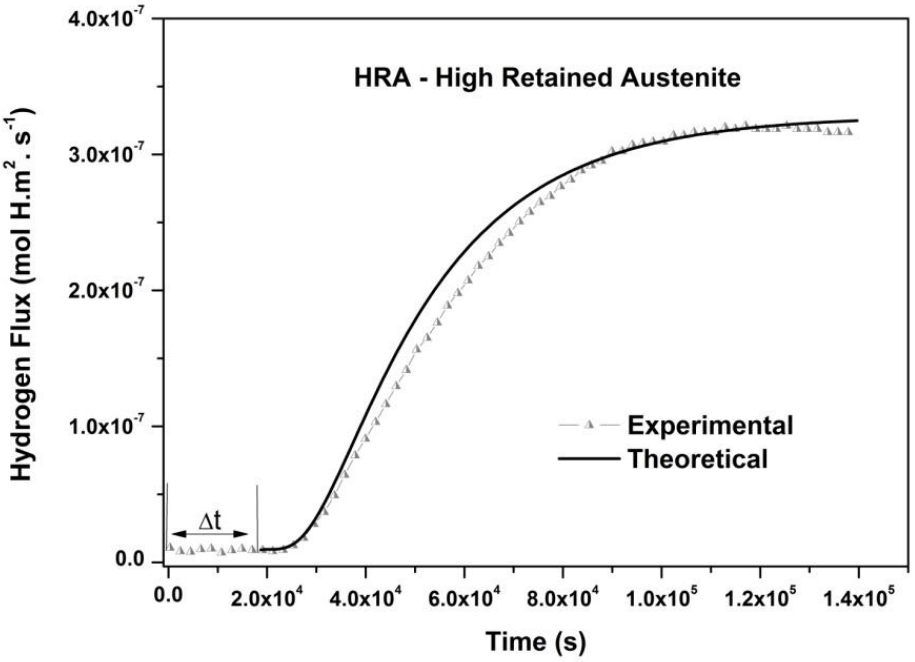


**(e)**

**Figure 6:** Electrochemical hydrogen permeation curves for: **a)** as-quenched sample [7]; **b)** Chi sample [7]; **c)** Low retained austenite sample (LRA) [present work]; **d)** Medium retained austenite (RA) [7]; **e)** High retained austenite sample (HRA) [present work].

In order to verify the relationship of the hydrogen diffusion coefficient with the amount of retained austenite, the figure 7 shows the results of $D_{app}$ for the two samples studied in the present work (LRA and HRA) and the results studied in the previous works (as-quenched, RA and Chi) [7]. It is possible to observe a tendency to $D_{app}$ decrease with the increasing of the content of $\gamma_{ret}$. The sample with no retained austenite (as-quenched) showed the highest diffusion coefficient ($D_{app}$ = 3.9x10$^{-12}$ m$^2$.s$^{-1}$), and the sample with 22% of retained austenite presented the lowest diffusion coefficient ($D_{app}$.= 3.4x10$^{-13}$m$^2$.s$^{-1}$), with one order of magnitude lower.

The $D_{app}$ for the LRA and RA samples presented just a slight difference (1.2x10$^{-12}$ versus 9.0x10$^{-13}$ m$^2$.s$^{-1}$ respectively), whereas the difference between RA (9.0x10$^{-13}$m$^2$.s$^{-1}$) and the HRA sample (3.4x10$^{-13}$m$^2$.s$^{-1}$) was higher. These differences can be attributed for a higher amount of retained austenite in the HRA sample. It is important to take account that the hydrogen diffusivity in austenite itself is 10$^{-15}$/10$^{-16}$ m$^2$·s$^{-1}$[23], and the diffusivity obtained in this work is three magnitude orderhigher, which can be conclude that the hydrogen diffused mainly in the ferrite, martensite and in the M/$\gamma_{ret}$ interface, instead in the austenite itself. Kimura et. al.[24] studied a supermartensitic stainless

steel (S13Cr) with different contents of retained austenite (0 to 37%) and did not observe significant difference among the $D_{app}$ for all the samples. They concluded that there was no dependency of hydrogen diffusion coefficient on the amount of austenite, and the hydrogen diffused in the martensite phase instead in the austenite.

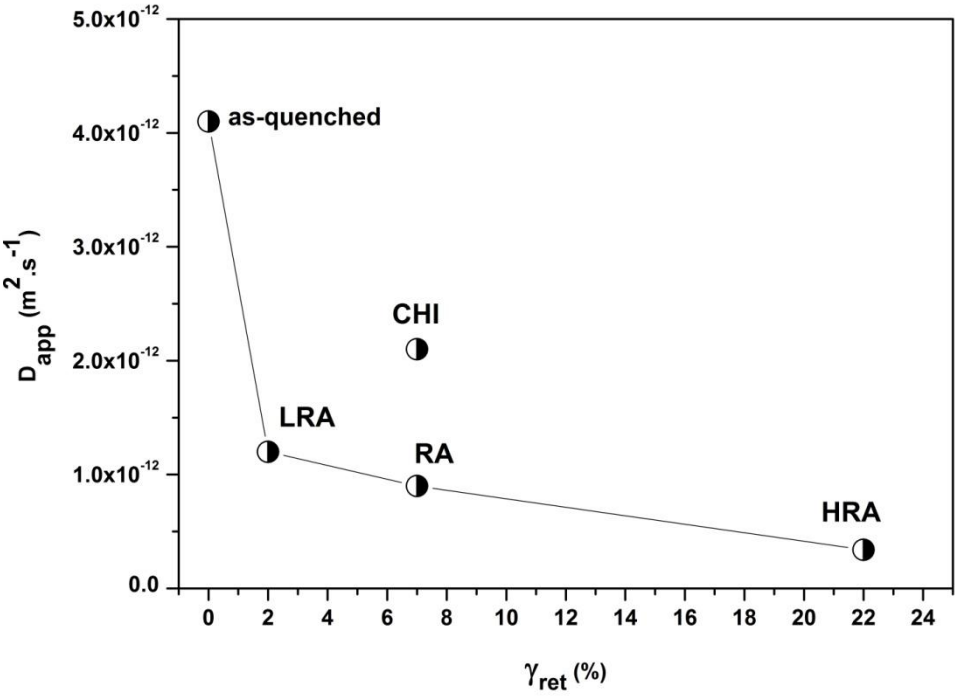


**Figure 7:** $\%\gamma_{ret}$ versus $D_{app}$ for the LRA and HRA studied in the present work, and for the as-quenched, RA and Chi studied in the previous work [7].

In order to consider the presence of deep traps in these samples, the solubility ($S_{app}$) was calculated using the equation 2 and added the solubility obtained by Fick's law using the $\Delta t$ observed in the figure 6. The results of hydrogen solubility ($S_{app}$) for LRA and HRA samples are presented in table 4. The hydrogen solubility for the HRA sample was higher than for the LRA sample. It was expected due to the presence of austenite phase. Moreover, the HRA sample was doubled tempered, decreasing the amount of defects in the microstructure and increasing the solubility of hydrogen.

In order to evaluate the solubility of hydrogen with the amount of retained austenite, the results obtained in a previous work [7] were compared with the data obtained in the present work. These results are shown in figure 8.

The RA sample presented the highest hydrogen solubility and the LRA sample presented the lowest (1577 and 331 $mol.H.m^{-3}$, respectively). As the retained austenite

presents a trend to absorb a high amount of hydrogen, suggesting an increase in the solubility of hydrogen in the sample with the increase in the amount of retained austenite, the sample could present the highest hydrogen solubility. On the contrary, the sample with a medium content of retained austenite (RA sample) showed the highest solubility. An explanation for this is that the finely dispersed austenite phase increases the solubility [4,5] of hydrogen, and coarse particles act as a obstacle for hydrogen, promoting a decrease in the solubility [25]. As the austenite in the RA sample are finer and more dispersed in the matrix than the austenite in the HRA sample, the solubility of hydrogen increased in the RA sample.

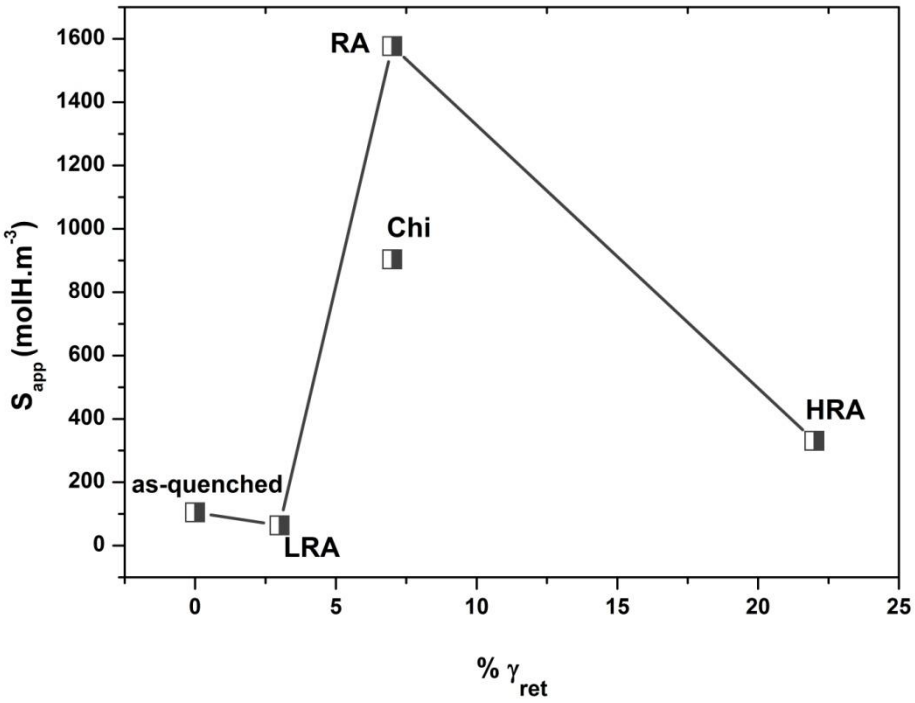


**Figure 8:** $\%\gamma_{ret}$ versus $S_{app}$ for LRA and HRA present work, and as-quenched, RA and Chi previous work [7].

## Conclusions

The influence of retained austenite in the hydrogen permeation has been studied using the electrochemical hydrogen permeation technique.

The Mossbauer Spectrometry showed a phase rich in Mo, which was associated to the χ-phase, or at least to a phase rich in Mo.

For identification of retained austenite, the XRD, XRD Syncronthron and Mossbauer Spectrometry techniques were used and compared. The results of the XRD technique

were considered more accurate and the discussion was made based on the results from this technique.

The morphology of retained austenite is influenced by the tempering temperature, presenting a spherical form at low tempering temperature (600°C) a needle form at medium tempering temperature (625°C) and a plate form at high tempering temperature (675°C).

The lowest $D_{app}$ was obtained for the HRA sample, and the highest solubility was obtained for the RA sample, showing the influence of retained austenite morphology in the hydrogen permeation.

**Acknowledgments**

The authors would like to sincerely thank Vallourec Tubos do Brasil, CNPq and CAPES for their financial support.

## References

[1] Kondo K., Amaya H., Ohmura T., Moriguchi K. Effect of cold work on retained austenite and on corrosion performance in low carbon. NACE Corrosion 2003, paper 03094.

[2] Kimura M., Miyata Y. Toyooka T. Effect of retained austenite on corrosion performance for modified 13%Cr steel pipe. NACE Corrosion 2000, paper 00137.

[3] Park J.Y., Park Y. S. The effects of heat-treatment parameters on corrosion resistance and phase transformations of 14Cr-3Mo martensitic stainless steel. Materials Science and Engineering A 2007 449-451: 1131-34.

[4] Solheim KG, Solberg JK, Walmsley J, Rosenqvist F, Bjørnå TH. Hydrogen Induced stress cracking in supermartensitic stainless steels – Stress threshold for coarse grained HAZ. Engineering Failure Analysis 2013; 34:140.

[5] Sojka J. Vodárek V., Schindler I., Lyb C., Jérôme M., Vánová P., Ruscassier N., Wenglorzová A. Effect of hydrogen on the properties and fracture characteristics of TRIP 800 steels. Corrosion Science 2011, 53: 2575–81.

[6] Szost BA, Vegter RH, Rivera-Díaz-del-Castillo PEJ. Hydrogen trapping mechanisms in nanostructured steel. Metallurgical and Materials Transactions 2013; 44A: 4542-50.

[7] Garcia D.C.S., Carvalho R.N., Lins V.F.C., Rezende D.M., Santos D.S. Influence of microstructure in the hydrogen permeation in martensitic-ferritic stainless steel. International Journal of Hydrogen Energy 2015, http://dx.doi.org/10.1016/j.ijhydene.2015.06.102

[8] Brand R. A., Improving the validity of hyperfine field distributions from magnetic alloys: Part I: Unpolarized source. Nuclear Instruments and Methods in Physics Research Section B 1987, 28: 398-14.

[9] Lemoine C., Fnidiki A. Danoix F., Hédin M. Teillet J. Mössbauer and atom probe studies on the ferrite decomposition in duplex stainless steels caused by the quenching rate. J. Phys. 1999, Condens. Matter. 11 1105. http://iopscience.iop.org/0953-8984/11/4/018.

[10] Solomon H. D., Levinson L. M. Mössbauer effect study of 475°C embrittlement of duplex and ferritic stainless steel. Acta Metallurgica 1978, 26: 429-42.

[11] ISO 17081:2004(E), Method of Measurement of Hydrogen permeation and Determination of Hydrogen Uptake and Transport in Metals by an Electrochemical Technique, ISO, Switzerland, 2004.

[12] Santos DS, Miranda PEV. Hydrogen solubility in amorphous and crystalline materials. International journal of hydrogen energy 1998; 23: 1011-17.

[13] Boes N, Zuchner H. Eletrochemical methods for studying diffusion permeation and solubility of hydrogen in metals. Journal of the Less-Common Metals 1976; 49: 223-40.

[14] Kircheim R. Hydrogen solubility and diffusivity in defective and amorphous metals. Progress in Materials Science1988; 32: 261-25.

[15] Cieslak J., Przewoznik J., Dubiel S.M. Structural and electronic properties of the μ-phase Fe-Mo compounds. Journal of Alloys and Compounds 2014, 612: 465-70

[16] Hurtado-Noreňa C., Dano C. A., N, Luppo M.I., Bruzzoni P. Evolution of Minor Phases in a 9PctCr Steel: Effect of Tempering Temperature and Relation with Hydrogen

[17] Kasper J. S. The ordering of atoms in the chi-phase of the iron chromium molybdenum system. Acta Metallurgica 1954, 2: 456-61.

[18] Gesnouin C., Hazarabedian A., Bruzzoni P.,Ovejero-García J., Bilmes P., Llorente C. Effect of post-weld heat treatment on the microstructure and hydrogen permeation of 13CrNiMo steels. Corrosion Science 2004, 46: 1633–47.

[19] Tavares S.S.M. , Bastos I. N., Pardal J.M., Montenegro T.R., Silva M.R. Slow strain rate tensile test results of new multiphase 17%Cr stainless steel under hydrogen

cathodic charging. International Journal of Hydrogen Energy 2015, http://dx.doi.org/10.1016/ j.ijhydene.2015.05.148.

[20] Santos T.A.A., Carvalho R. N., Rocha A. C., Ferreira M.A.C., Buono V.T.L. Estudo da Reversão da Austenita em um aço inoxidável martensítico-ferrítico. 69º Congresso Anual da ABM – Internacional, 14º ENEMET - Encontro Nacional de Estudantes de Engenharia Metalúrgica, de Materiais e de Minas, 21 a 25 de julho de 2014, São Paulo, SP, Brasil.

[21] Park B.Y.D., Maroef I.S., Landau A., Olson D.L. Retained Austenite as a Hydrogen Trap in Steel Welds Hydrogen trapping is investigated as a means of improving resistance to hydrogen-assisted cracking in HSLA steels. WELDING JOURNAL 27S-35S.

[22] Kim. S.J., Yun. D.W., Suh D.W., Kim K.Y. Electrochemical hydrogen permeation measurement through TRIP steel under loading condition of phase transition. Electrochemistry Communications 2012, 24: 112–15.

[23] Olden V, Thaulow C, Johnsen R. Modelling of hydrogen diffusion and hydrogen induced cracking in supermartensitic and duplex stainless steels. Materials and Design 2008, 29: 1934-48.

[24] Kimura M., Miyata Y., Toyooka T. Effect of retained austenite on corrosion performance for modified 13%Cr steel pipe. Corrosion NACE 2000, n° 00137.

[25] Pressouyre GM. Hydrogen traps, repellers, and obstacles in steel; consequences on hydrogen diffusion, solubility, and embrittlement. Metallurgical Transactions A 1983;14A: 2189-93.

# *CHAPTER 4*

## *PAPER 3: Influence of Retained austenite and chi-phase in the Hydrogen Embrittlement in Martensitic-Ferritic Stainless Steel*

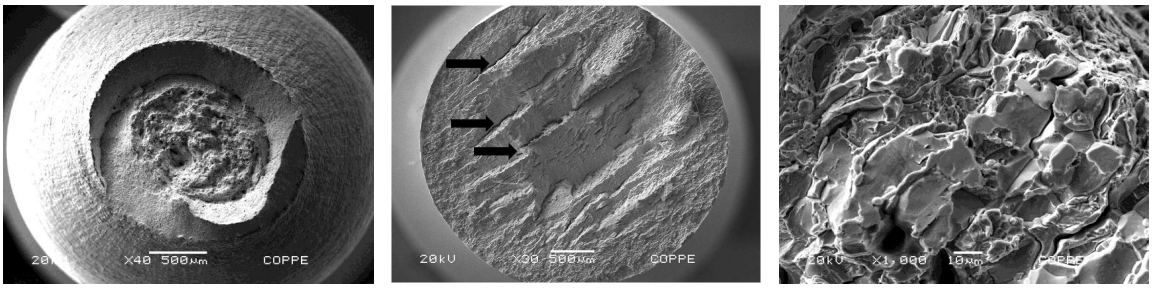

## Abstract

The influence of the retained austenite and chi-phase of martensitic-ferritic steel on hydrogen embrittlement was investigated by performing tensile tests in samples uncharged and cathodically charged using two different crosshead displacement speeds, and the results were compared based on different approaches, i.e. loss ductility versus index embrittlement. The samples tested with hydrogen showed a brittle failure with low elongation and low reduction of area. The hydrogen embrittlement increased with the increase of retained austenite content, and this phase seems to play a role on the hydrogen embrittlement.


## Introduction

Understanding of hydrogen interactions and transport in dual-phase microstructures is necessary to control hydrogen embrittlement (HE). This phenomenon has a substantial influence on the mechanical properties, causing a brittle and unpredictable fracture promoting severe consequences on the integrity of the material [1]. The intensity of HE depends on many factors: source of hydrogen, microstructure, heterogeneity and distribution of hydrogen concentration, strength or strain level and trap binding energy. The trap binding energy has a direct impact on the HE. In the class of low binding energy the dislocations can influence on the mechanical behavior of the metal and trap hydrogen reversibly. The interaction of hydrogen with dislocations was considered an important factor in understanding hydrogen embrittlement [2]. This kind of trap sites with low binding energy values provide a reservoir of diffusible hydrogen that can diffuse to sites susceptible to hydrogen-induced cracking [3].

The retained austenite belongs to the class of high binding energy, although this phase act as irreversible hydrogen trap with a high binding energy of $55 kJ.mol^{-1}$ [4], and is considerable to be irreversible trap for hydrogen, the retained austenite can also be responsible for the embrittlement on the material. As reported by Solheim et. al. [5] retained austenite plays an important role to prevent or to increase the HE susceptibility. According to these authors [5] the finely dispersed austenite phase mainly increases the solubility and decreases the diffusion rate of hydrogen when compared with ferrite and martensite phases. Therefore, the difference between the solubility and diffusivity at

low temperature in ferrite and martensite will be the trigger for the austenite to act as a hydrogen trap in this microstructure. In their study in SMSS with different amounts of retained austenite, Solheim et. al. [5] concluded that the higher the amount of retained austenite the higher the HE.

In terms of mechanical properties, the tensile tests, charged and uncharged with hydrogen, are used to predict the HE susceptibility of the material. Since the hydrogen embrittlement is responsible to promote loss in plasticity on the material, many investigations have been developed using tensile tests with samples charged and uncharged with hydrogen [6- 10]. The embrittlement index (EI) and/or loss ductility (LD) are parameters used to evaluate materials using this testing.

The EI provide information on the loss of ductility based on the results of elongation of the sample with and without hydrogen. The parameter range varies between 0 to 1; results close to 0 means a small ductility drop and the material seems to be unaffected by hydrogen, and results close to 1 means that the ductility drop is higher and the material exhibited the maximal HE [1, 8,11].

The LD parameter is calculated based on the results of reduction of area in the sample tested with and without hydrogen. Ordinarily this parameter has the same interpretation of EI, but the calculation procedure is different.

Tensile tests with and without a hydrogen charge can provide important information on the mechanism of the failure and the behavior of the material in front of hydrogen. In the present work the influence of the retained austenite and chi-phase of martensitic-ferritic steel on hydrogen embrittlement was investigated by performing tensile tests in samples uncharged and cathodically charged using two different crosshead displacement speeds, and the results were compared based on different approaches.

## Experimental Details

The steel used in this research was a MFSS which the chemical composition is shown in table 1. The samples were extracted from water quenched seamless stainless steel tube after a solution treatment at 1000°C for 30 min. The five microstructures used in this work were obtained with a specific heat treatment, as detailed in a previous work [12, 13]. The samples for tensile tests were of specific shape with 35.0mm gauge length ($l_0$) and 4.0mm diameter ($d_0$). The samples were placed in an especially electrochemical

cell, which just the gauge length was in contact with the solution. For the test, performed in a strain rate of 1.0mm.min$^{-1}$ , the samples were pre-charged for 168 h using a 3.5 wt./v % NaCl solution with a pH 4.0 adjusted by $CH_3COOH$ using a cathodic current of -20mA and the tensile test was performed without hydrogen. For the test performed in the slow strain rate tensile (SSRT) the samples were pre-charged for 2h before the test began using the same current and solution used in the test performed for 168h charged sample. After the pre-charging, the test started with a speed of 0.01mm.min$^{-1}$ and the hydrogen charge was maintained until the end of the test. After both tensile tests, the fracture surface was investigated using a scanning electron microscope (SEM), JEOL JSM 6460.

The embrittlement index parameter (EI), which measure the hydrogen embrittlement in the sample with and without hydrogen charging was calculated by equation 1.

$$EI = \frac{El_1 - El_2}{El_1} \qquad \text{equation (1)}$$

Where EI is the embrittlement index; $El_1$ is the elongation of the sample tested without hydrogen charging and $El_2$ is the elongation of the sample tested with hydrogen charging.

The loss ductility (LD) is another parameter that provide the information of hydrogen embrittlement was compared with EI and was calculated by equation 2.

$$LD = \frac{AR_1 - AR_2}{AR_1} \qquad \text{equation (2)}$$

Where $AR_1$ is the area reduction of the sample tested without hydrogen charging and $AR_2$ is the area reduction of the sample tested with hydrogen charging.

**Table 1 –** The chemical composition of investigated MFSS (wt%)

| C | Cr | Ni | Mo | Si | S | P |
|---|---|---|---|---|---|---|
| 0.012 | 14.00 | 5.00 | 3.00 | 0.32 | 0.002 | 0.014 |

## Results and Discussion

### *Tensile Tests*

***As-quenched sample***

The tensile test results for as-quenched samples with and without hydrogen charging are summarized in figure 1 and table 2. The yield strength (YS) and the ultimate tensile strength (UTS) have a trend to increase with hydrogen charging tests. The sample tested at 168h charged sample cathodically charged with hydrogen presented higher YS and UTS than the sample tested at SSRT condition. The elongation and reduction of area decrease for samples hydrogen charged and the EI is higher for the 168h charged sample charged sample. The steel sample tested without H charging presented 92% higher elongation than the 168 h charged sample, and showed 80% higher elongation when comparing of SSRT test.

It is important to highlight that the as-quenched sample had ferrite and quenched martensite, and consequently a higher amount of dislocations and defects, thus providing more preferred sites for trapping hydrogen reversibly [14].

On the previous work [12], as-quenched samples showed a high hydrogen diffusion coefficient ($D_{app}$ = $3.9x10^{-12}$ $m^2.s^{-1}$) and consequently a high amount of diffusible hydrogen, with a de-trapping hydrogen temperature by TDS test of 109°C. These results are well aligned with the results found in this work, which due to the high capacity of trap the hydrogen reversibly the more embrittlement will be promoted on the material. This argument is supported by the high loss of ductility suffered for both samples tested in different hydrogen charging conditions. Depover et. al. [1] studied different kinds of steel (Dual-Phase, TRIP, HSLA and Ferritic-Bainitic) and demonstrated that the lower hydrogen peak temperature desorption, the higher the amount of diffusible hydrogen, consequently the greater hydrogen embrittlement.

Other important point to discuss is that even though the tests were performed in different conditions of charge and deformation rate, the difference among the results was not sufficient to detect a large difference on the mechanical properties. The results of SSRT test showed lower hydrogen embrittlement than the 168h charged sample test. This result was found although the displacement speed in the SSRT test was lower, and some studies found that the lower the displacement speed the higher the HE [1]. It is important to consider that in the SSRT test, the pre-charging of hydrogen was only for 2 h and the test occurred during 3 h, i.e. the distance that hydrogen could diffuse during the pre-charging time was 0.34 mm for the SSRT test, and 3.1mm for the 168h charged sample charged sample.

The sample charged for 168h charged sample allowed a saturation of hydrogen in the microstructure before the beginning of the tensile test, which cause the shielding effect on the dislocations promoting a local hardening and consequentially ductility loss.

The SSRT sample was only charged on its surface and during the test the continued inflow of hydrogen simultaneously with deformation promoted an increased mobility of the dislocations and the H transport was performed through such existent flaws as well as with the ones created during the test. The result of it is a substantial loss of ductility, triggered by the dislocations charged with H.

Birnbaum [15] observed that under conditions of constant stress the hydrogen reduces the barriers of dislocation and increases the slip planarity of dislocations. Deformation with simultaneous electrochemical charging of H have been reported to cause both softening and hardening of steel. At high strain rates, where the H atmospheres move with but lag behind the dislocations, decreases in dislocation mobility and macroscopic hardening may be expected as the atmospheres provide a drag force.

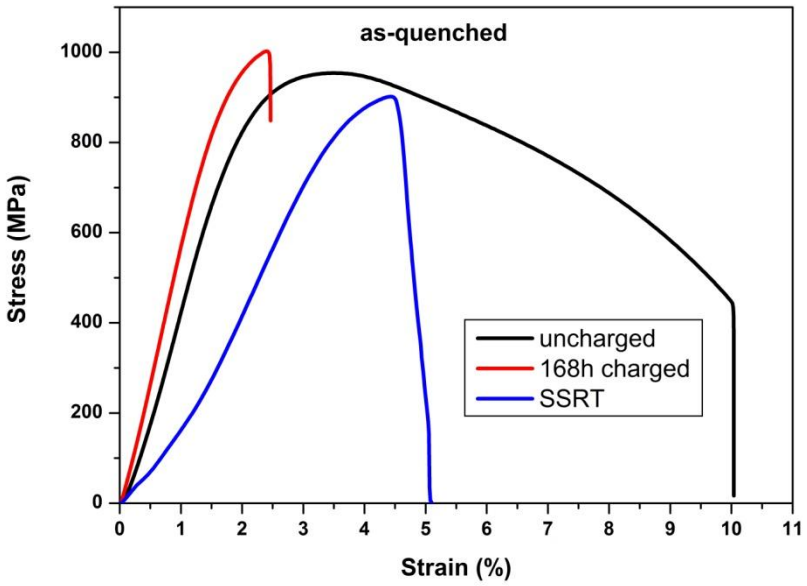


**Figure 1:** Tensile tests results for the as-quenched sample uncharged, 168h charged sample with H and SSRT condition.

**Table 2:** Summary the tensile tests performed on the as-quenched sample with and without H charging. min.

| Sample | YS (MPa) | UTS (MPa) | Elongation (%) | Reduction of Area (%) | Index Embrittlement |
|---|---|---|---|---|---|
| Without H | 835 | 958 | 8.9 | 78.2 | - |
| 168h charged sample | 901 | 991 | 0.7 | 4.8 | 0.9 |
| SSRT | 857 | 907 | 1.8 | 14.4 | 0.8 |

The SEM images for these samples are shown in figure 2. The sample without H charge (figure 2a and 2b) presented 100% of ductile fracture with dimples indicating microvoid coalescence (MVC). Fracture surface of sample tested after 168h charged sample of hydrogen charging, (figure 2c and 2d), revealed that hydrogen embrittlement manifested itself by a change in the failure micromechanism from ductile for brittle failure (predominant cleavage and transgranular) with small dimples (see black arrows fig. 2d) and ductile hair lines (see red arrows fig. 2d). The ductile hair lines are characteristic of hydrogen embrittlement and are formed by being drawn out as fine ridges during separation and thus represent small areas of plastic deformation indicating localized plasticity.

The fracture surface for the as-quenched sample after the SSRT testing is shown in figure 2e and 2f. As can be seen, the surface of this sample was more heterogeneous than the 168h charged sample charged sample, but also presenting predominant brittle transgranular characteristics with localized plasticity. Many authors [1, 16-18] studied different kinds of steels, different charge conditions and also found the change in the micro mechanism fracture from ductile to brittle form of samples uncharged and charged, respectively.

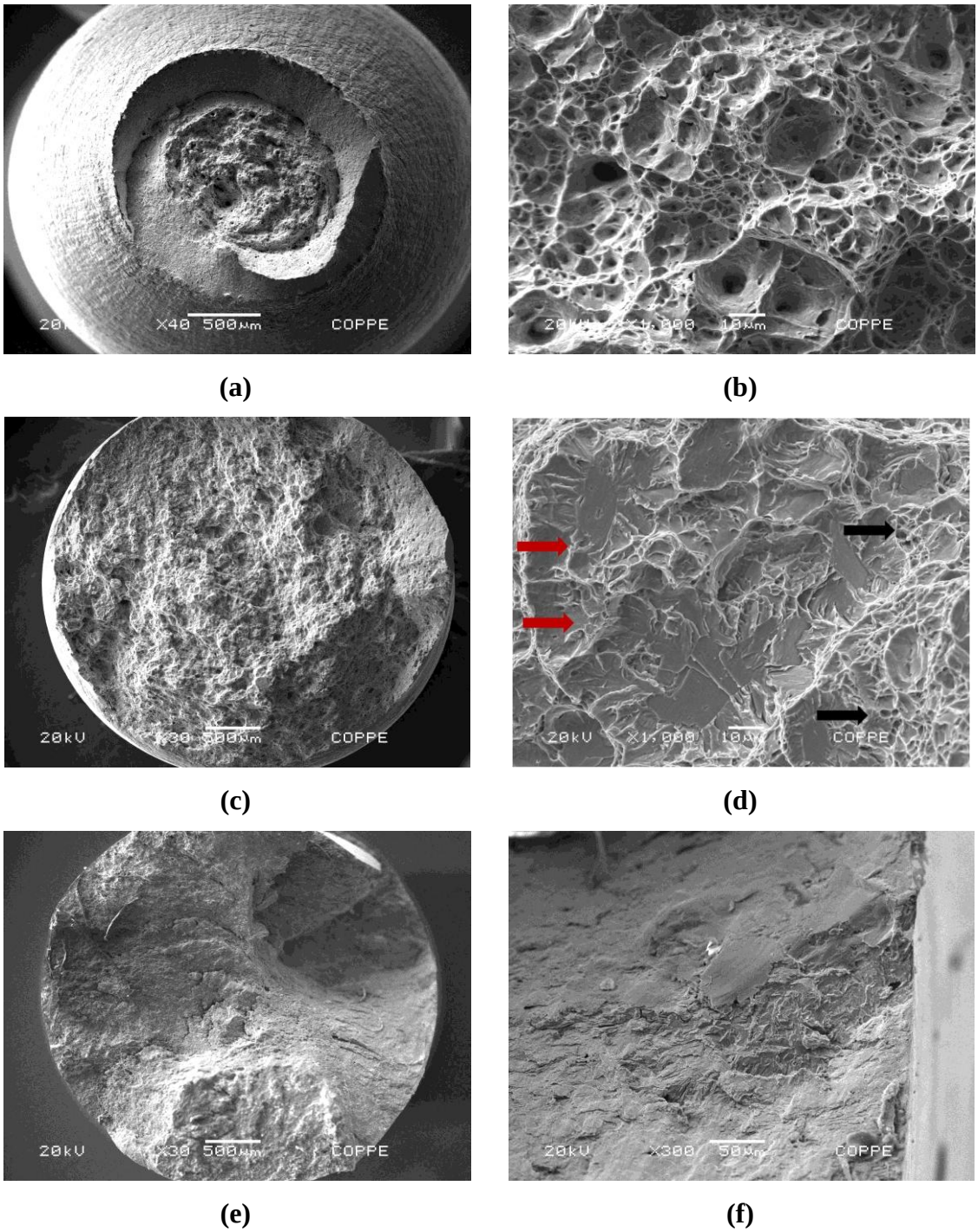


**(a)** **(b)**

**(c)** **(d)**

**(e)** **(f)**

**Figure 2:** Fracture surface of the as-quenched sample **a)** without H; **b)** magnification of a; **c)** 168h charged sample cathodically charged; **d)** Magnification of C; **e)** SSRT test condition; **f)** magnification of e.

***Chi sample***

The tensile test results for chi-sample with and without hydrogen charging are summarized in figure 3 and table 3.

The YS and UTS increased for the 168h charged sample charged tested sample and decreased for the SSRT tested sample when compared with the sample tested without H charging. On the other hand, the elongation and reduction of area for both H charged condition tests: 168 h charged and SSRT decreased 71 and 82%, respectively. As showed on the previous work [12] this complex microstructure (M; $\gamma_{ret,}$ $\chi$-phase and precipitates rich in Mo and Cr) presented $D_{app} = 2.1x10^{-12}$ $m^2.s^{-1}$ and a high hydrogen solubility ($S_{app}$ = 904mol.H.$m^{-3}$) with many preferential sites to trap the hydrogen reversibly, which are responsible to promote the hydrogen embrittlement in this sample. To support these affirmations, the desorption peak temperature was 143°C [12], indicating the presence of diffusible hydrogen to promote the hydrogen embrittlement.

Although the time to hydrogenated the SSRT samples was lower than for the 168h charged sample charged sample, and the distance reached for hydrogen during the charging time was 2.26mm for the 168h charged sample charged sample and 0.25mm for the SSRT sample, the second one presented a higher EI; i.e 0.8 for SSRT and 0.7 for 168h charged sample.

The chi phase shows a body centered cubic structure with a lattice parameter of 8.8Å [19], therefore, incoherent with the matrix, once the ferrite has a lattice parameter of 2.8 Å. Due to their large sizes, these precipitates beyond absorbing hydrogen on the interface, also allow its inflow and accumulation in the matrix.

Cieslak et. al. [20] developed in lab a sample rich in $Fe_{53.8}Cr_{46.2}$ (called sigma-phase), saturated it with hydrogen and observed that the lattice parameter of this phase increased with the hydrogen presence. Cieslak et. al. [20] concluded that not only the hydrogen is trapped in the interface, it is also present inside the phase, attaching itself to the interstices, increasing the "phases's" capacity for hydrogen absorption. Furthermore, the sigma-phase is fragile to hydrogen and the crack in the matrix develops from the precipitate. Since the hydrogen is responsible to increase the dislocation mobility as well as the interatomic distance (decohesion), causing a distortion in the lattice, this effect has been maximized in the low deformation rate testing due to the increase in the local hydrogen absorption by these incoherent precipitates.

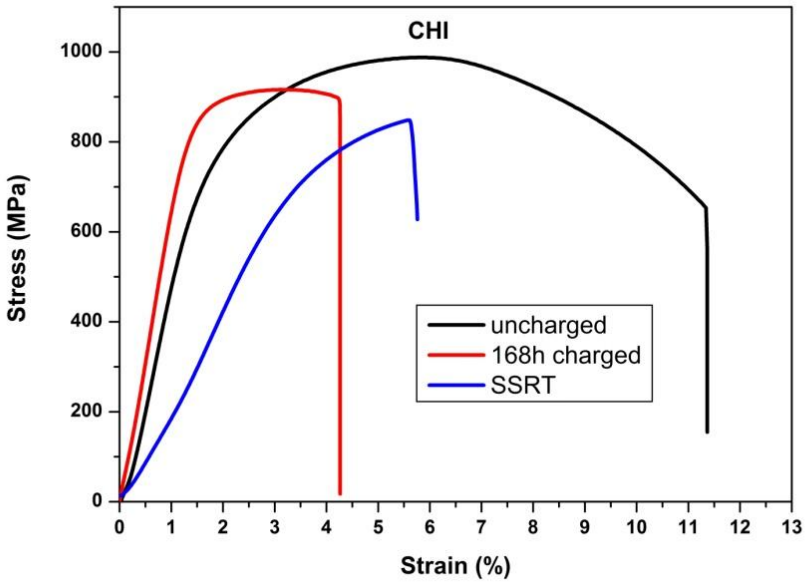


**Figure 3:** Tensile tests results for the Chi- ample uncharged, 168h charged sample with H and SSRT condition

**Table 3:** Summary the tensile tests performed on the chi sample with and without H charging.

| Sample | YS (MPa) | UTS (MPa) | Strain (%) | Reduction of Area (%) | Embrittlement Index (EI) |
|---|---|---|---|---|---|
| Without H | 703 | 938 | 10.0 | 40.5 | - |
| 168h charged sample | 817 | 987 | 2.9 | 8.1 | 0.7 |
| SSRT | 696 | 848 | 1.8 | 10.4 | 0.8 |

The SEM images for these samples are shown in figure 4. The sample without H (figure 4a and 4b) presented a fracture surface with secondary cracks (see red arrows fig. 1a) and low reduction of area (40.5% - table3). In figure 4b, some secondary cracks and small dimples were identified indicating microvoid coalescence (MVC). In this sample, the chi-phase had a deleterious effect in the steel, promoting a smaller reduction of area even when tested without hydrogen.

Nevertheless, the samples charged with H presented brittle intergranular fracture with very small dimples, indicating localized plasticity (figure 4c and 4d). Tavares et. al. [18] studied a martensitic-ferritic stainless steel with a phase rich in Cr and Mo at the grain boundaries and observed the same brittle intergranular fracture with small dimples, they [18] attributes this feature to the phase at the grain boundary. According to Kirchheim

[21] dislocations emitted from the crack tip allow crack opening and vacancies attracted by the stress field towards the tip agglomerate and form voids in front of the crack, therewith the ligaments between the voids break with local plasticity with a macroscopically brittle characteristic. The SEM image of SSRT sample (figure 4e and 4f) confirms the planar slip enhanced with elongated voids and facets decorated with slip traces (see black arrows fig.4f), supporting the maximized effect discussed above.

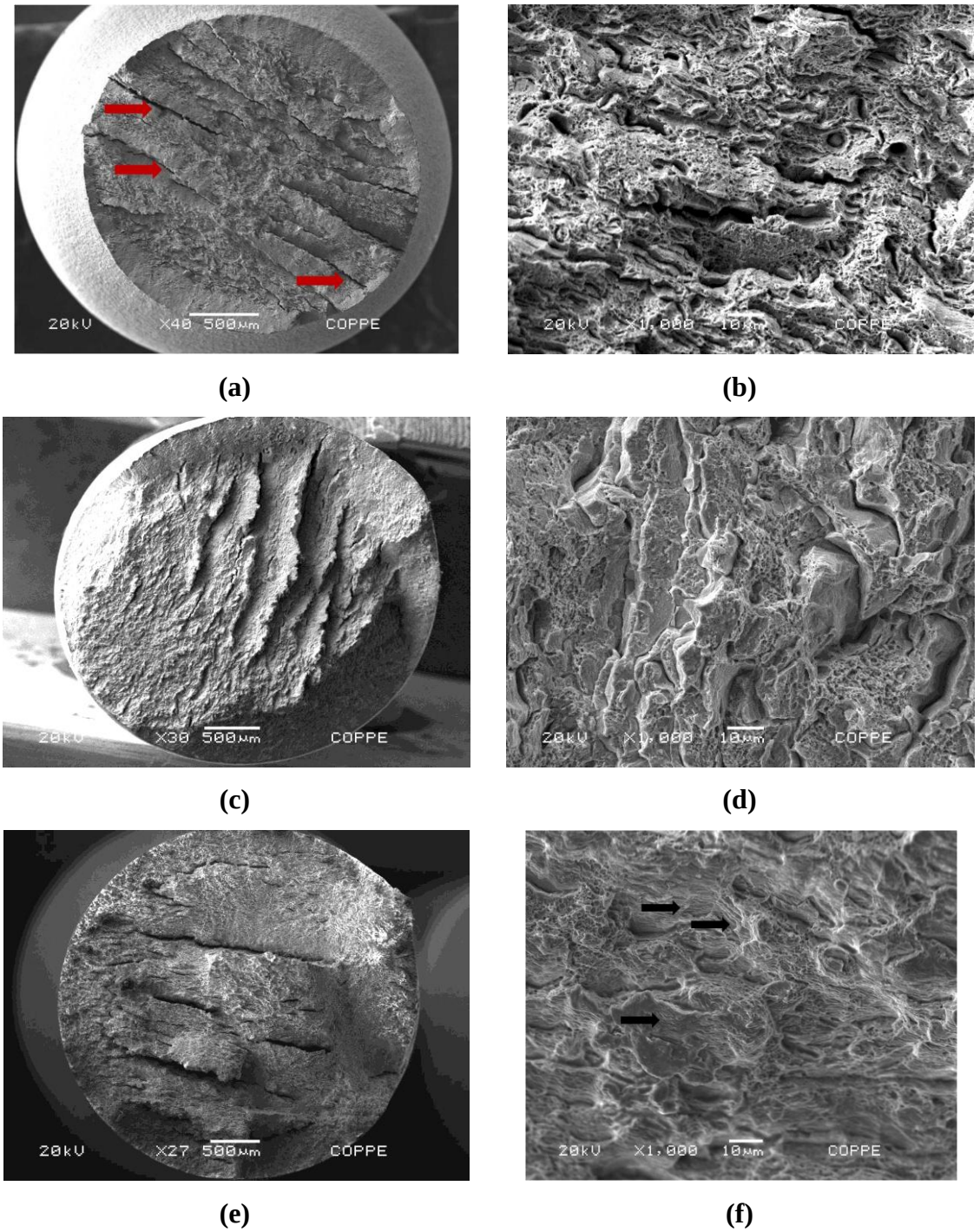


**(a)** **(b)**

**(c)** **(d)**

**(e)** **(f)**

**Figure 4:** Fracture surface of the Chi-sample **a)** without H; **b)** magnification of a; **c)** 168h charged sample cathodically charged; **d)** Magnification of C; **e)** SSRT test condition; **f)** magnification of e.

***Low Retained Austenite sample - LRA***

The tensile test results for the LRA sample with and without hydrogen charging are summarized in figure 5 and table 4

As observed in the as-quenched and chi samples, the YS for the LRA sample increased with hydrogen charging. On the other hand, the EI and reduction of area decreased with H, what was already expected since the sample presented a desorption temperature peak at 132°C ***[*this value comes from the paper 4 in the next topic of this thesis]*** indicating the presence of diffusible hydrogen, and, consequentially, probable hydrogen embrittlement. The reduction of area and EI were more pronounced for the sample tested in the SSRT condition, i.e. 7.9% (SSRT test) versus 20.9% (168 h charging) for reduction of area and 0.8 (SSRT test) versus 0.7 (168 h H charging sample) for EI.

Considering the microstructure of this sample (3% of $\gamma_{ret}$, 20% of ferrite and 77% of martensite) [22] the feasible explanation given by Hilditch et. al. [22] is that since the fracture initiated at the martensite/ferrite interfaces, it can be assumed that the hydrogen preferentially migrates to such interfaces during charging and gained importance at a lower deformation rate, where diffusible hydrogen is enabled to diffuse to critically highly stressed regions and to the interface of ferrite/martensite during the tensile test. Depover et. al. [1] studied a dual-phase steel with ferrite plus martensite, and also observed a higher hydrogen embrittlement for this steel when tested in a lower deformation rate, and also attributes this fact to the Hilditch explanation [22].

In order to verify the crack propagation, the tensile sample from 168h charged sample cathodically charged with hydrogen after test, was cut in a longitudinal direction and the longitudinal surface was observed by SEM. As observed in figure 6, the crack propagated preferably from the ferrite/martensite interface and also crosses the martensite phase, showing the brittleness of this phase.

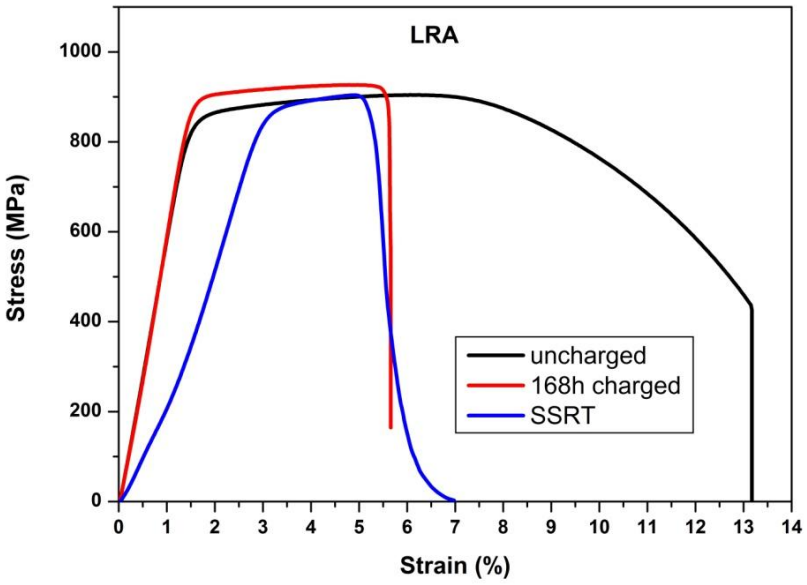


**Figure 5:** Tensile tests results for the LRA sample uncharged, 168h charged sample with H and SSRT condition

**Table 4:** Summary the tensile tests performed on the LRA sample with and without H charging.

| Sample | YS (MPa) | UTS (MPa) | Elongation (%) | Reduction of Area (%) | Index Embrittlement |
|---|---|---|---|---|---|
| Without H | 843 | 918 | 12.4 | 77.3 | - |
| 168h charged sample | 897 | 936 | 4.0 | 20.9 | 0.7 |
| SSRT | 861 | 886 | 1.9 | 7.9 | 0.8 |

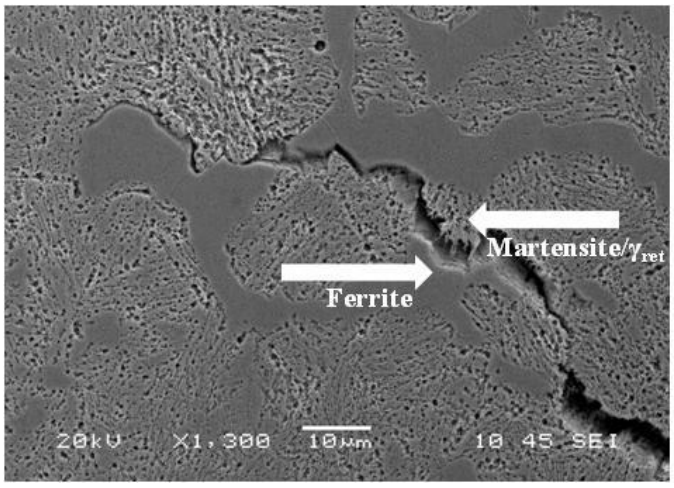


**Figure 6:** Crack propagation in LRA sample after tensile test in the longitudinal direction.

The fracture surface analyzed by SEM for these samples is shown in figure 7. As can be observed, the sample tested without hydrogen charging follows the same trend as the as-quenched sample, i.e. the fracture surface was ductile presenting dimples with MVC (figure 7a and 7b). A further similarity between these samples (as-quenched versus LRA) is the reduction of area parameter, which was 78.2% for the as-quenched sample (see table 2) and 77.3% for the LRA sample (see table4). This result is in good agreement, since the difference between these samples are just 2% of retained austenite in the LRA sample, which leads to a conclusion that the amount of retained austenite was not higher enough to produce the effect of this phase in the tensile test without hydrogen.

Nevertheless, the samples tested with hydrogen charging (168h charged sample and SSRT tests) presented a brittle fracture surface with secondary cracks in the 168h charged sample charged sample (see arrows black) and transgranular cleavage failure with hair ductile lines for both samples (168h charged sample and SSRT) as sown in figure 7. Despite the SSRT sample presented a higher EI and a surface heterogeneity, the magnification of failure (fig 7d and 7f) showed the same trend for both tests.

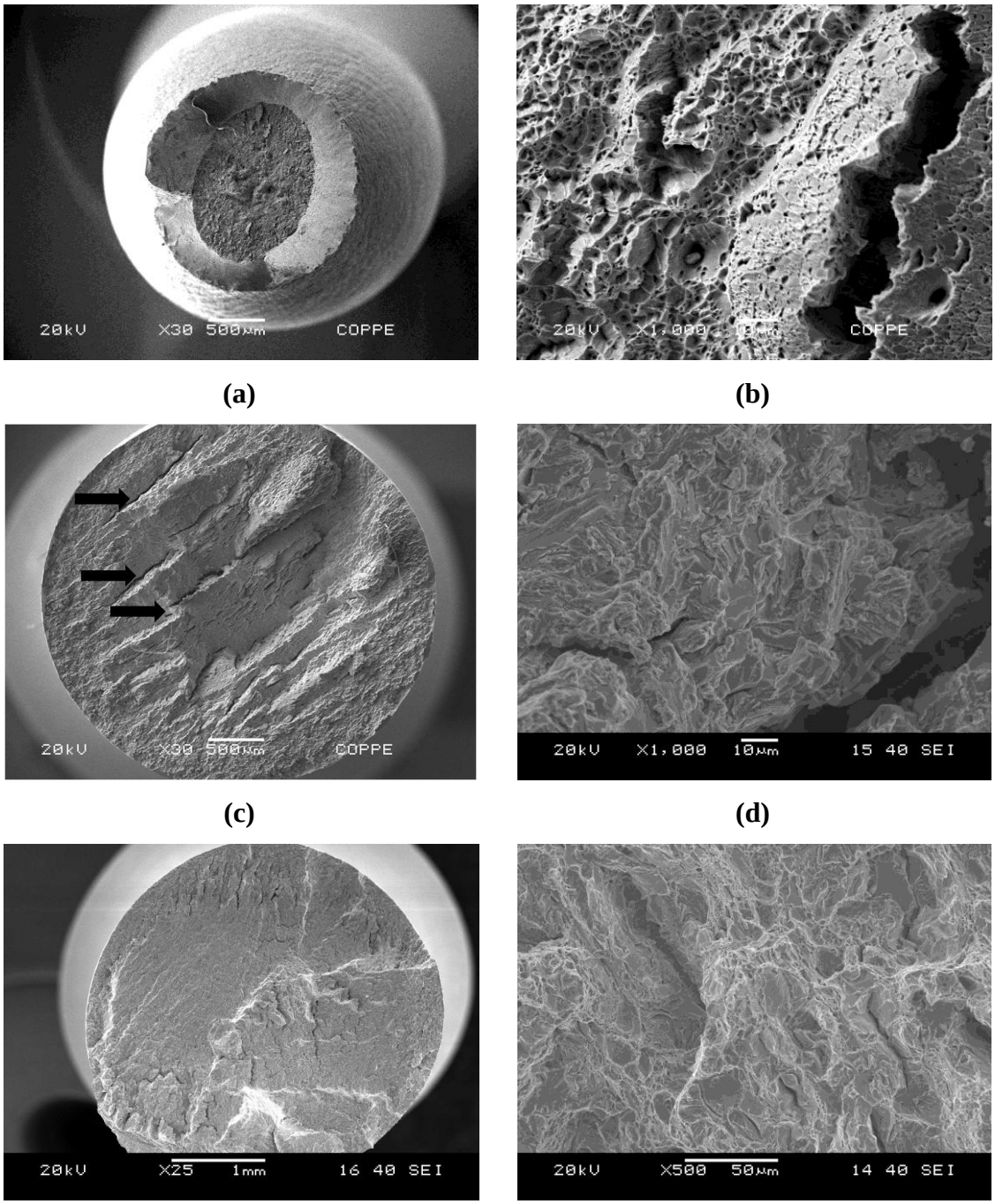


**Figure 7:** Fracture surface of the LRA sample **a)** without H; **b)** magnification of a; **c)** 168h charged sample cathodically charged; **d)** Magnification of C; **e)** SSRT test condition; **f)** magnification of e.

***Medium Retained Austenite - RA***

The tensile test results for the RA sample with and without hydrogen charge are summarized in figure 8 and table 5. As observed in the as-quenched, chi and LRA

samples, the YS for the RA samples also increased for the samples tested with hydrogen charging, showing a significant hydrogen embrittlement with a high EI.

Analyzing the desorption temperature peak (195°C) obtained by the TPD test and the high solubility of this sample (1577 mol.H.m$^{-3}$) obtained in a previous work [12], is expected a high hydrogen embrittlement in this sample, since the diffusible hydrogen is present promoting the embrittling. Despite the distance reached during the hydrogenation for SSRT was lower than reached for the 168h charged sample charged sample (0.07 and 0.69mm, respectively), the difference in strain and area reduction between the 168h charged sample test and SSRT is only 0.2 and 1% respectively. Depover [1] studied a TRIP steel with 9.3% of retained austenite at two deformation rates (5 and 0.05mm/min) and also did not find a significant difference in the reduction of area between the samples tested at the two conditions. They attributed this fact to the amount of retained austenite in that steel and the lower fraction of martensite/ferrite interface when compared with dual-phase steel. The RA sample has 20% of ferrite; 73% of martensite and 7% of $\gamma_{ret}$, [12] consequentially less martensite and less martensite/ferrite interface, but more interface martensite/$\gamma_{ret}$ interface. Taking into account, and considering that interphase boundaries are another element of the microstructure vulnerable to hydrogen, is feasible to consider that in the case of the RA sample, the retained austenite seems to play an important role on the embrittling of this sample. To corroborate this argument, the figure 9 shows the crack propagation of the sample tested after 168h charged sample hydrogen charging and can be observed that the crack follows the martensite/ferrite interface and crosses martensite/$\gamma_{ret}$ phases.

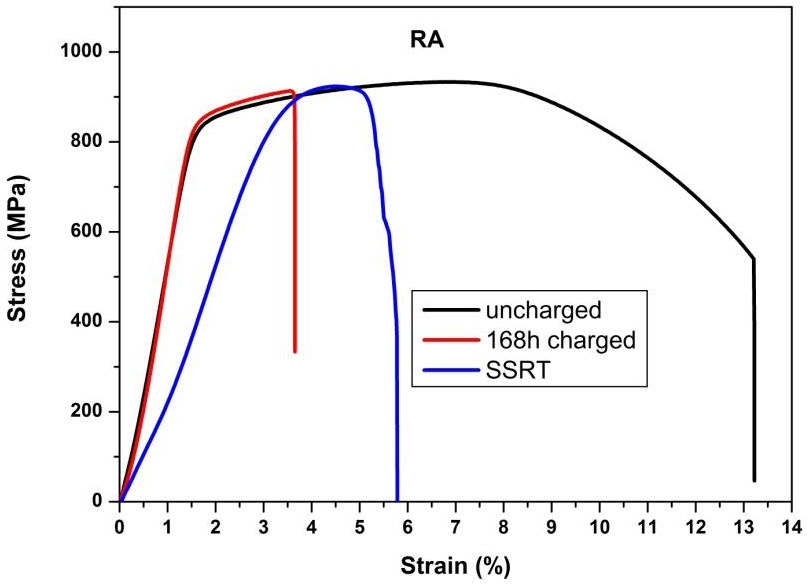


**Figure 8:** Tensile tests results for the RA sample uncharged, 168h charged sample with H and SSRT condition.

**Table 5:** Summary of results of the tensile tests performed on the RA sample with and without H charging.

| Sample | YS (MPa) | UTS (MPa) | Strain (%) | Area Reduction (%) | Index Embrittlement |
|---|---|---|---|---|---|
| Without H | 831 | 918 | 12.2 | 70.0 | - |
| 168h charged sample | 907 | 942 | 2.0 | 10.1 | 0.8 |
| SSRT | 856 | 916 | 1.8 | 8.9 | 0.9 |

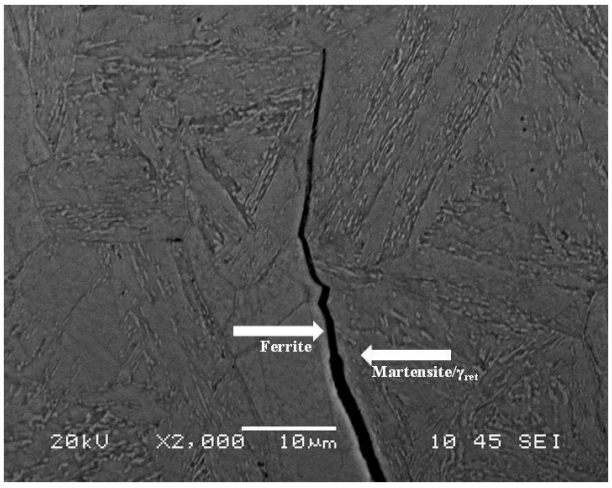


**Figure 9:** Crack propagation in RA sample after tensile test in the longitudinal direction

The SEM images for these samples are shown in figure 10. The sample tested without hydrogen charging followed the same trend of the chi-sample, i.e presenting a fracture surface with secondary cracks, low reduction of area and dimples indicating MVC (figure 10a and 10b). The samples tested with hydrogen charging presented intergranular brittle surface with secondary cracks for the 168h charged sample and transgranular cleavage failure with hair ductile lines for the SSRT test. These differences can be attributed to the explanation of dislocation mobility that hydrogen facilitates, and the planar slip of dislocations leading to a deformation in bands. Voids nucleate at the intersections of such bands leading to a transgranular fracture with different morphologies [23].

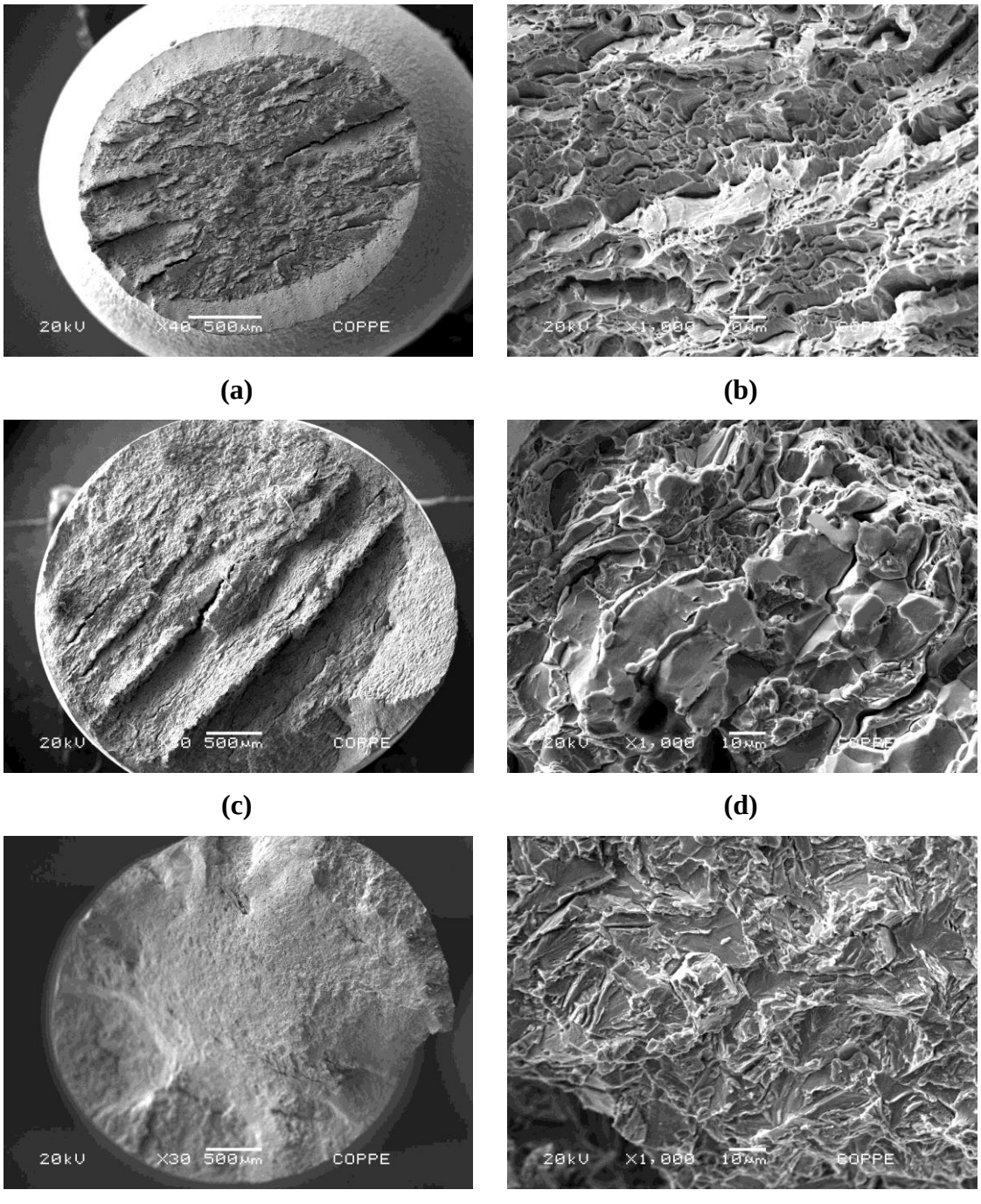


**(a)** **(b)**

**(c)** **(d)**

**(e)** **(f)**

**Figure 10:** Fracture surface of the RA sample **a)** without H; **b)** magnification of a; **c)** 168h charged sample cathodically charged; **d)** Magnification of C; **e)** SSRT test condition; **f)** magnification of e.

***High Retained Austenite - HRA***

The tensile test results for the HRA sample with and without hydrogen charge are summarized in figure 11 and table 6.

The results of YS, UTS, El and reduction of area for HRA sample followed the same trend of all the samples tested with hydrogen charging, i.e. increases in the YS and UTS parameters, and decreases in strain and in reduction of area.

The EI was also high for both samples tested with hydrogen charging, showing a high hydrogen embrittlement, but less comparing it to all the samples above (as-quenched, Chi, LRA and RA). As observed for all the samples discussed above, TPD test also presented a desorption temperature peak for diffusible hydrogen at 152°C ***[*this value comes from the paper 4 in the next topic of this thesis]*** , indicating hydrogen deleterious features in this microstructure.

The hydrogen embrittlement for the168h charged sample was higher than for the SSRT tested samples. These samples have a high amount of retained austenite with a low diffusion coefficient ($D_{app}$ = 3.4x$10^{-13}$ $m^2.s^{-1}$) [13], therefore the distance reached for the hydrogen was insufficient for the 168h charged sample and for the SSRT sample (0.71 and 0.08mm respectively). Despite the timing to hydrogenate the samples was not enough to saturate the sites with hydrogen, it was possible to identify a high embrittlement in both tested condition samples. Due to the low $D_{app}$ and a high amount of retained austenite, the most of the hydrogen was trapped in the austenite interface. The embrittled region promoted by hydrogen was around 500µm along the thickness (see figure 12c), that corroborates with the statement of no saturation pointed above.

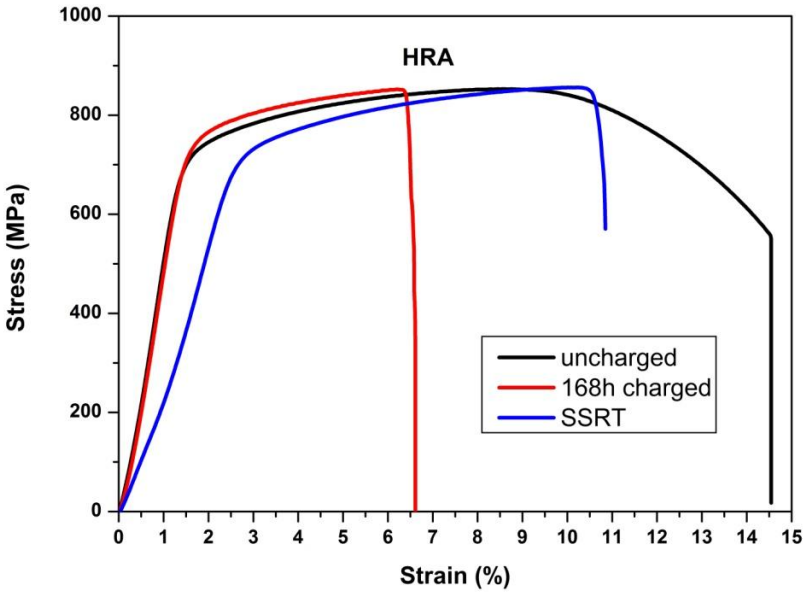


**Figure 11:** Tensile tests results for the HRA sample uncharged, 168h charged sample with H and SSRT condition

**Table 6:** Summary the tensile tests performed on the HRA sample with and without H charging.

| Sample | YS (MPa) | UTS (MPa) | Elongation (%) | Area Reduction (%) | Embrittlement Index |
|---|---|---|---|---|---|
| Without H | 694 | 847 | 13.5 | 65.0 | - |
| 168h charged sample | 715 | 832 | 6.0 | 6.8 | 0.6 |
| SSRT | 716 | 860 | 7.6 | 12.4 | 0.4 |

The SEM images for these samples are shown in figure 12. As shown, the sample tested without hydrogen charging followed the same trend of the chi and RA samples, i.e presented a fracture surface with secondary cracks and small dimples indicating MVC (figure 12a and 12b).The fracture surface for the samples tested with hydrogen are shown in figure 12c to 12f, the fracture features are brittle with small dimples, as observed on surfaces of LRA and RA samples.

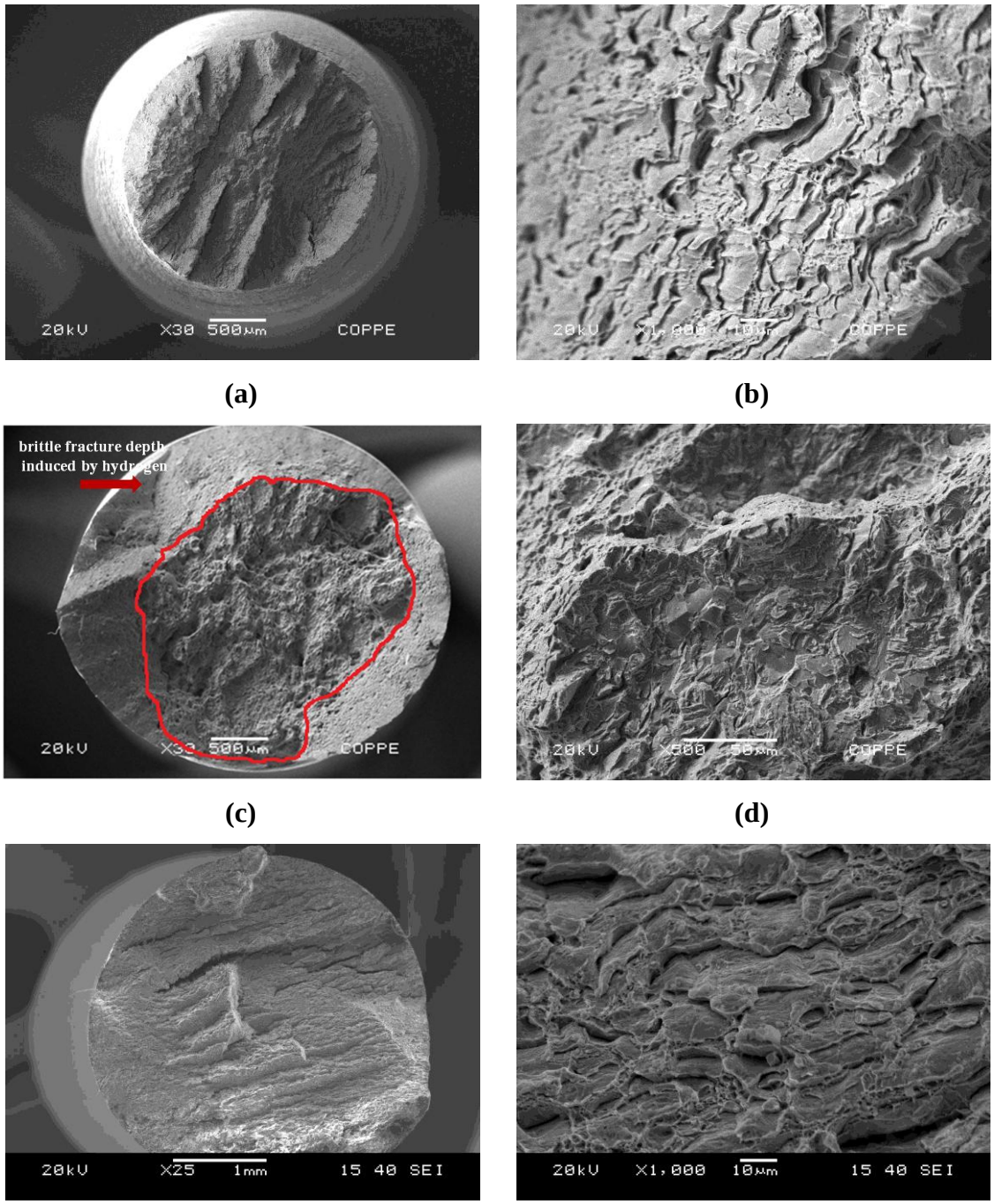


**Figure 12:** Fracture surface of the HRA sample **a)** without H; **b)** magnification of a; **c)** 168h charged sample cathodically charged; **d)** Magnification of C; **e)** SSRT test condition; **f)** magnification of e.

***YS 168h charged sample charged versus YS uncharged***

The comparison of YS for the uncharged, the 168h charged the SSRT hydrogen charged samples is shown in figure 13. Comparing the sample as-quenched (0% of retained

austenite) among LRA, RA and HRA (3, 7 and 22% of retained austenite respectively) for all tests, as the amount of retained austenite increases, the yield strength decreases. This was already expected as the austenite tends to decrease the mechanical resistance and increase the plastic deformation. Zou 2010 [24] and Ma 2012 [25] heat treated SMSS in a different condition, and obtained different amounts of retained austenite, and also observed the decrease in the YS as the amount of the retained austenite increases. Despite the chi sample contains the same amount of retained austenite of the RA sample (7%), the yield strength was lower for the chi- sample than for the RA sample. It is important to highlight that the chi sample present besides $\gamma_{ret}$, also present $\chi$-phase and precipitates rich in Mo and Cr. Moreover, the heat treatment on the chi sample was for 18h, decreasing the number of defects, thereby reducing the strength. It still seen a slight increase in yield strength for samples cathodically charged with hydrogen. Zakroczymski et. al. [26] also observed the same trend in the duplex stainless steel studied in different charging conditions. In their work, the sample pre-charged with 0.1M $H_2SO_4$ + $As_2O_3$ presented the higher YS and consequently the higher hydrogen embrittlement. Nonetheless, many authors studied different kinds of steel and have found a decrease in the YS in samples charged with H [1]. In general, it is not simple to correlate the yield strength obtained by tensile test and the microscopic effects of H on the dislocations behavior. Birbaum [23] pointed out that in the presence of slip localization, a tensile test will not determine the true yield strenght of the material. Thus the macroscopic yield strength measured in a tensile test can increase depending on the magnitude of the hydrogen enhanced dislocation velocity and on the degree of the slip localization. Measurements of the macroscopic stress strain behavior which show increases in the flow stress due to the introduction of H may result from shear localization, even in the presence of reduced barriers to dislocation motion. The effect of hydrogen on the macroscopic yield strength of metals, as measured by tensile tests, depends both on the effects of H on the dislocation stress velocity relation and on the tendency for H to cause strain localization.

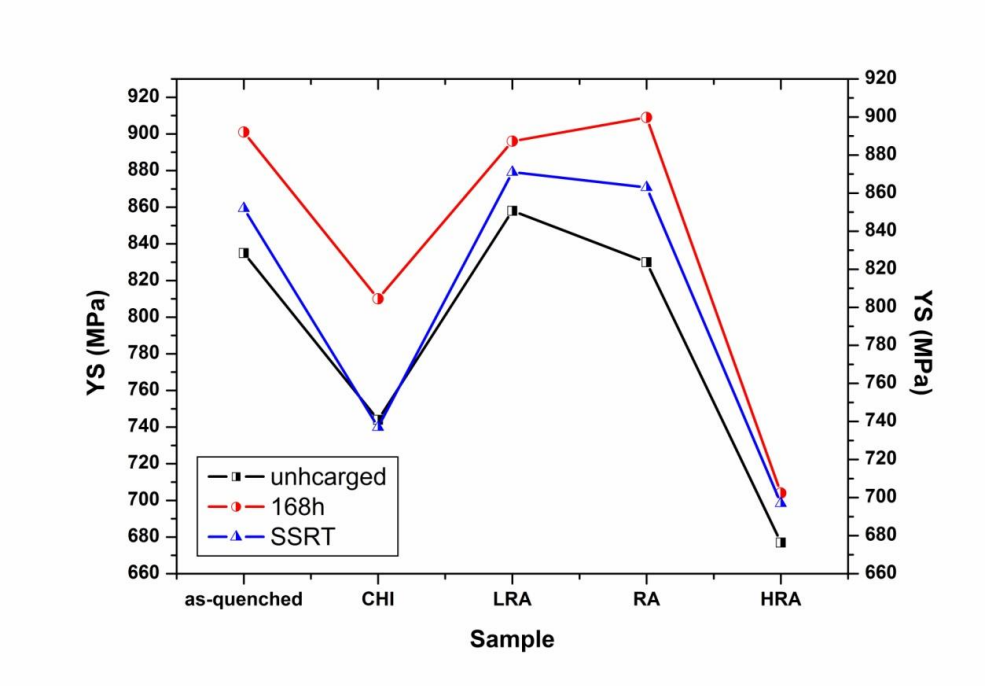


**Figure 13:** YS of uncharged, 168h charged and SSRT samples.

## Discussion

### *Embrittlement Index versus Reduction of Area - Loss ductility*

The embrittlement index was compared with loss of ductility (LD) calculated using the reduction of area in the sample with and without hydrogen charge. The results of EI versus LD are shown in figure 14. As observed, the order of hydrogen embrittlement using both parameters follows the same trend with a discrepancy only for the HRA sample, which presented a lower embrittling using EI and the same embrittlement of the RA sample using LD parameter. These results, using the LD parameter, showed a trend to increase the HE with an increase in the amount of retained austenite. These results are in good agreement with Solheim et. al. [5], who studied a supermartensitic stainless steel with different amounts of retained austenite using the LD parameter to evaluate the hydrogen embrittlement. These authors [5] found a trend to increase the HE by increasing the content of retained austenite. In the sample with 19% of retained austenite the loss of ductility was 85%, whereas on the sample with 2% of this phase the HE was 64% and the sample without $\gamma_{ret}$ showed 45% of LD. Solheim et al. [5] concluded that the higher the amount of retained austenite, the greater the hydrogen

embrittlement, and an indicative of this was suggested to be the transformation-induced plasticity effect (TRIP) of austenite to martensite.

In order to verify this effect in the sample after the tensile test for the 168h charged sample in the present work, the XRD technique was performed in the region below of fracture and very close to the necking. The results showed that the HRA sample in this region presented just 10% of retained austenite, Chi and LRA samples did not present any amount of this phase, and the RA sample presented the same 7% of retained austenite. It seems that it occurred the TRIP effect in the Chi, LRA and HRA, which can also have contributed with the high hydrogen embrittlement in these samples.

After the tensile test, the HRA sample showed an austenite fraction similar to the RA sample, a similar embrittlement was expected, since the martensite fraction values were close, i.e. 70% for the HRA sample versus 73% for the RA sample.

Another point to be considered is that the austenite of RA sample appears to have not undergone this transformation induced by plastic deformation, showing a greater stability of the austenite in this sample. As shown in work done by Santos [27] the highest austenite reversion temperature in which this phase remains retained in the microstructure after cooling is at a temperature of 675 ° C, ie at the same temperature TT of the HRA sample. This stability of retained austenite was not enough to keep the retained austenite in microstructure when submitted to the tensile testing with hydrogen charge. Due to the TRIP effect, the loss ductility parameter for the HRA sample is more reliable than the embrittlement index, as the loss of ductility refers to the necking region where the TRIP effect occurred.

Despite the explanation was done considering the TRIP effect, these data have to be confirmed with XRD test in the region close to the necking and in a region far to the necking, on the samples uncharged and charged with hydrogen.

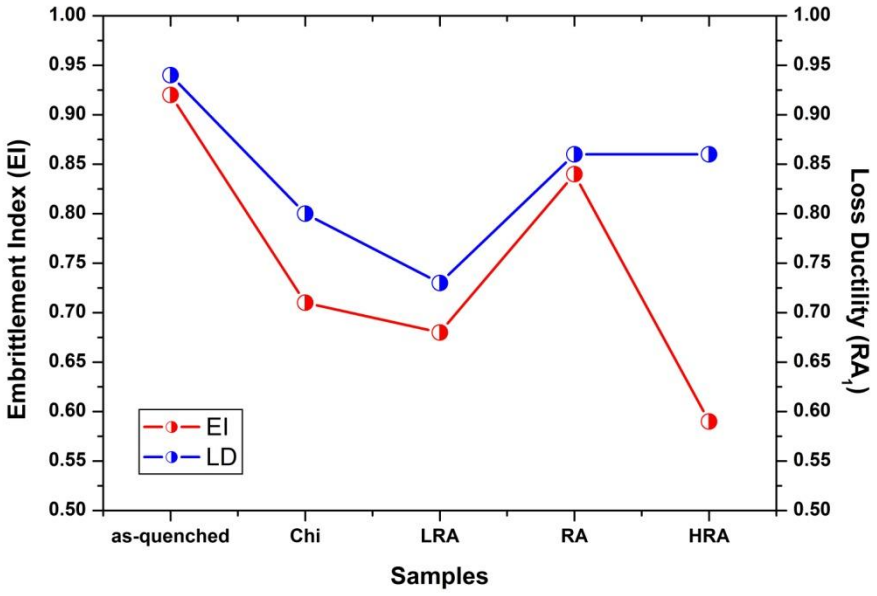


**Figure 14:** Embrittlement index versus loss ductility.

***Hydrogen concentration versus hydrogen embrittlement***

The concentration of hydrogen calculated as per the equation (3) is represented in the figure15. As described by Olden [28] C(x, t) is the sought concentration of hydrogen and $c_0$ the bulk concentration. Where the $c_1$ is a constant surface hydrogen concentration and $c_0$ is a uniform initial bulk hydrogen distribution. To solve this equation the boundary conditions established by Boes and Zuchner [29] have to be used.

t = 0: c = 0 for $0 \leq x \leq s$

t > 0: $c_0 = c_1$ and $c_s = 0$

$$c(x,t) = c_1 - c_1\frac{x}{s} + \frac{2}{\pi}\sum_1^{\infty}\frac{-c_1}{n}\sin\frac{n\pi x}{s}\exp\left(\frac{Dn^2\pi^2 t}{s^2}\right) \qquad \text{equation (3)}$$

The hydrogen concentration decreases with increasing depth, yet generating a gradient concentration between the surface and the interior of sample. These graphs show how the hydrogen evolution occurs during the hydrogenazation and what the necessary time for the reversible sites is and lattice sites are completely filled with hydrogen.

A pseudo critical concentration may be determined in function of the widths of the embrittled layers. In figure 15 this parameter was simulated for the 500 μm depth, due

the HRA sample presented clearly this brittle fracture depth induced by hydrogen (see figure 12c).

The HRA sample presented 500µm brittle fracture depth induced by hydrogen and the critical hydrogen concentration of 146mol.H.m$^{-3}$. For this sample, even with ten times the hydrogenization periods, the mid thickness concentration would be of only 108 mol.H.m$^{-3}$, that is, three times lesser than the value obtained for the stationary state of the sample (331mol.H.min$^{-1}$). An important discussion to be highlighted is that even with a low concentration in the sample interior, the amount of hydrogen before the tensile test was enough to promote a high embrittlement in this sample. This fact can be attributed to the deleterious effect of the austenite, due to the induced transformation through plastic-deformation as discussed previously, but this effect have to be further investigate.

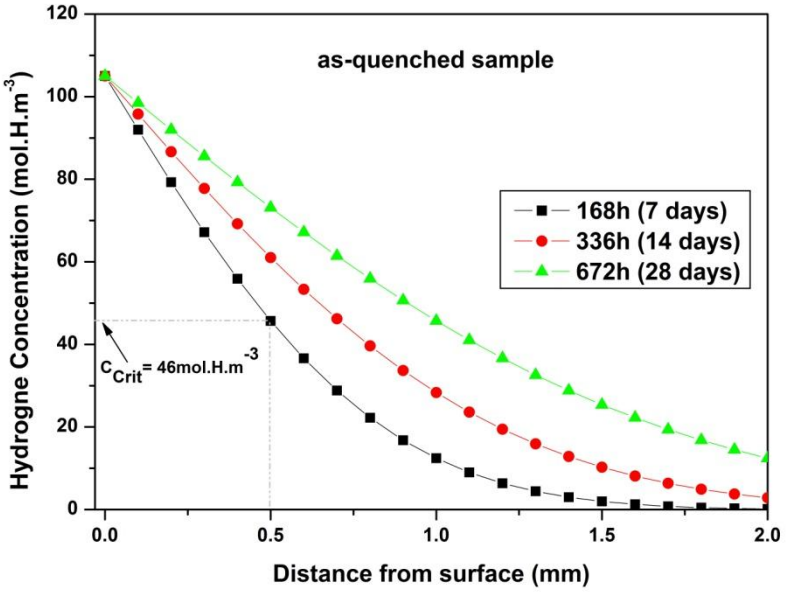


**(a)**

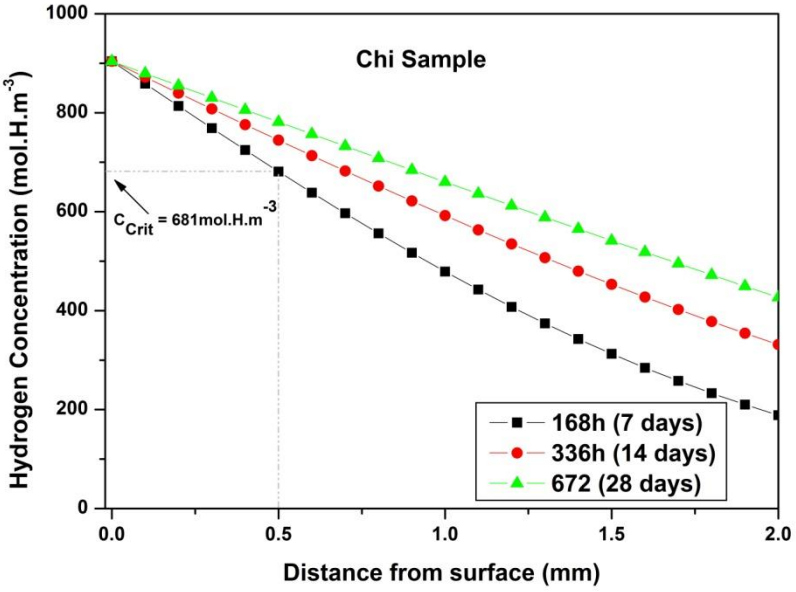
Chi Sample
Hydrogen Concentration (mol.H.m-3)
Distance from surface (mm)
C Crit = 681mol.H.m-3
168h (7 days)
336h (14 days)
672 (28 days)
0
200
400
600
800
1000
0.0
0.5
1.0
1.5
2.0

**(b)**

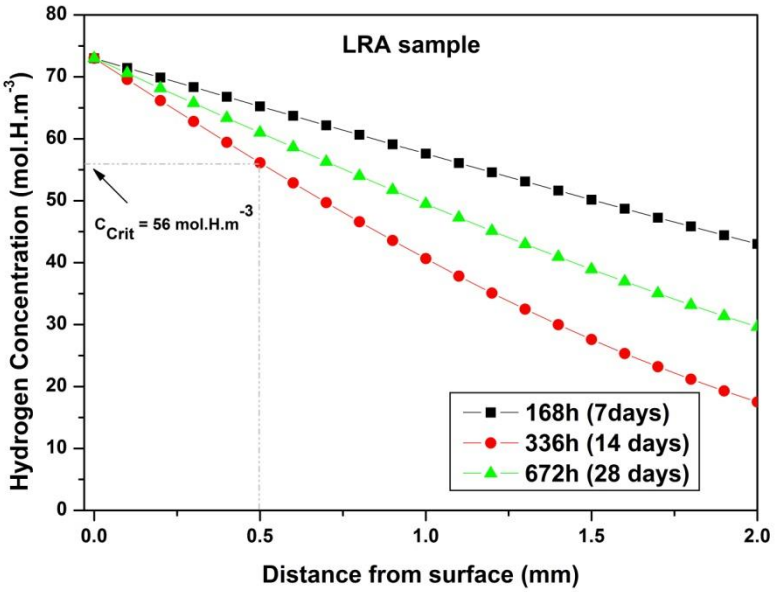
LRA sample
Hydrogen Concentration (mol.H.m-3)
Distance from surface (mm)
C Crit = 56 mol.H.m-3
168h (7days)
336h (14 days)
672h (28 days)
0
10
20
30
40
50
60
70
80
0.0
0.5
1.0
1.5
2.0

**(c)**

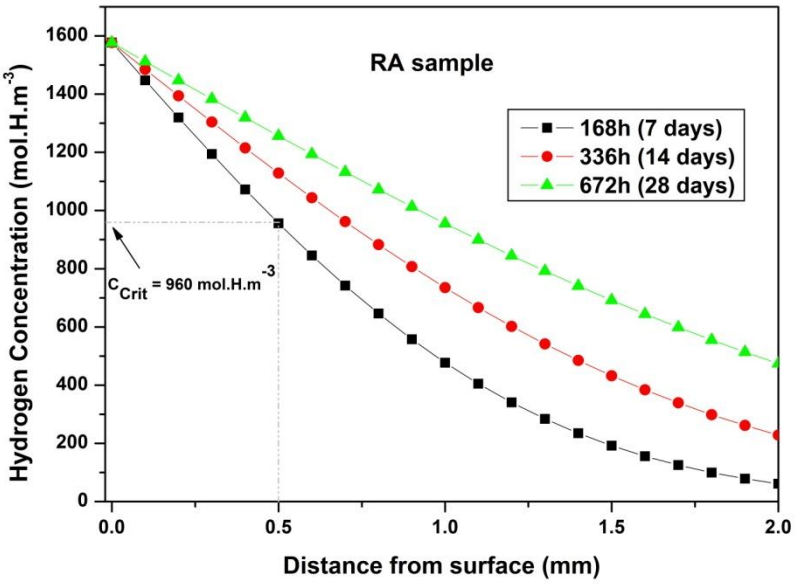


**(d)**

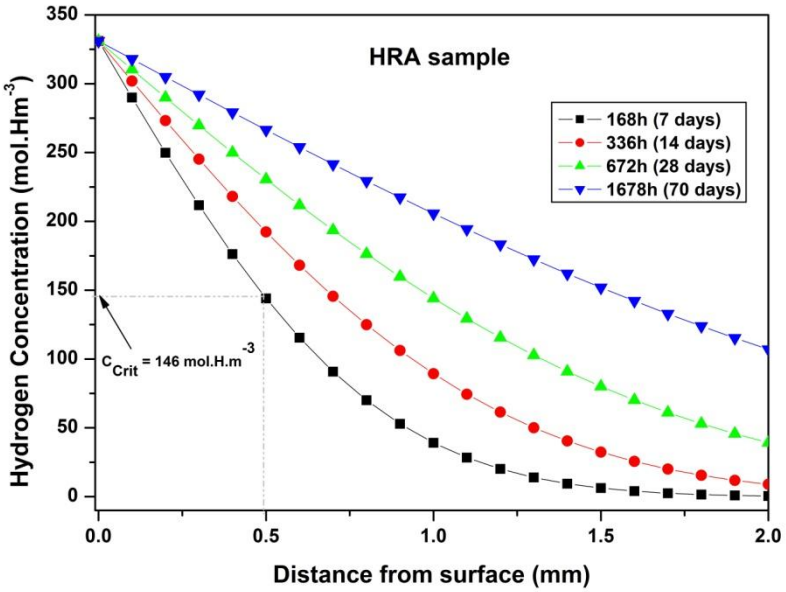


**(e)**

**Figure 15:** Hydrogen distribution in a thin plate at different times. Calculated using the thin plate diffusion model a) as-quenched sample, b) Chi-sample; c) LRA sample, d) RA sample. e) HRA sample.

## Conclusions

The ductility of tensile test samples was greatly reduced by the presence of retained austenite and chi-phase when the microstructure was charged with hydrogen prior to testing. The loss of ductility (LD) was measured by reduction of area of round bar tensile test samples. For instance, for a sample of HRA sample that contained 22% austenite, the reduction of area was 65% without hydrogen charging, and 6.8% after 168h hydrogen charging. In comparison, in the sample of LRA with 2% of retained austenite, the reduction of area was 77.3% without hydrogen charging and 20.9% after 168h hydrogen charging.

TRIP effect in the HRA sample seems to contribute to the hydrogen cracking mechanism in MFSS, but have to be further investigated. Crack propagation as a result of diffusion of hydrogen from austenite without prior phase transformation cannot be ruled out, and may be the subject of further testing.

The Chi sample with χ-phase showed high hydrogen embrittlement (LD = 80%) showing a deleterious effect of this phase, but the embrittling was lower in this sample than in the HRA sample with 22% of retained austenite (LD = 90%).

**Acknowledgments**

The authors would like to sincerely thank Vallourec Tubos do Brasil, CNPq and CAPES for their financial support.

## References

[1] Depover. T., Peréz Escobar D., Wallaert E. Zermout Z., Verbeken K. Effect of hydrogen charging on the mechanical properties of advanced high strength steels. International Journal of Hydrogen Energy 2014, 39: 4647-56.

[2] Hadam U., Zakrozymski T. Abosrption of hydrogen in tensile strained iron and high-carbon steel studied by electrochemical permeation and desorption techiniques. International Journal of Hydrogen Energy 2009, 34: 2449-59.

[3] Li D., Gangloff R. P., Scully J. R. Hydrogen Trap States in Ultrahigh-Strength AERMET 100 Steel. Metallurgical and Materials Transactions A 2004, 35A: 849-64

[4] Park B.Y.D., Maroef I.S., Landau A., Olson D.L. Retained Austenite as a Hydrogen Trap in Steel Welds Hydrogen trapping is investigated as a means of improving

resistance to hydrogen-assisted cracking in HSLA steels. WELDING JOURNAL 27S-35S.

[5] Solheim K. G., Solberg J. K., Walmsley J., Rosenqvist F. The role of retained austenite in hydrogen embrittlement of supermartensitic stainless steel. Engineering Failure Analysis 2013, 34: 140-49.

[6] Escobar P.D., Verbeken K., Duprez L., Verhaege M. Evaluation of hydrogen trapping in high strength steels by thermal desorption. Materials Science and Engineering A 2012, 551:50– 58.

[7] Eliaz N., Shachar A., Tal B., Eliezer D. Characteristics of hydrogen embrittlement, stress corrosion cracking nad tempered martensite embrittlement in high-strength steels. Engineering Failure Analysis 2002, 9:167-84.

[8] Sojka J., Vodarek V., Schindler I., Jerome Ly. M., Vánová P., Ruscassier N. Wenglorzova A. Effect of hydrogen on the properties and fracture characteristics of TRIP 800. Corrosion Science 2011, 53:2575‑81.

[9] Koyama M., Tasan C. C., Akiyama E., Tsuzaki K., Raabe D. Hydrogen-assisted decohesion and localized plasticity in dual-phase steel.Acta Materialia 2014, 70:174–87.

[10] Michler T., Lee Y., Gangloff R. P., Naumann J. Influence of macro segregation on hydrogen environment embrittlement of SUS 316L stainless steel. International Journal of Hydrogen Energy 2009, 34:3201-09.

[11] Marchetti L., Herms E., Laghoutaris P., Chêne J.Hydrogen embrittlement susceptibility of tempered 9%Cr-1%Mo steel. International Journal of Hydrogen Energy 2001, 36: 15880-87.

[12] Garcia D.C.S., Carvalho R.N., Lins V.F.C., Rezende D.M., Dos Santos D.S. Influence of microstructure in the hydrogen permeation in martensitic-ferritic stainless steel, International Journal of Hydrogen Energy 2015, http://dx.doi.org/10.1016/j.ijhydene.2015.06.102

[13] Garcia D.C.S., Carvalho R.N., Lins V.F.C., Dos Santos D.S. Influence of retained austenite in the hydrogen diffusion in martensitic-ferritic stainless steel, submitted to International Journal of Hydrogen Energy 2015/October.

[14] Pressouyre GM. Trap theory of hydrogen embrittlement. Acta Metallurgica 1979; 28: 895-911.

[15] Birnbaum H. K., Sofronis P. Hydrogen-enhanced localized plasticity-a mechanism for hydrogen related fracture. Materials Science and Engineering, A 1994, 176: 191-02.

[16] Sojka J. Vodárek V., Schindler I., Lyb C., Jérôme M., Vánová P., Ruscassier N., Wenglorzová A. Effect of hydrogen on the properties and fracture characteristics of TRIP 800 steels. Corrosion Science 2011, 53: 2575–81.

[17] Martin M., Weber S., Theisen W., Michler T, Naumann J. Effect of alloying elements on hydrogen environment embrittlement of AISI type 304 austenitic stainless steel. International Journal of Hydrogen Energy 2011, 36: 1588-98.

[18] Tavares S.S.M. , Bastos I. N., Pardal J.M., Montenegro T.R., Silva M.R. Slow strain rate tensile test results of new multiphase 17%Cr stainless steel under hydrogen cathodic charging. International Journal of Hydrogen Energy 2015, http://dx.doi.org/10.1016/ j.ijhydene.2015.05.148.

[19] Kasper J. S. The ordering of atoms in the chi-phase of the iron chromium molybdenum system. Acta Metallurgica 1954, 2: 456-61.

[20] Cieslak J., Costa B.F.O., Dubiel S.M., Fruchart D. Skryabina N.E. Hydrogen effect on the sigma-phase in Fe53.8Cr46.2. Journal of Alloys and Compounds 2009, 467: 182–86.

[21] Birnbaum H. K. Hydrogen effects on deformation – retaltion between dislocation behavior and the macroscopic stress-strain behavior. Scripta Metallurgica *et* Materialia 1994, 31 (2): 149-53.

[22] Hilditch TB, Lee S-B, Speer JG, Matlock DK. Response to hydrogen charging in high strength automotive sheet steel products. SAE Technical Paper 2003-01-0525, http://dx.doi.org/10.4271/2003-01-0525; 2003.

[23] Robertson I.M. Birnbaum H.K. Dislocation mobility and hydrogen – a brief review. Department of Materials Science and Engineering, University of Illinois, Urbana, IL 61801 USA.

[24] Zou D.N., Han Y., Zhang W., Fang X.D. Influence of Tempering Process on Mechanical Properties of 00Cr13Ni4Mo Supermartensitic Stainless Steel. Journal of

[25] Ma X.P., Wang L.J., Liu C.M., Subramanian S.V. Microstructure and properties of 13Cr5Ni1Mo0.025Nb0.09V0.06N super martensitic stainless steel Materials Science and Engineering A 2012, 539: 271–79.

[26] Hadam U., Zakroczymski T. Absorption of hydrogen in tensile strained iron and high-carbon steel studied by electrochemical permeation and desorption techniques. International Journal of Hydrogen Energy 2009, 34: 2449-59.

[27] Santos T.A.A., Carvalho R. N., Rocha A. C., Ferreira M.A.C., Buono V.T.L. Estudo da Reversão da Austenita em um aço inoxidável martensítico-ferrítico. 69º

Congresso Anual da ABM – Internacional, 14º ENEMET - Encontro Nacional de Estudantes de Engenharia Metalúrgica, de Materiais e de Minas, 21 a 25 de julho de 2014, São Paulo, SP, Brasil.

[28] Olden V, Thaulow C, Johnsen R. Modelling of hydrogen diffusion and hydrogen induced cracking in supermartensitic and duplex stainless steels. Materials and Design 2008, 29: 1934-48.

[29] Boes N, Zuchner H. Eletrochemical methods for studying diffusion permeation and solubility of hydrogen in metals. J Less-Common Metals 1976; 49: 223-40.

# *CHAPTER 4*

## *PAPER 4: Hydrogen trapping in martensitic-ferritic stainless steel*

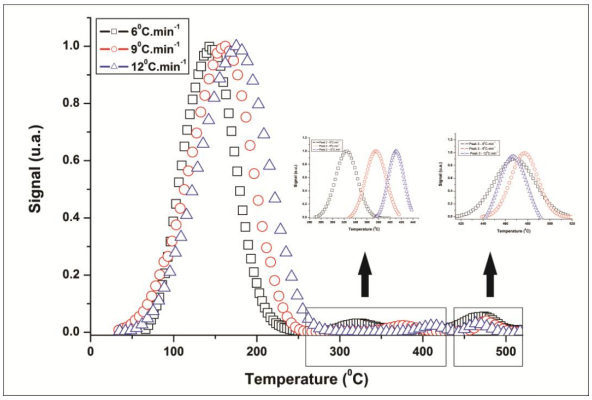


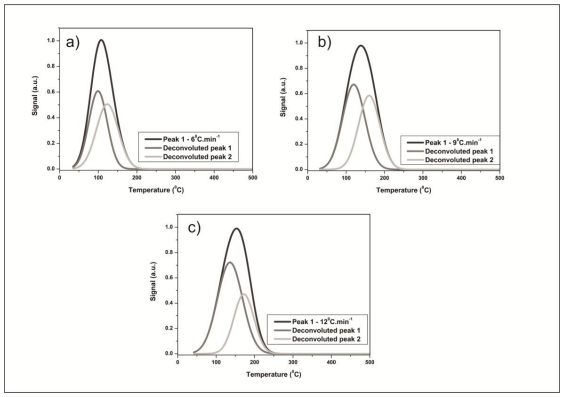

## Abstract

Hydrogen trapping in martensitic-ferritic stainless steel was investigated by using thermal desorption spectroscopy technique. The samples were tested in 6, 9 and 12°C.min$^{-1}$ heating rate and the activation energy (Ea) was calculated for the 1st deconvoluted peak of all the heating rates and samples. As results the sample called HRA with 22% of retained austenite showed the highest desorption peak temperature.


## Introduction

The hydrogen can be trapped on the microstructure of the material reversibly or irreversibly, and depends on the trap binding energy it will be classified as reversible or irreversible traps. Trap binding energy and distribution in the microstructure can provide further understanding of the role of H trapping in solubility, diffusivity, and embrittlement, and the thermal desorption spectroscopy (TDS) method is well suited to provide such detailed information about these characteristics on the material [1]. This technique allows distinguish the hydrogen traps in the material based on determination of the peak temperatures for hydrogen desorption during heating. Besides to reveal the hydrogen trap sites, this method can classify them both qualitatively and quantitatively into strong or/and weak traps [2]. This technique is advantageous due the capacity to detect hydrogen as a probe; even in small quantities; and is faster than other techniques when it comes to detect phases with low diffusion coefficient, e.g. retained austenite.
For retained austenite whose diffusion coefficient is low, this method is appropriate to classify the reversible and irreversible hydrogen traps [3].
The aim of this study is to investigate the characteristics of traps present in the martensitic ferritic stainless steel with different amounts of retained austenite and chi-phase by TDS method using different heating rate.

## Experimental Details

The samples used in the present work as the five samples used in the previous work [4,5], i.e. as-quenched, chi, LRA, RA and HRA. The thermal desorption spectroscopy

(TDS) was made using a heating rate of 6, 9 and 12°C.min$^{-1}$ in vacuum environments desorbing the hydrogen detected by a mass spectrometer (QMA200-PFEIFFER) as described in the previous work [4]. The samples were hydrogenated according to the diffusion coefficient of each microstructure, (using NaCl 3.5 wt% solution, pH 4.0 adjusted by sodium acetate), as the same way described on the previous works from these authors [4]. The procedure used to hydrogenate the samples was the same cited in the reference [4] and the details are shown in table 1.

**Table 1:** Hydrogenation condition of TDS tests.

| Sample | Current Density (mA.cm$^{-2}$) | Thickness (cm) | Sample size (mm) | Hydrogenation time (h) |
|---|---|---|---|---|
| As-quenched | 43.0 | 0.043 | 3.67 x 20.5 | 3 |
| Chi | | 0.047 | 3.55 x 18.2 | 18 |
| LRA | | 0.027 | 4.32 x 12.98 | 96 |
| RA | | 0.081 | 2.72 x 15.5 | 24 |
| HRA | | 0.044 | 3.00 x 19.58 | 48 |

In order to calculate the binding energy of the trap the Lee and Lee's model was applied [5,6]. According to their work, the hydrogen evolution rate as a thermally activated process from trap sites is given by equation 1.

$$\frac{dx}{dt} = A(1-X)exp^{(-E_a/RT)} \qquad equation\ (1)$$

Where X is the hydrogen content that escapes a trap, A is the reaction rate constant, Ea is the activation energy for releasing hydrogen from its trapping site, R is the gas constant and T is the absolute temperature. The activation energy for hydrogen desorption from a certain trap can be calculated by the shift of the peak temperature of different heating rates. By imposing a linear change of temperature, ϕ, the activation energy of the rate determining desorption process (Ea) is obtained by equation 2 [5,6]:

$$\frac{dln\left(\phi/T_c^2\right)}{d\left(1/T_c\right)} = -\frac{E_a}{RT} \qquad equation\ (2)$$

Where $T_c$ is the peak temperature and $\phi$ is the heating rate. Thus by plotting $\ln(\phi/T_c^2)$ versus 1/Tc ,where Tc is the critical temperature for hydrogen evaluation from a trap site, this should yield straight lines with the slope -Ea/R [7].
In the present work the activation energy (Ea) will be calculated only for the first peak desorption temperature.

## Results and Discussion

### *As-quenched sample*

Figure 1 and table 2 show the TDS results of the as-quenched sample under investigation obtained by using the three heating rate described in experimental details. From the TDS spectra, it can be observed an increase in peak temperature with increasing heating rate; i.e. increasing heating rate causes the peaks to move to greater intensities and shift to higher temperature, indicating desorption kinetic dependences with the heating rates [8].
All heating rate presented a peak at low temperature but, only heating rate 9 and 12°C.min$^{-1}$ detected a peak at high temperature (446 and 408°C respectively). Silverstein et. al. [9] explained this phenomenon based on the fact that low heating rate allows for more time for diffusion of hydrogen, and enables the possibility to de-trap hydrogen and re-trap in higher $E_a$ trapping site.
The occurrence of these peaks at high temperature in the as-quenched sample is characteristics of retained austenite. Despite the XRD results demonstrated in another publication from the authors [4] only ferrite on the microstructure, the results from Mossbauer in the other previous work from these authors [10] showed 1% of $\gamma_{ret}$. These amounts of this phase cannot be negligible at TDS test, as the hydrogen act as a probe in the material. Therefore, it is feasible to attribute this peak for de-trap in $\gamma_{ret}$ interface thus proving the irreversible nature of this phase and showing the sensibility of TDS technique to identify the traps in the material.

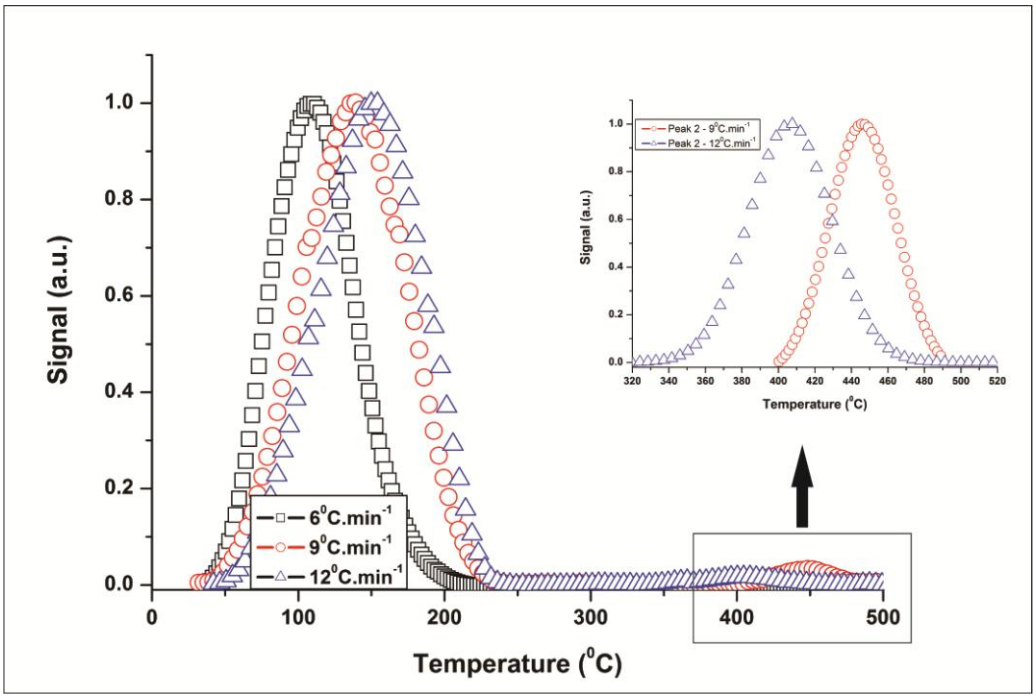


**Figure 1:** TDS results for the as-quenched sample. Heating rate 6, 9 and 12°C.min$^{-1}$ with the zoom in the 2nd desorption peak temperature.

**Table 2:** Desorption temperature for peak 1 and 2 of 6, 9 and 12°C.min$^{-1}$ heating rate.

| **Heating Rate (°C.min$^{-1}$)** | **Peak 1 (°C)** | **Peak 2 (°C)** |
|---|---|---|
| 6 | 109 | - |
| 9 | 138 | 446 |
| 12 | 153 | 408 |

Figure 2 presents the results of the deconvolution procedure used in the as-quenched sample tested at heating rate of 6, 9 and 12°C.min$^{-1}$. It was observed that the low temperature peak could be fitted nicely with two distinct peaks (figure 2a, 2b and 2c). The deconvolution of the peak allowed determining the peak temperature for every heating rate and distinct better the nature of the trap. With this peak temperature is possible to obtain the value of $\ln(\phi/T^2_{max})$ versus $(1/T_{max})$ and calculate the activation energy for these traps.

The values from the resolution of equation 2 for deconvoluted peak 1 and 2 are summarized in table 3 -4 and figure 3. The first and second deconvoluted peaks showed a average peak temperature equal 117and 151°C with Ea equal 17 and 13kJ/mol, respectively. Based on the results obtained by Choo and Lee [11], and the fact that the interaction between hydrogen and dislocation start as much higher temperature, the first and second peak can be attributed as being grain boundaries and dislocations respectively. On the other hand, many authors [11,12] reported that the activation

energy from 20 to 58kJ/mol as being characteristics of grain boundaries and the range from 19 to 30 kJ/mol [11,13] could be attributed for dislocations. It is important to highlight that these authors studied different steels with different microstructure, and these values are just a prediction, and some differences are acceptable. The main point to be considered with the results found in this work is that the higher the desorption temperature, the harder it is for de-trap hydrogen.

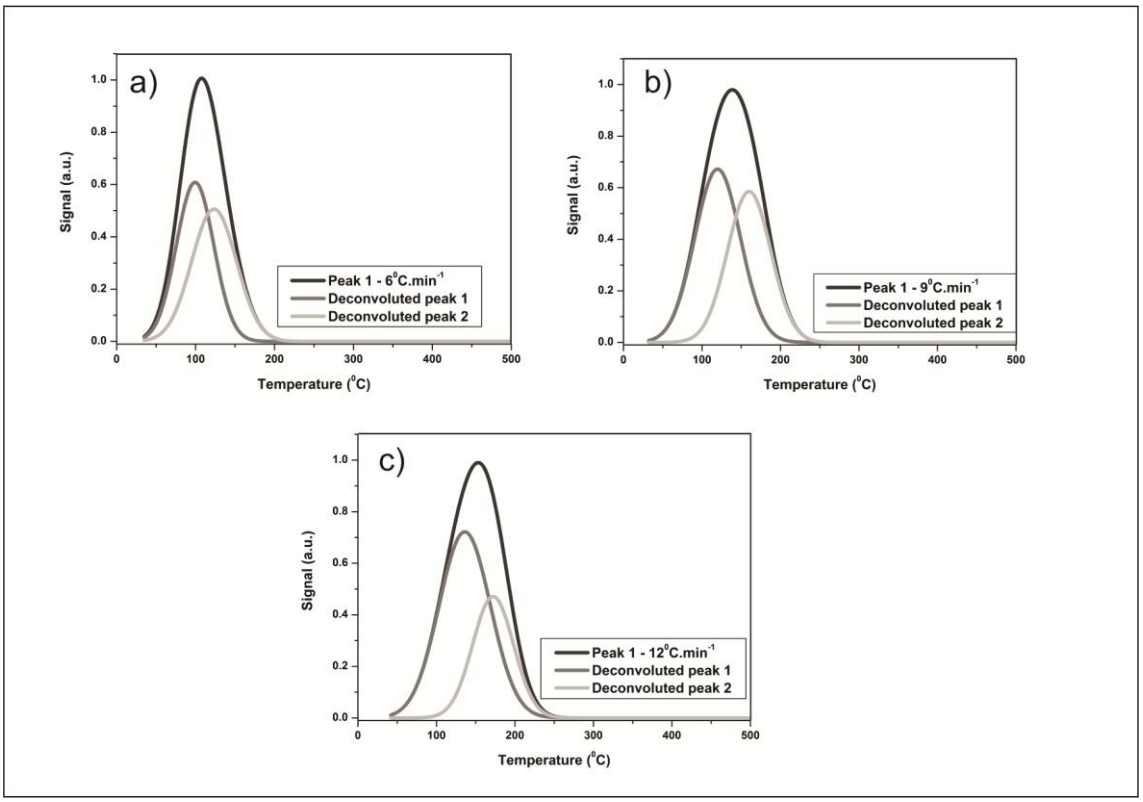


**Figure 2:** Deconvolution of TDS curve for as-quenched sample for heating rate **a)** 6°C.min$^{-1}$, **b)** 9°C.min$^{-1}$ **c)** 12°C.min$^{-1}$

**Table 3:** Data of the peak temperatures for each heating rate for the 1st deconvoluted peak for the as-quenched sample.

| **°C.min$^{-1}$** | **as-quenched sample - 1st peak** | | | **Ea (kJ.mol$^{-1}$)** |
|---|---|---|---|---|
| | **$\ln(\phi/T^2)$** | **$T_{max}$ (K)** | **$1/T_{max}$** | |
| 6 | -10.04 | 98 | 0.00269 | 17 |
| 9 | -9.74 | 117 | 0.00256 | |
| 12 | -9.54 | 136 | 0.00244 | |

**Table 4:** Data of the peak temperatures for each heating rate for the 2nd deconvoluted peak for the as-quenched sample.

| °C.min$^{-1}$ | as-quenched sample - 2nd peak | | | Ea (kJ.mol$^{-1}$) |
|---|---|---|---|---|
| | ln($\phi$/T$^2$) | $T_{max}$ (K) | 1/$T_{max}$ | |
| 6 | -10.1668 | 122 | 0.00253 | 13 |
| 9 | -9.94032 | 159 | 0.00231 | |
| 12 | -9.71192 | 172 | 0.00225 | |

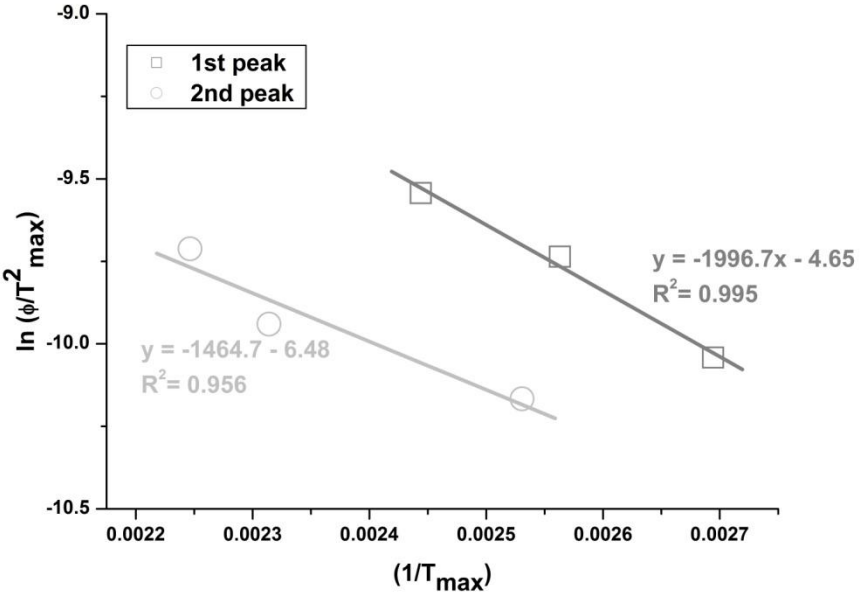


**Figure 3:** ln($\phi$/T$^2$) as a function of (1/$T_{max}$) for the two deconvoluted peaks of as-quenched.

***Chi sample***

Figure 4 and table 5 shows the TDS results of chi sample under investigation obtained by using the three heating rates described in experimental details.

As observed in as-quenched sample, the TDS spectra for chi sample, also presented a shift on the peak to higher temperature with increasing heating rate. This trend was obtained just for the peaks detected at low temperature. All heating rate presented 1 peak at low temperature and 2 different peaks at high temperature. The peak at low temperature represents the hydrogen de-trapped reversibly and the diffusible hydrogen. The 2nd peak was detected at 325, 376 and 411°C for 6, 9 and 12°C/min respectively. This high temperature shows an irreversible effect of this trap, and suggests that the

hydrogen was trapped by χ-phase and/or incoherent precipitates, as $Cr_{23}C_{6.}$ It is known that incoherent carbides present irreversible features and is de-trapped in high temperature [14,15].

The 3th peak was detected at higher temperature than the 2nd, showing more irreversible characteristics than 2nd peak. The temperature for this peak was close to the temperature detected for RA sample in the previous work [4], i.e. 492°C for RA (6°C.min$^{-1}$ heating rate) versus 468°C for chi (6°C heating rate). Both samples has retained austenite, and it was expected the same, or at least very close, de-trapped temperature.

Pavarthavatini [14] classified the traps in 3 categories, 1) very weak traps that are include dislocations, fine precipitates in the matrix and solutes like Cr and Mo; 2) intermediate traps that are include martensite laths and prior austenite grain boundaries; 3) strong traps that are include non-metallic inclusions, spherical precipitates, interfaces of martensite laths and/or prior austenite grain boundaries with retained austenite and fine precipitates or impurity segregations. Taking this classification into account is feasible to attribute the 2nd peak for χ-phase and/or $Cr_{23}C_6$ and 3th peak for $\gamma_{ret}$.

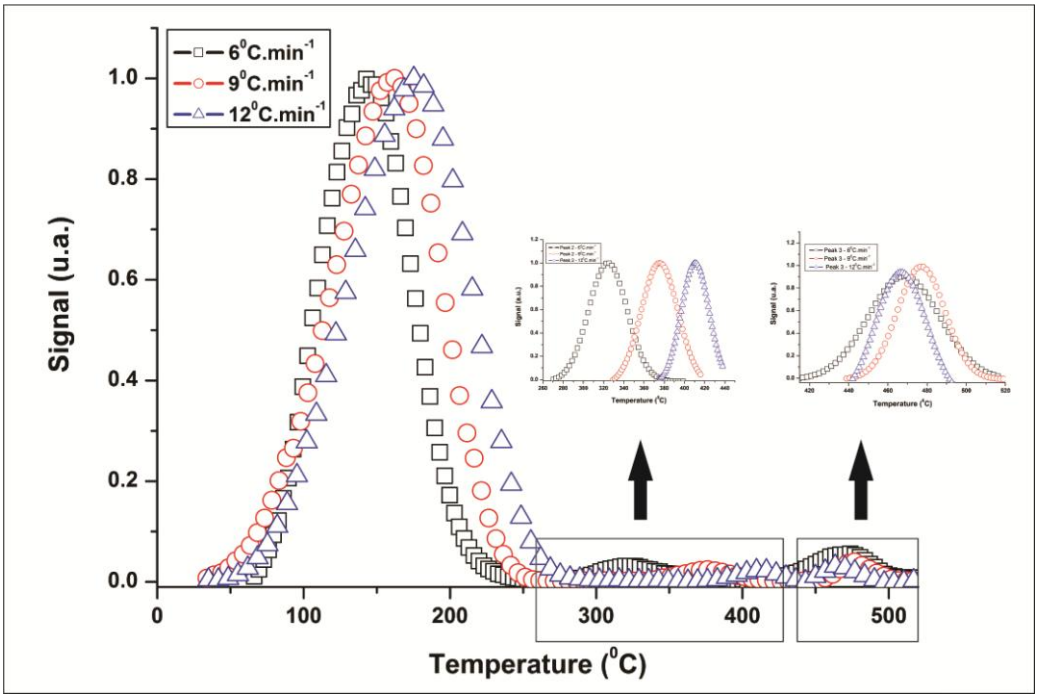


**Figure 4:** TDS results for the chi sample. Heating rate 6, 9 and 12°C.min$^{-1}$ with the zoom in the 2nd and 3th desorption peak temperature.

**Table 5:** Desorption temperature for peak 1, 2 and 3 of 6, 9 and 12°C.min$^{-1}$ heating rate.

| **Heating Rate (°C.min$^{-1}$)** | **Peak 1 (°C)** | **Peak 2 (°C)** | **Peak 3 (°C)** |
|---|---|---|---|
| 6 | 143 | 325 | 468 |
| 9 | 161 | 376 | 477 |
| 12 | 176 | 411 | 467 |

Figure 5 presents the results of the deconvolution procedure used in the chi sample using heating rate of 6, 9 and 12°C.min$^{-1}$. It was observed that the low temperature peak could be fitted nicely with two distinct peaks.

As made for as-quenched sample, the activation energy was calculated based on the deconvoluted peak 1 and 2 for all heating rate, these values are summarized in table 6-7 and figure 6. It can be seen that the values of activation energy for the two peaks were similar (20 and 17kJ/mol for peak 1 and 2, respectively) and based only in this value was not possible to differentiate the kind of trap that the hydrogen was de-trapped in this sample. Analyzing the difference among peak temperature in the 3 heating rate and 2 deconvoluted peaks, the 2nd deconvoluted peak was higher than 150°C for all heating rates, which can be attributed for the trapping on the dislocations. Comparing these results with as-quenched samples it can be said that the chi sample trapped hydrogen stronger than as-quenched sample, due the high temperature for the 1st and 2nd deconvoluted peak.

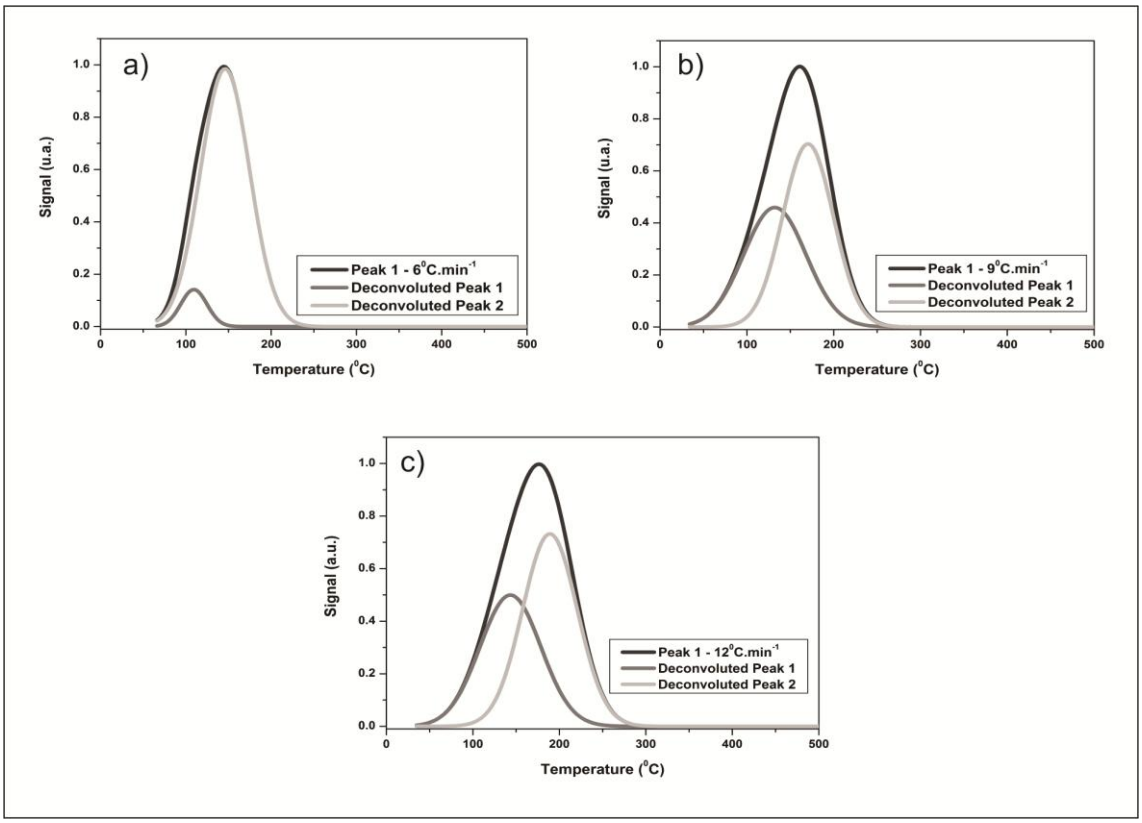


**Figure 5:** Deconvolution of TDS curve for chi sample for heating rate **a)** 6°C.min$^{-1}$, **b)** 9°C.min$^{-1}$ **c)** 12°C.min$^{-1}$

**Table 6:** Data of the peak temperatures for each heating rate for the 1st deconvoluted peak for the chi sample sample.

| °C.min$^{-1}$ | Chi sample - 1st peak | | | Ea (kJ.mol$^{-1}$) |
|---|---|---|---|---|
| | ln($\phi$/T$^2$) | $T_{max}$ (K) | 1/$T_{max}$ | |
| 6 | -10.11 | 110 | 0.00261 | 20 |
| 9 | -9.82 | 134 | 0.00246 | |
| 12 | -9.58 | 143 | 0.00240 | |

**Table 7:** Data of the peak temperatures for each heating rate for the 2nd deconvoluted peak for chi sample.

| °C.min$^{-1}$ | Chi sample - 2nd peak | | | Ea (kJ.mol$^{-1}$) |
|---|---|---|---|---|
| | ln($\phi$/T$^2$) | $T_{max}$ (K) | 1/$T_{max}$ | |
| 6 | -10.28 | 144 | 0.00240 | 17 |
| 9 | -10.00 | 171 | 0.00225 | |
| 12 | -9.79 | 189 | 0.00216 | |

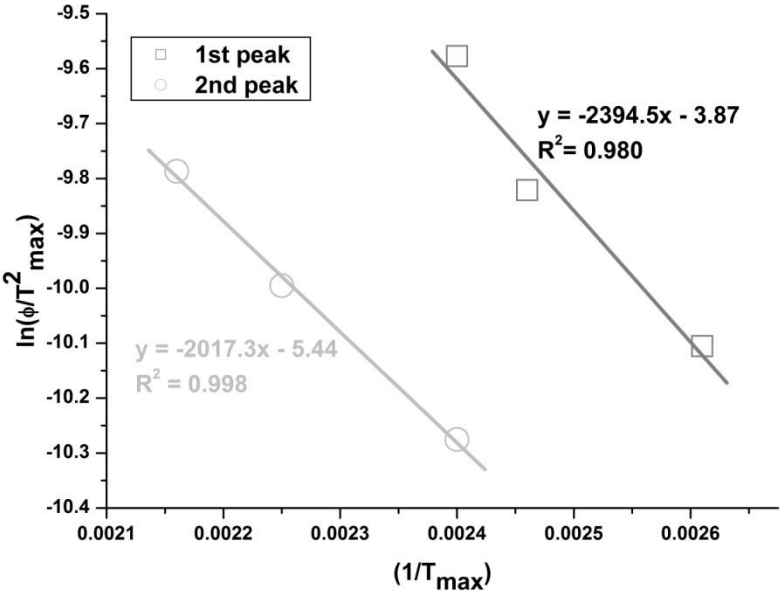


**Figure 6:** $\ln(\phi/T^2)$ as a function of $(1/T_{max})$ for the two deconvoluted peaks of chi sample.

***Low Retained Austenite sample***

Figure 7 and table 8 shows the TDS results of LRA sample under investigation obtained by using the 3 heating rate described in experimental details. The same trend of the as-quenched and the chi sample was observed in the LRA sample, i.e. also presented a shift on the peak to higher temperature with increasing heating rate.

All heating rate presented 1 peak at low temperature and 1 peak at high temperature. The peak at low temperature show the presence of hydrogen trapped irreversibly and diffusible hydrogen. The peak at high temperature (peak 2) shows the presence of irreversible trap in this microstructure that can be attributed also for $\gamma_{ret}$, since this sample presented just this phase in the microstructure that can de-trap hydrogen at high temperature.

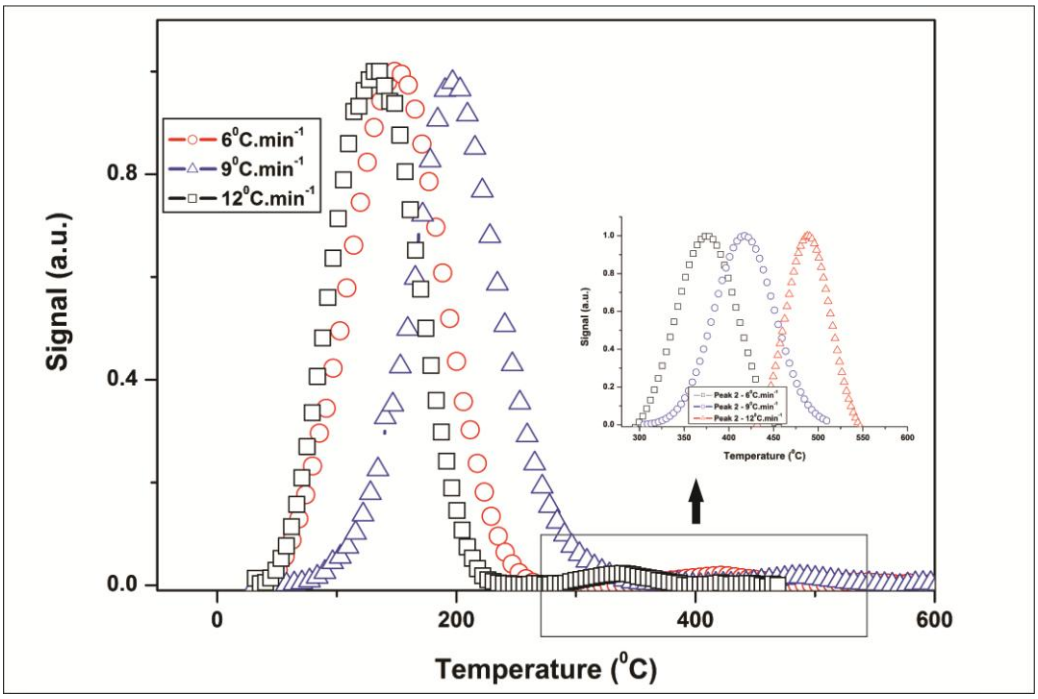


**Figure 7:** TDS results for the LRA sample. Heating rate 6, 9 and 12°C.min$^{-1}$ with the zoom in the 2nd desorption peak temperature.

**Table 8:** Desorption temperature for peak 1 and 2 of 6, 9 and 12°C.min$^{-1}$ heating rate.

| Heating Rate (°C.min$^{-1}$) | Peak 1 (°C) | Peak 2 (°C) |
|---|---|---|
| 6 | 133 | 337 |
| 9 | 148 | 416 |
| 12 | 197 | 490 |

Figure 8 presents the results of the deconvolution procedure used in the LRA sample using heating rate of 6, 9 and 12°C.min$^{-1}$.

It was observed that the low peak temperature showed two deconvoluted peaks which the fit for it could be fitted, but with low $R^2$ (figure 9). As made for as-quenched and chi sample, the activation energy was calculated based on the deconvoluted peak 1 and 2 for all heating rate, these values are summarized in table 9-10 and figure 9.

It can be seen that the values of activation energy for the two peaks were very low for the first and second peaks (4 and 11kJ.mol$^{-1}$ respectively).

Analyzing the difference among peak temperature in the 3 heating rate and 2 deconvoluted peaks, the 2nd deconvoluted peak was higher than the first for all heating rates, and the low trapping binding energy calculated for this peak predict that the hydrogen was trapped mainly for the interstice of the ferrite and martensite. Michler and Balogh [16] reported that low binding energies are reported for common structural features like grain boundaries, dislocations or substitutional elements, as being the

intersticial site in iron based alloy presenting Ea around 4-8kJ.mol$^{-1}$, this can explain that the mainly irreversible hydrogen trapped in the LRA sample was from the lattice parameter. Since this sample has tempered martensite, ferrite plus a small amount of retained austenite, these results are in agreement with the low binding energy found here.

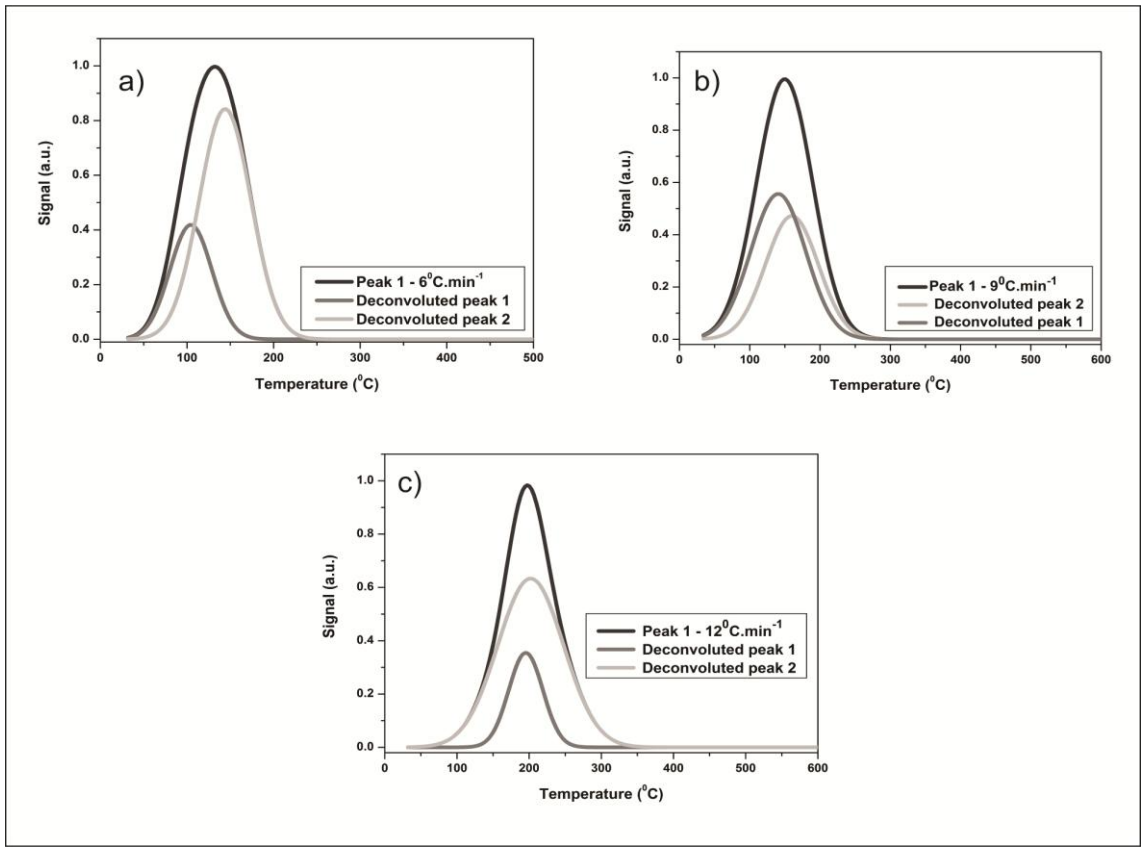


**Figure 8:** Deconvolution of TDS curve for LRA sample for heating rate **a)** 6°C.min$^{-1}$, **b)** 9°C.min$^{-1}$ **c)** 12°C.min$^{-1}$

**Table 9:** Data of the peak temperatures for each heating rate for the 1st deconvoluted peak for the LRA sample.

| °C.min$^{-1}$ | LRA sample - 1st peak | | | Ea (kJ.mol$^{-1}$) |
|---|---|---|---|---|
| | ln($\phi$/T$^2$) | $T_{max}$ (K) | 1/$T_{max}$ | |
| 6 | -10.0682 | 103 | 0.00266 | 4 |
| 9 | -9.8504 | 140 | 0.00242 | |
| 12 | -9.80839 | 194 | 0.00214 | |

**Table 10:** Data of the peak temperatures for each heating rate for the 2nd deconvoluted peak for the LRA sample.

| °C.min$^{-1}$ | LRA sample - 2nd peak | | | Ea (kJ.mol$^{-1}$) |
|---|---|---|---|---|
| | ln($\phi$/T$^2$) | $T_{max}$ (K) | 1/$T_{max}$ | |
| 6 | -10.2799 | 145 | 0.00239 | 11 |

| | | | |
|---|---|---|---|
| 9 | -9.94494 | 160 | 0.00231 |
| 12 | -9.84656 | 203 | 0.00210 |

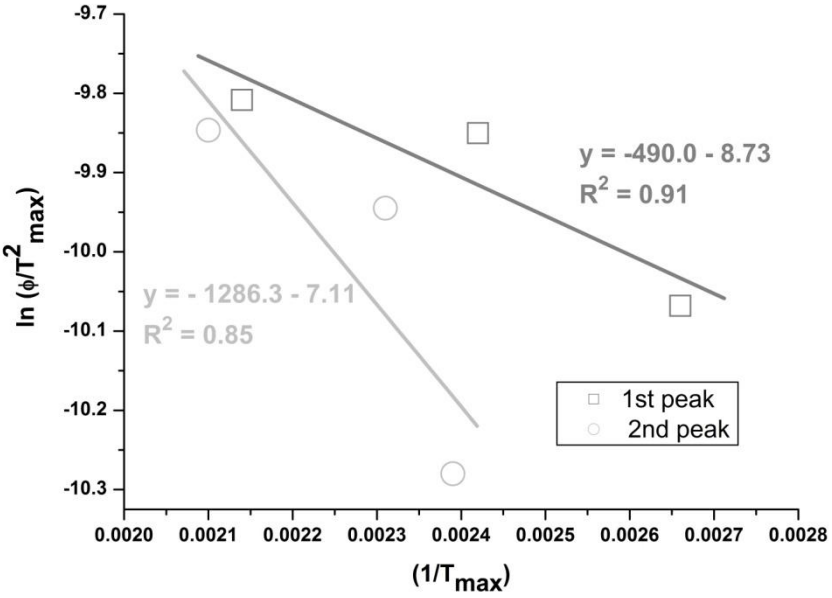


**Figure 9:** $\ln(\phi/T^2)$ as a function of $(1/T_{max})$ for the two deconvoluted peaks of LRA sample.

***Retained Austenite sample***

Figure 10 and table 11 show the TDS results of LRA sample under investigation obtained by using the 3 heating rate described in experimental details. As observed in the as-quenched, chi and LRA samples, the TDS spectra for RA, also presented an increase in peak temperature with increasing heating rate for the peaks detected at low temperature. All heating rate presented 1 peak at low temperature and 1 different peak at high temperature. The first peak can be attributed for reversible in diffusible hydrogen and the second for retained austenite. The explanation for these peaks is the same used for the samples analyzed above (Chi and LRA samples).

**Table 11:** Desorption temperature for peak 1 and 2 of 6, 9 and 12°C.min$^{-1}$ heating rate.

| **Heating Rate (°C.min$^{-1}$)** | **Peak 1 (°C)** | **Peak 2 (°C)** |
|---|---|---|
| 6 | 194 | 492 |
| 9 | 204 | 415 |
| 12 | 210 | 465 |

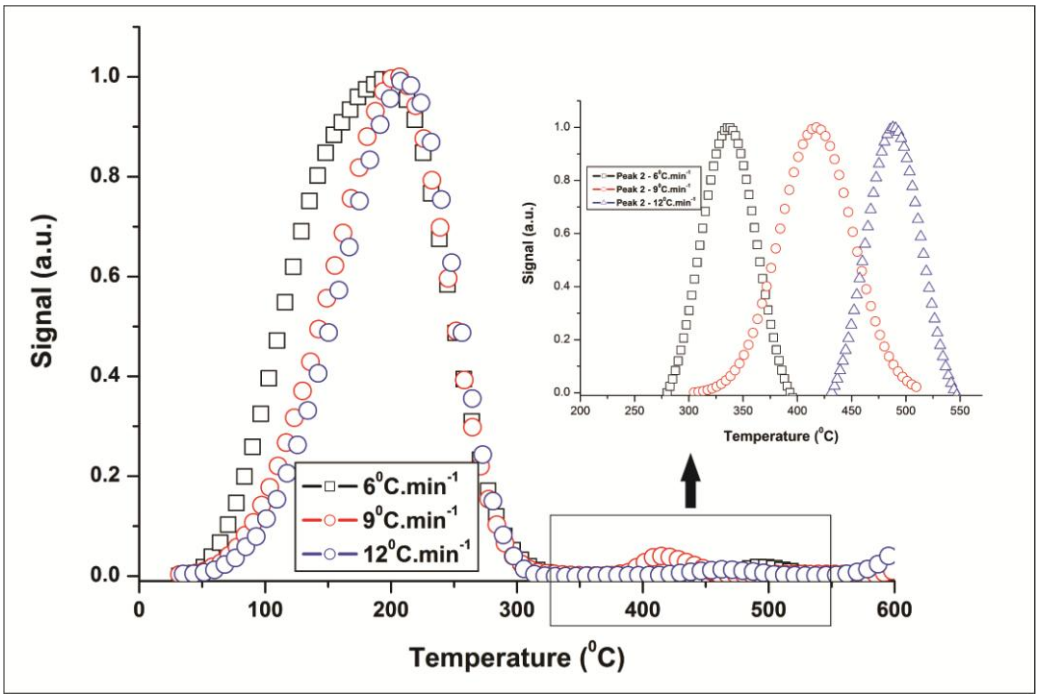


**Figure 10:** TDS results for the RA sample. Heating rate 6, 9 and 12°C.min$^{-1}$ with the zoom in the 2nd desorption peak temperature.

Figure 11 presents the results of the deconvolution procedure used in the RA sample using heating rate of 6, 9 and 12°C.min$^{-1}$. It was observed that the low temperature peak showed two deconvoluted peaks which the fit for it could be fitted nicely.

As made for all the samples above, the activation energy was calculated based on the deconvoluted peak 1 and 2 for all heating rate, these values are summarized in table 12-13 and figure12a and 12b. The $E_a$ for the 1st deconvoluted peak was low enough to predict that hydrogen was trapped by dislocations. Despite the curve fitted the values quite good (figure 12b), the $E_a$ for the 2nd deconvoluted peak was not possible to calculate, the result was very high, and further investigation have to be made.

Comparing these results with the as-quenched, chi and LRA samples it can be said that the RA sample trapped hydrogen stronger than both, due the high temperature for the 1st and 2nd deconvoluted peak. It was already expected since this sample was double quenched for 1h, decreasing the amount of defects in the microstructure and increasing the solubility of hydrogen and hence the capacity to trap hydrogen.

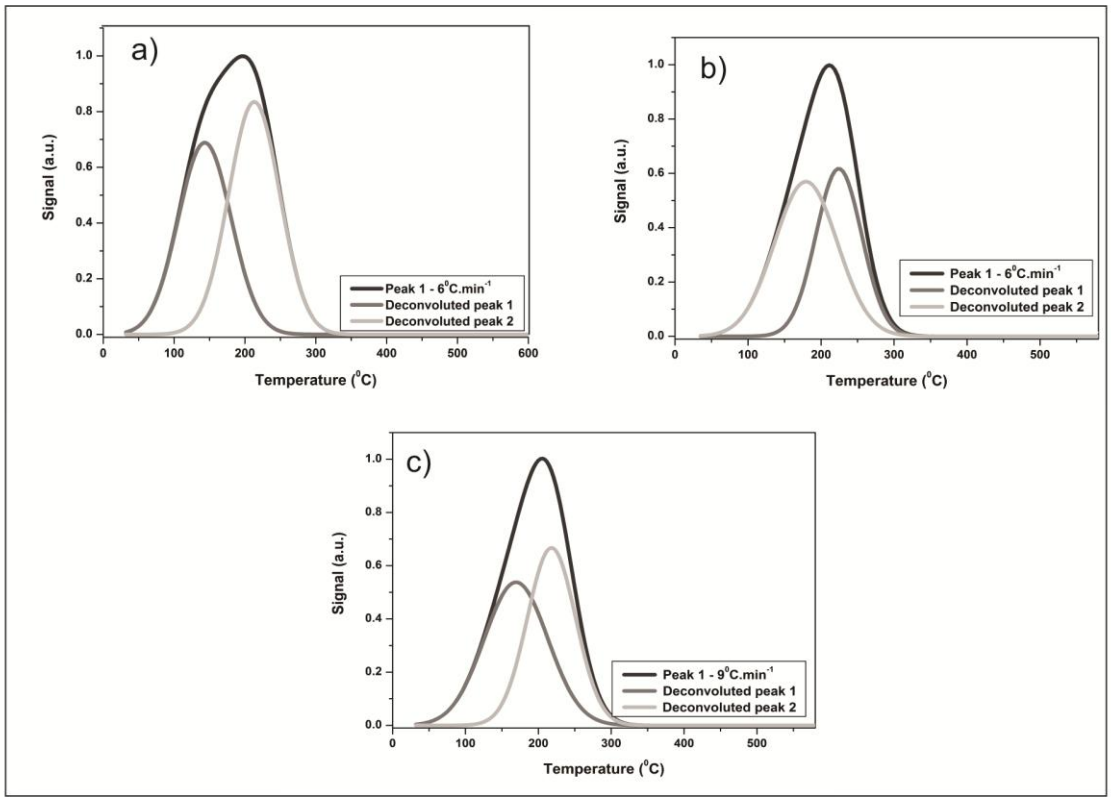


**Figure 11:** Deconvolution of TDS curve for RA sample for heating rate **a)** 6°C.min$^{-1}$, **b)** 9°C.min$^{-1}$ **c)** 12°C.min$^{-1}$

**Table 12:** Data of the peak temperatures for each heating rate for the 1st deconvoluted peak for the RA sample.

| **°C.min$^{-1}$** | **RA sample - 1st peak** | | | **Ea (kJ.mol$^{-1}$)** |
|---|---|---|---|---|
| | **ln($\phi$/T$^2$)** | **$T_{max}$ (K)** | **1/$T_{max}$** | |
| 6 | -14.3647 | 143 | 0.00240 | 22 |
| 9 | -14.0849 | 170 | 0.00226 | |
| 12 | -13.8419 | 180 | 0.00221 | |

**Table 13:** Data of the peak temperatures for each heating rate for the 2nd deconvoluted peak for the RA sample.

| **°C.min$^{-1}$** | **RA sample - 2nd peak** | | | **Ea (kJ.mol$^{-1}$)** |
|---|---|---|---|---|
| | **ln($\phi$/T$^2$)** | **$T_{max}$ (K)** | **1/$T_{max}$** | |
| 6 | -10.5772 | 212 | 0.00206 | - |
| 9 | -10.1963 | 218 | 0.00204 | |
| 12 | -9.92885 | 223 | 0.00202 | |

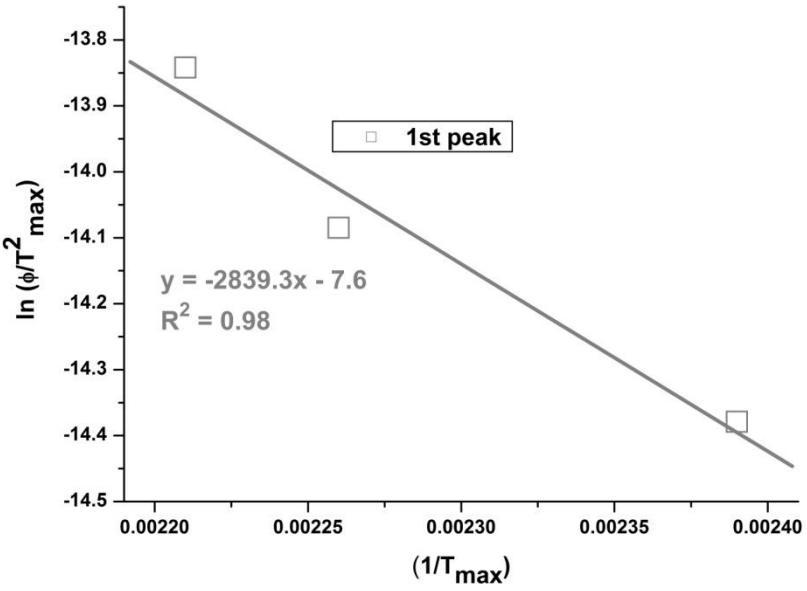


**(a)**

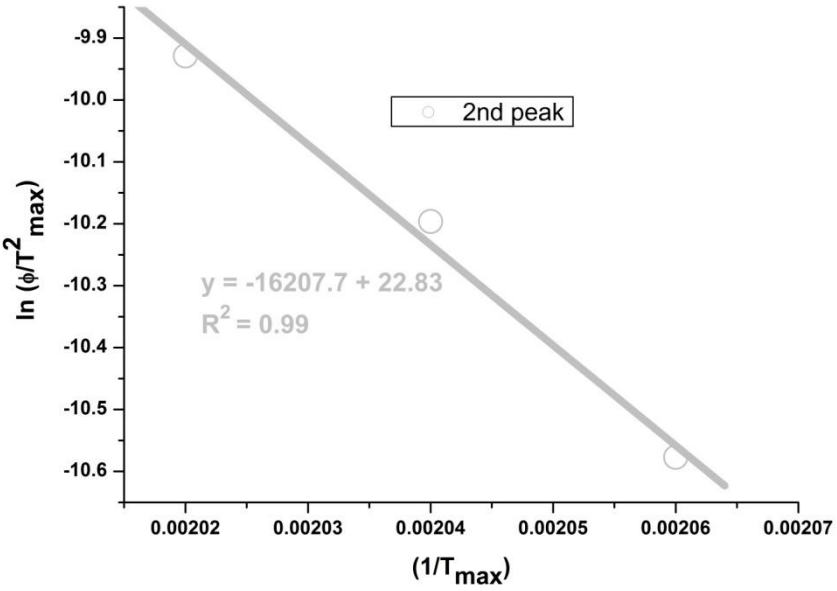


**(b)**

**Figure 12:** $\ln(\phi/T^2)$ as a function of $(1/T_{max})$ for the two deconvoluted peaks of RA sample. **a)** 1st deconvoluted peak; **b)** 2nd deconvoluted peak.

***High Retained Austenite sample***

Figure 13 and table 14 show the TDS results of HRA sample under investigation obtained by using the 3 heating rate described in experimental details. As observed in all the samples above (as-quenched, Chi, LRA and RA), the TDS spectra for the HRA sample, also presented an increase in peak temperature with increasing heating rate for the peaks detected at low temperature. All heating rate presented 1 peak at low temperature and 1 peak at high temperature. The peak at low temperature represents the hydrogen de-trapped at reversible and diffusible hydrogen.

The peak detected at high temperature for the HRA sample was lower than the peak presented for the LRA and RA samples (396°C for HRA, 457°C for RA and 414°C for LRA, ***average of the 3 values in each heating rate***).

The temperature range in the second peak is close to the range found in the second peak for chi-sample (396°C versus 371°C, respectively). The HRA sample presented a phase rich in Cr and Mo at the grain boundaries, some precipitates in the ferrite and traces of $Cr_{23}C_6$, and this peak can be de-trapped from this phase, and not from the retained austenite. Park et. al. [17] studied the influence of retained austenite as a hydrogen trap in steel welds, and found that the de-trapped temperature of hydrogen from retained austenite was higher than 500°C for samples with different amount of austenite or/retained austenite. The sample with less amount of retained austenite (4%) presented a shift to low peak (590°C) temperature, and the sample with 12% of retained austenite and 50% of austenite showed a little higher peak temperature (600°C). They showed that the amount of retained austenite can influence in the de-trap temperature. Maroef et. al. [18] studied the presence of hydrogen in retained austenite in the ferritic welds, and found that hydrogen remains trapped in this phase up to temperatures above 500°C. Michler and Balogh [16] studied a TRIP steel with different amount of retained austenite also found a peak desorption in 500°C.

It seems that the retained austenite in the HRA sample will de-trap this phase at high temperature, due the high amount of retained austenite. The trend found by Park et. al. [17] can be extrapolated for the results in the HRA sample, since this sample has 22% of retained austenite, and probably the hydrogen de-trapped of it will be done at high temperature.

Is it important to highlight that in the heating rate of 12°C.min$^{-1}$ at the 2nd peak there is a 3th peak that mix with the end of the 2nd peak, and this "3th" peak was detected at high temperature, close to 500°C. It seems that in this test condition there was a trend to

detect hydrogen de-trapped from retained austenite. Further investigations have to be done, to confirm these results.

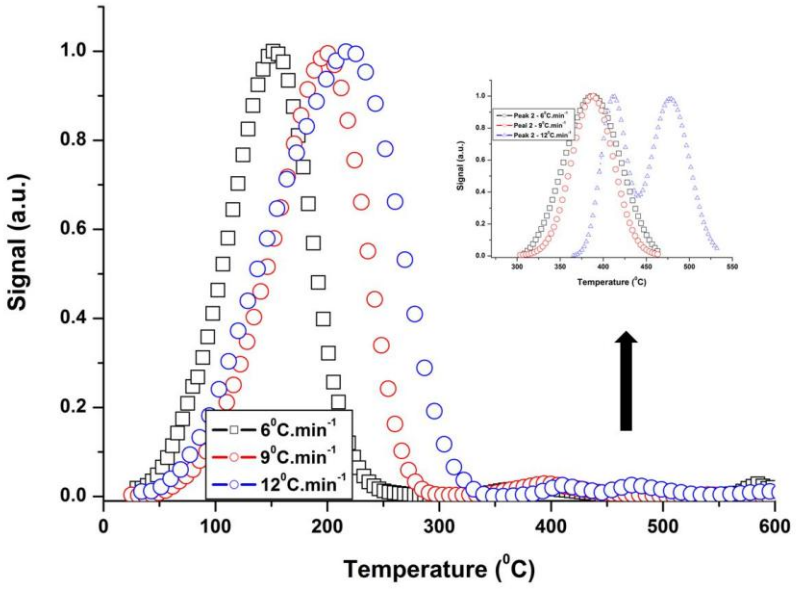


**Figure 13:** TDS results for the HRA sample. Heating rate 6, 9 and 12°C.min$^{-1}$ with the zoom in the 2nd desorption peak temperature.

**Table 14:** Desorption temperature for peak 1 and 2 of 6, 9 and 12°C.min$^{-1}$ heating rate.

| Heating Rate (°C.min$^{-1}$) | Peak 1 (°C) | Peak 2 (°C) |
|---|---|---|
| 6 | 151 | 382 |
| 9 | 199 | 396 |
| 12 | 219 | 411 |

Figure 14 presents the results of the deconvolution procedure used in the HRA sample using heating rate of 6, 9 and 12°C.min$^{-1}$. It was observed that the low temperature peak showed two deconvoluted peaks which the fit for it could be fitted nicely.

As made for all the samples above, the activation energy was calculated based on the deconvoluted peak 1 and 2 for all heating rate, these values are summarized in table 15-16 and figure15. It can be seen that the values of activation energy for the two peaks were very low for the first and second peaks (21 and 10kJ.mol$^{-1}$ respectively).

Analyzing the difference among peak temperature in the 3 heating rate and 2 deconvoluted peaks, the 2nd deconvoluted peak was higher than the first for all heating rates, which can be attributed for the trapping on the dislocations. Comparing these results with the samples above it can be said that the HRA sample trapped hydrogen stronger than both, due the high temperature for the 1st and 2nd deconvoluted peak. It was already expected since this sample was double quenched for 1h, decreasing the

amount of defects in the microstructure and increasing the capacity of trap hydrogen, and also increasing the amount of retained austenite in the microstructure.

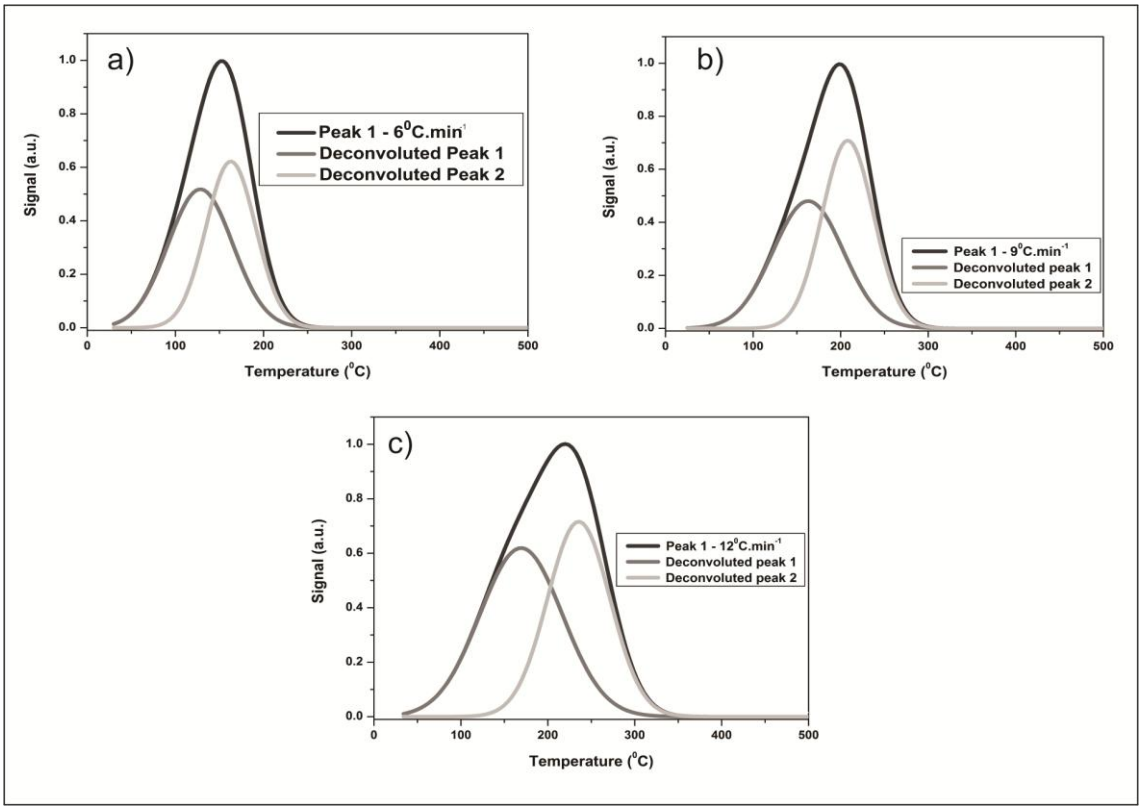


**Figure 14:** Deconvolution of TDS curve for HRA sample for heating rate **a)** 6°C.min$^{-1}$, **b)** 9°C.min$^{-1}$ **c)** 12°C.min$^{-1}$

**Table 15:** Data of the peak temperatures for each heating rate for the 1st deconvoluted peak for the HRA sample.

| °C.min$^{-1}$ | HRA sample - 1st peak | | | Ea (kJ.mol$^{-1}$) |
|---|---|---|---|---|
| | ln($\phi$/T$^2$) | $T_{max}$ (K) | 1/$T_{max}$ | |
| 6 | -10.2315 | 135 | 0.00245 | 21 |
| 9 | -9.94956 | 161 | 0.00230 | |
| 12 | -9.70291 | 170 | 0.00226 | |

**Table 16:** Data of the peak temperatures for each heating rate for the 2nd deconvoluted peak for the HRA sample..

| °C.min$^{-1}$ | HRA sample - 2nd peak | | | Ea (kJ.mol$^{-1}$) |
|---|---|---|---|---|
| | ln($\phi$/T$^2$) | Tmax (K) | 1/$T_{max}$ | |
| 6 | -10.3642 | 163 | 0.00229 | 10 |
| 9 | -10.1551 | 208 | 0.00208 | |
| 12 | -9.98058 | 236 | 0.00196 | |

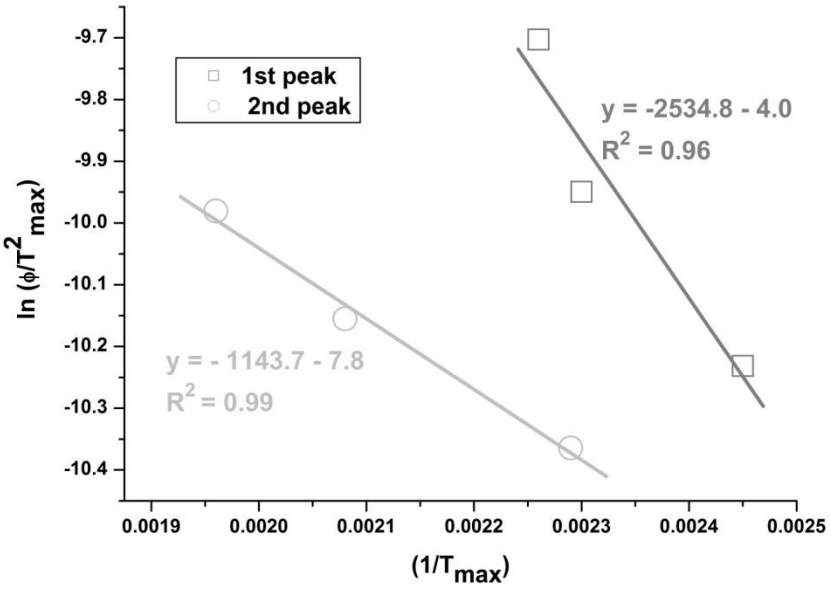


**Figure 15**: $\ln(\phi/T^2)$ as a function of $(1/T_{max})$ for the two deconvoluted peaks of HRA sample.

## Discussion

The figure 16 shows the desorption temperature at first peak for all the samples tested at 6°C.min$^{-1}$ versus the amount of retained austenite. The results are shown the tendency to increase the desorption temperature with the increase of the austenite content. As discussed above, this peak temperature is responsible for trap hydrogen reversibly indicating the presence of diffusible hydrogen, and the higher the desorption temperature the stronger the hydrogen is trapped in the microstructure.

The LRA sample showed a little higher temperature desorption for hydrogen than as-quenched sample, indicating that the LRA sample trapped hydrogen a little stronger than the as-quenched sample. Since the LRA sample was quenched at 600°C for 1h this fact was already expected, as this heat treatment promoted a decrease in the defects on the microstructure, promoting a small amount of retained austenite and generating more preferential local to trap hydrogen stronger.

Despite the chi sample has the same amount of retained austenite that RA sample, the peak temperature for chi sample was lower than for RA sample. It is important to highlight that the presence of $\chi$-phase in the chi sample could influenced in this desorption temperature, since this phase showed a desorption temperature peak in a

temperature lower than the retained austenite in the RA sample. Another point is that the solubility of hydrogen in RA sample was much higher than in chi sample (1577mol.Hm$^{-3}$ versus 904 mol.Hm$^{-3}$) [4], and this high solubility is responsible for a high desorption peak temperature for RA sample.

The desorption peak temperature for RA versus HRA samples was almost the same (143 versus 135°C) it seems that the morphology of retained austenite discussed in the previous work [10] may be contributing to this result. In this case, further investigations have to be done.

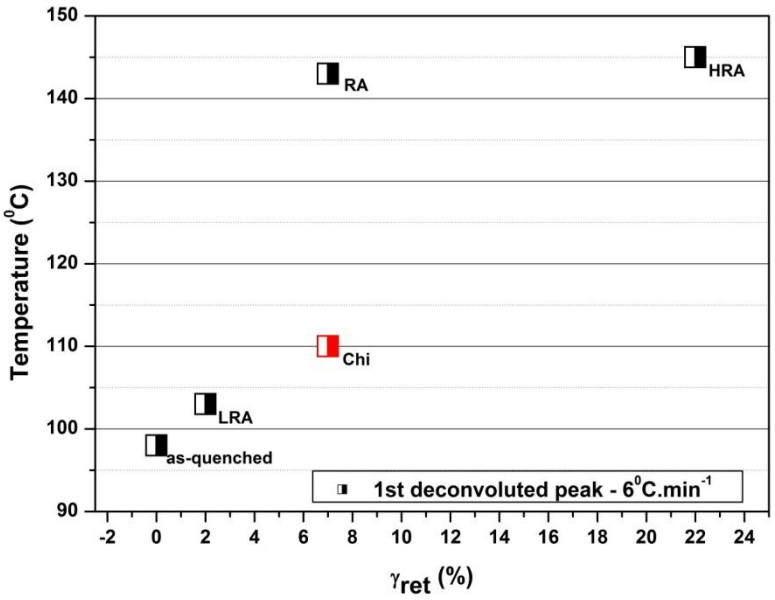


**Figure 16:** Desorption temperature peak of the 1st deconvoluted peak versus % retained austenite.

## Conclusions

All the samples showed the presence of diffusible hydrogen and the capacity to trap hydrogen reversibly. The first peak for all the samples was deconvoluted and was nicely fitted. The samples with χ-phase and $\gamma_{ret}$ showed a desorption peak at high temperature, showing that these phase trap hydrogen irreversibly. Further investigations have to be made in order to improve the accuracy of the desorption peak at high temperatue.

## References

[1]Li D., Gangloff R. P., Scully J. R. Hydrogen Trap States in Ultrahigh-Strength AERMET 100 Steel. Metallurgical and Materials Transactions A 2004, 35A: 849-64

[2] Pérez Escobar D., Verbeken K., Duprez L., Verhaege M. Evaluation of hydrogen trapping in high strength steels by thermal desorption. Materials Science and Engineering A 2012, 551:50– 58.

[3] Pérez Escobar D., Depover T., Duprez L., Verbeken K., Verhaege M. Combined thermal desorption spectroscopy, differential scanning calorimetry, scanning electron microscopy and X-ray diffraction study of hydrogen trapping in cold deformed TRIP steel. Acta Materialia 2012, 60: 2012 2593–05.

[4] Garcia D.C.S., Carvalho R.N., Lins V.F.C., Rezende D.M., Dos Santos D.S. Influence of microstructure in the hydrogen permeation in martensitic-ferritic stainless steel, International Journal of Hydrogen Energy 2015, http://dx.doi.org/10.1016/j.ijhydene.2015.06.102

[5] Lee S., Lee J. The trapping and transport phenomena of hydrogen in nickel. Metallurgical Transactions A 1986, 17: 181-87.

[6] Turnbull A, Hutchings R. B., Ferriss D. H. Modelling of thermal desorption of hydrogen from metals. Materials Science Engineerging 1997, 238: 317-28.

[7] Szost BA, Vegter RH, Rivera-Dı´az-del-Castillo PEJ. Hydrogen trapping mechanisms in nanostructured steel. Metallurgical .Mater Trans 2013; 44A: 4542-50.

[8] Frappart S., Oudriss A., Feaugas X., Creus J., Bouhattate J., Thebault F., Delattre L., Marchebois H. Hydrogen trapping in martensitic steel investigated using electrochemical permeation and thermal desorption spectroscopy. Scripta Materialia 2011, 65: 859–62.

[9] Silverstein R., Eliezer D. Hydrogen trapping mechanism of different duplex stainless steels alloys. Journal of Alloys and Compounds 2015, 644: 280‑86.

[10] Garcia D.C.S., Carvalho R.N., Lins V.F.C., Dos Santos D.S. Influence of retained austenite in the hydrogen diffusion in martensitic-ferritic stainless steel, submitted to International Journal of Hydrogen Energy 2015/October.

[11] CHOO W.Y., LEE J. Y. Thermal Analysis of Trapped Hydrogen in Pure Iron. Metallurgical Transactions A 1982, 13A: 135-40.

[12] Pressouyre G.M., A Classification of Hydrogen Traps in Steel. Metallurgical Transactions A 1979, 10: 1571–73.

[13] Takai K., Chiba Y., Noguchi K., Nozue A., Metallurgical. Materials. Transaction A 2002, 33: 2659-65.

[14] Parvarthavarthini N, Saroja S. Studies on hydrogen permeability of 2.25% Cr-1% Mo ferritic steel: correlation with microstructure. Journal of Nuclear Materials 2001;288: 187-96.

[15] Wei F.G., Tsuzaki K. Metallurgical and Materials Transactions. A, 2006, 37A: 331–53.

[16] Michler T., Balogh M. P. Hydrogen environment embrittlement of an ODS RAF steel - Role of irreversible hydrogen trap sites. International Journal of Hydrogen Energy 2010, 35: 975-54.

[17] Park B.Y.D., Maroef I.S., Landau A., Olson D.L. Retained Austenite as a Hydrogen Trap in Steel Welds Hydrogen trapping is investigated as a means of improving resistance to hydrogen-assisted cracking in HSLA steels. WELDING JOURNAL 27S-35S.

[18] Maroef I. Hydrogen trapping in ferritic steel weld metal. Int. Mater Ver. 2002, 47(4):191-223.

# *CHAPTER 5 – Conclusions*

## Conclusions

In this work the as-quenched sample was heat treated at different temperatures and the retained austenite and chi-phase were evaluated in terms of hydrogen permeation and hydrogen embrittlement.

The amount of $\gamma_{ret}$ increased in the microstructure as the tempering temperature increased, showing the high amount (22%) of this phase in the matrix for the heat treatment performed at 675°C for 1h.

The heat treatment at 670°C for 18h to obtain χ-phase was successful, and the chi sample presented a phase rich in Cr and Mo at the grain boundaries and inside the ferrite.

The morphology of retained austenite in the matrix plays a role of the diffusion and solubility of the hydrogen. In which, the sample with 22% of retained austenite (plate form) showed the lowest hydrogen diffusion coefficient and the sample with 7% of this phase (needles form) showed the highest hydrogen solubility.

The SSRT test condition showed higher hydrogen embrittlement for the chi, RA and HRA samples, than the 168h test condition.

The ductility of tensile test samples was greatly reduced by the presence of retained austenite and chi-phase when the microstructure was charged with hydrogen prior to testing, showing a significant hydrogen embrittlement in all the samples.

The $\gamma_{ret}$ showed higher deleterious effect by hydrogen than χ-phase, since the sample with 7% of retained austenite (RA) presented higher LD than the sample with 7% of retained austenite and 6% of χ-phase. (LD = 86 versus 80%, respectively). Further investigations have to be made, in order to evaluate the TRIP effect in the samples tested.

All the samples presented diffusible hydrogen with a desorption peak at low temperature, and the presence of χ-phase and $\gamma_{ret}$ in the matrix shift the desorption peak for high temperature. In addition, all the samples presented a desorption peak at high temperature, showing the capacity of χ-phase and $\gamma_{ret}$ to trap hydrogen irreversibly.

## Suggestions for future studies

- To perform electrochemical hydrogen permeation test in different temperature;
- To perform gaseous hydrogen permeation;
- Multi scale simulation;
- Evaluate statistically the results of hydrogen permeation.